QUANTIFYING MICROBUBBLE STREAMING AND ITS APPLICATIONS

BY

VENKATARAMA BHARGAV RALLABANDI

DISSERTATION

Submitted in partial fulfillment of the requirements
for the degree of Doctor of Philosophy in Theoretical and Applied Mechanics
in the Graduate College of the
University of Illinois at Urbana-Champaign, 2015

Urbana, Illinois

Doctoral Committee:

Associate Professor Sascha Hilgenfeldt, Chair and Director of Research
Professor Jonathan Freund
Assistant Professor Randy Ewoldt
Associate Professor Daniel Bodony

Abstract

The growing interest in microfluidics in the last two decades has resulted in new and exciting ways in which to drive microfluidic flows. A simple and powerful flow actuation method involves the use of acoustically excited microbubbles. For ease of manufacture and flow control, setups have largely focused on microbubbles of semi-cylindrical shape, attached to a wall of the microchannel. The application of an ultrasound field drives oscillations of the bubble interface, which then become rectified into strong secondary steady currents in the fluid, termed "streaming". While several researchers have used such setups in experiments, a theoretical quantification of the bubble streaming flows, crucial for the systematic design of practical microfluidics applications, has lagged behind.

In the first part of the dissertation, we resolve both the primary oscillatory and secondary steady flow components. We begin by developing an asymptotic theory describing the oscillatory response of the bubble to the applied acoustic field. We show that the presence of viscous boundary layers and pinned contact lines at the walls (i) strongly couples volume oscillations of the bubble to shape oscillations of the interface, and (ii) results in much wider surface-mode frequency resonance peaks than is nominally predicted by potential flow theory. The oscillatory dynamics then feed into a calculation of the secondary flow, which rigorously accounts for boundary layers over the bubble and the wall. We show that the two-dimensional steady vortical streaming flows observed in experiment are governed at low frequencies by surface mode dynamics, but undergo a reversal of orientation at higher frequencies, where volume oscillations dominate. The theory therefore connects the oscillatory dynamics to the steady streaming, reproducing the entire spectrum of steady flow patterns observed in experiments, with no adjustable parameters.

The 2D theory is then modified to include 3D flow effects, in the light of recent collaborative experimental measurements. We show that these flows arise due to the axial confinement of the bubble by no-slip walls, and can be modeled by a perturbation of the 2D streaming solutions

by additional (axial) Stokes solutions. The 3D theory explains the experimentally observed flow kinematics over a wide range of time scales, showing that the 2D trajectories typically observed in experiments are in fact sections of a higher three-dimensional flow structure that becomes apparent only on much longer time scales. We then develop a Hamiltonian formalism that governs the long time 3D motion and is applicable to any perturbed 2D flow under confinement.

Having now systematically developed a theoretical description of the flow field, the second part of the dissertation deals with its application to practically useful situations in microfluidics. We first analyze the micromixing between two fluid streams continuously transported through the channel by a Poiseuille flow, whose mixing properties are enhanced by an array of acoustically excited bubbles located at the channel walls. We argue that in order to achieve exponentially fast fluid mixing, it is necessary to introduce a temporal modulation in the flow field, achieved here through a duty cycling of the streaming flow (i.e., of the driving ultrasound). It is then shown using numerical simulations that the mixing is optimized at specific duty cycles that can be understood from global transport properties of the Poiseuille flow and the streaming vortices, thus forming the first protocol for open-flow mixing that is optimized from first principles.

Finally, we analyze the motion of rigid spherical microparticles within streaming flows, with the intention of designing a size-sensitive sorting device. We show that assuming a short-range hard-core interaction to prevent penetration of particle and bubble surfaces is sufficient to explain a drift of particles across streamlines close to the bubble. This drift ultimately results in the size-dependent sorting behavior observed in experiments, provided that 3D flow effects are properly accounted for.

To my grandfather, a man I deeply admire.

Acknowledgements

First and foremost, I would like to express my deepest gratitude to my advisor Professor Sascha Hilgenfeldt, for his extraordinary mentorship, encouragement and support through my doctoral study, without which this dissertation would not be possible. The wealth of experience that I have gained through interactions with him has been crucial in honing my scientific temperament and has helped me become a more mature researcher. He has afforded me a great deal of intellectual and personal freedom during my time here, for which I thank him deeply.

I also thank Professor Christian Kähler, whose willingness and enthusiasm to host me at the Bundeswehr University in Munich has resulted not only in fruitful collaborative research, but also in a number of new friendships and experiences. I would also like to thank my doctoral committee members – Professor Jonathan Freund, Professor Randy Ewoldt and Professor Daniel Bodony – for their valuable comments and insightful discussions about my work.

This work would scarcely have been possible without the rigorous foundation in applied mechanics and mathematics that I was provided with through graduate classes at MechSE, which have carried me through my doctoral work and will stay with me long beyond. I would like to especially thank Professor Matthew West for those wonderful mathematics lectures, and Professor Moshe Matalon for his excellent course on asymptotic methods, which have played a crucial role during my early years as a graduate student.

I wish to thank all the people I have had the pleasure of collaborating with, many of whom have become close friends. I thank the current and past members of our research group here at MechSE – Shreyas Jalikop, Cheng Wang, Lin Guo, Raqeeb Thameem, Rui Yang, and Sangwoo Kim – for fruitful discussions over the years. I also thank my collaborators in Munich – Alvaro Marin, Massimiliano Rossi, Rune Barnkob and Andreas Volk – for making my stay in Munich a memorable and intellectually stimulating one.

The administrative staff of the MechSE department have always been very helpful and friendly. I pointedly want to thank Kathy Smith for her patient guidance through the various stages of my doctoral study. Working as a teaching assistant has taught me valuable lessons in patience and humility; I am deeply thankful to the MechSE department for granting me this experience.

I express my thanks to all my friends at Champaign-Urbana, who have made life outside of work enjoyable. Special thanks go to two very close friends of mine – Harishankar Manikantan and Bindu Jagannatha – who have been the source of countless discussions on life, the universe and everything. Their love and support has without doubt made me a better person over the years.

My warmest thanks to Shreya for her limitless affection and for being an immense source of emotional support through my graduate years. Finally, I would like to thank my family for their unwavering love and affection, and their steadfast encouragement. Thanks *Amma*, for everything.

Table of Contents

List of Figures

Chapter 1

Introduction

1.1 Microfluidics

In a broad sense, microfluidics refers to the control and manipulation of fluid flows at length scales that range from 100 nm to 1 mm. In current usage, the term applies primarily to applications involving fluid flows in micron-scale flow geometries that are designed in order to carry out specific engineering or scientific tasks [24]. Microfluidics has a wide range of engineering applications from micromanufacturing processes to biomedical engineering and microfluidic fuel cells, as well as more fundamental scientific uses, such as the study of the biomechanics of DNA and swimming microorganisms [4, 12, 24, 124]. The wide range of applications is complemented by the low cost of manufacture (thanks to techniques borrowed from the electronics industry), making microfluidics an attractive and practical flow actuation method.

From a technical standpoint, microfluidic flows are characterized by the dominance of surface forces, which scale as L^2 (L being some characteristic length scale), over body forces, which scale as L^3 [12, 24, 99]. At the same time, the length scales are large enough that continuum descriptions of physical phenomena are still applicable. This in contrast to *nanofluidics*, which deals with flows over nanometer length scales, where (i) continuum models of matter may not adequately describe observed physical phenomena and (ii) thermal fluctuations or quantum phenomena may be important [16, 95]. This places microfluidics in a distinct position where classical physical descriptions are still applicable, but with very different effects compared to macroscopic flows, affording fluid control by exploiting surface tension, electromagnetic and acoustic fields, optical forces, etc.

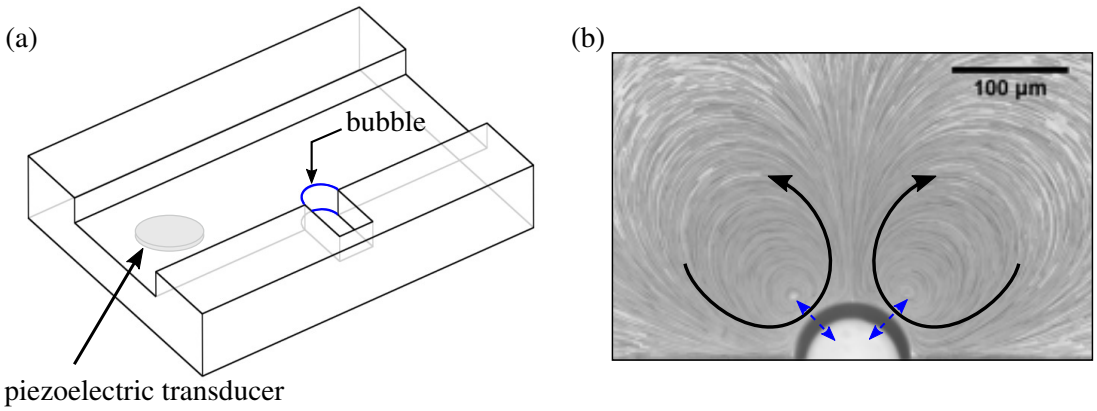

Figure 1.1 (a) Schematic of experimental set-up showing a bubble of semi-cylindrical shape trapped in a side channel of a main microfluidic channel. A piezoelectric transducer mounted on the same substrate as the device establishes an ultrasound pressure field (typically 10 - 100 kHz) which excites oscillations of the bubble interface. (b) Experimental image showing a section of the channel perpendicular to the axis of the bubble (dark semicircular outline), with dashed blue arrows indicating the fast oscillatory motion of its interface. The primary oscillatory motion is rectified into secondary steady currents (streaming), typically confined to planes parallel to the bubble axis and visualized here using tracer particles (1 µm diameter). The orientation of the streaming is indicated by solid black arrows.

1.2 Acoustically driven microbubbles as flow actuators

The excitation of an oscillatory flow in a viscous fluid gives rise to steady secondary currents, termed in general as "streaming". Such secondary flows may be actuated either by the propagation of sound through a medium, or by the oscillations of a boundary relative to its surrounding fluid, and are driven by non-zero Reynolds stresses due to the inertia of the fluid oscillation [30, 46, 47, 86].

A simple and robust method of driving streaming in microfluidic devices is through the acoustic excitation of microbubbles that have been positioned at walls of the device. The bubble undergoes both shape and volume oscillations in response to the ultrasound, establishing boundary layers that ultimately drive steady streaming in the entire bulk of the medium [90, 110, 112]. Such setups have been used with a great degree of success in several practical applications such as particle trapping [51, 87, 110], size-selective particle sorting [110, 111], microfluidic mixing [2, 44, 112], and shear force actuation [55].

Due to the ease of flow control and manufacture using lithography techniques, experimental designs have focused in recent years on two-dimensional geometries, where the bubble has a semi-

cylindrical shape and is sessile on the wall of the device [90, 112]. Figure 1.1(a) shows a schematic of the setup, indicating the outline of the bubble and figure 1.1(b) depicts the steady streaming as viewed in a cross-sectional plane perpendicular to its axis. It has been shown that these setups drive flows that appear to be confined to planes perpendicular to the bubble axis over timescales of practical interest in several applications [110, 111]. While such setups have been successfully employed in applications, their design has to a large extent been empirically driven, due to an absence of a theory connecting the applied ultrasound (frequency and amplitude) to the interface oscillations, and ultimately the steady secondary flow [2, 33, 44, 120].

1.3 Organization of the dissertation

The dissertation is broadly divided into two parts. In the first part of the dissertation (chapters 2–4) we develop of a rigorous asymptotic theory of the steady streaming due to a sessile microbubble of semi-cylindrical shape, in the limit of small oscillation amplitude. The asymptotic framework has two main advantages over direct numerical simulations in such flows. First, it provides fundamental physical insights into the mechanisms of flow excitation, and second, it is a versatile general formalism applicable to wide range of practical scenarios. In the second part of the dissertation (chapters 5 and 6), we demonstrate the practical utility of the asymptotic flow theory by applying it directly to two practical applications of general interest in microfluidics: particle sorting and manipulation, and microfluidic mixing. The contents of the individual chapters are summarized below.

In Chapter 2, we describe the two-dimensional oscillation dynamics of a sessile semicylindrical bubble in response to an applied driving frequency. We show here that the interface may be described as a multi-mode linear oscillator, whose mode spectrum is governed by two physical parameters: a dimensionless frequency, and a dimensionless damping parameter. In Chapter 3, we build on the results of the previous chapter and develop an asymptotic theory of the two-dimensional steady streaming, providing quantitative predictions for the flow fields over a wide range of driving frequencies. Chapter 1 and 2 therefore complete a self-consistent 2D description of both primary (oscillatory) and secondary (steady) flow fields, which agree quantitatively with experimental measurements.

Chapter 4 revisits the assumptions of two-dimensional streaming theory, motivated by Astig-

matism Particle Tracking Velocimetry (APTV) experiments, which show that while the 2D flow description is accurate at intermediate time scales (typically $\sim$ 100 ms), three-dimensional effects are important on both shorter ($\sim$ 1 ms) and longer ($\sim$ 1000 ms) time scales. We argue that these effects are excited due to the presence of axially confining walls, and show that a superposition of the 2D streaming theory with additional axial Stokes solutions accounts for both of these effects. We then develop a general Hamiltonian description of the long-time motion with broader applicability to flow superpositions in confined geometries outside of streaming phenomena.

Having developed a description of the flow field over a wide range of time scales, we focus in the next two chapters on practical applications. In Chapter 5, we address the problem of open-flow (continuous throughput) mixing, where we seek to achieve exponentially fast mixing by using an array of microbubbles in the microchannel. Using the theoretical streaming solutions, we show here that global transport properties of the streaming enable the identification of flow modulation strategies that maximize the rate of mixing of the fluid as it flows through the channel. In Chapter 6, we study the transport of finite-sized microparticles under a superposition of streaming and Poiseuille flows, focusing on the use of microbubbles for the continuous size-dependent sorting of microparticles. We advance a geometric argument which allows us to predict the deflection of particles, and show that the 3D flow effects are important in the quantitative description of sorting process.

1.4 Key Accomplishments

The key accomplishments of the research are organized into separate projects. Each project represents both a set of related technical ideas as well as a key step in furthering the understanding of microbubble streaming and its applications.

- **Asymptotic theory of two-dimensional oscillation dynamics and streaming:** We develop here, for the first time, a rigorous self-consistent theory of steady microbubble streaming, using only properties of the acoustic driving field as inputs. Focusing on microbubbles of semi-cylindrical shape, we (i) first resolve the oscillation dynamics of the bubble interface in response to applied pressure, which (ii) then feed into a theory of the secondary steady

streaming. Both the primary (oscillatory) and secondary (steady) flow components fully resolve leading order boundary layer effects over rigid walls (no-slip) and the bubble interface (stress-free), using only the driving frequency and damping parameter as inputs.

- **Three-dimensional effects under confinement:** We show here that axial confinement of the bubble modifies the 2D steady streaming, resulting in 3D fluid motion, modeled through a superposition of the 2D streaming theory with axial Stokes flow solutions. The 3D theory provides qualitative agreement with experimental observations, and also predicts 3D flow effects in streaming due to oscillating rigid cylinders in microfluidic environments. We develop a Hamiltonian theory of the topology and kinematics of such 3D flows, valid more generally for arbitrary perturbations of 2D flows under confinement. This forms the first quantitative description of three-dimensional flow effects in streaming flows in any system.

- **Continuous throughput micromixing:** We study optimal mixing protocols in bubble-based micromixers with continuous throughput, using a superposition of bubble streaming and a Poiseuille transport flow. We show first that in the limit of zero diffusion, a modulation of the flow is necessary to achieve rapid (exponentially fast) mixing, which is achieved here using a duty cycling of the streaming flow. We identify optimum duty cycling protocols using numerical simulations, which can be understood theoretically using global transport properties of the streaming and Poiseuille flows. The study builds towards a more systematic design of open flow micromixers that is based on simple transport properties of the flows involved.

- **Particle trajectories and size-dependent sorting:** We quantify the behavior of finite-sized microparticles near the bubble in the presence of transport (Poiseuille) flow for a fast, size-based sorting of microparticles. In order to achieve size-sensitive sorting of particles, differential (size-dependent) motion of particles *across* fluid streamlines is in general required. We argue that such a differential motion may be explained in part by assuming short range hard-core interactions (contact forces) between particle and bubble surfaces, but that a purely 2D flow description underpredicts the extent of sorting observed in experiments. Ultimately, we show that 3D effects play an important role in the sorting process, and are able to accurately quantify the sorting properties of experimental microbubble-based sorting devices.

Chapter 2

Oscillatory response of cylindrical bubbles

In this chapter[1], we develop a theoretical description of the interfacial oscillations of a semicylindrical bubble in contact with a side-wall of a microfludiic device. As the streaming flow patterns are caused by oscillations of microbubbles in contact with walls of the set-up, an understanding of the bubble dynamics is crucial. Here we characterize the oscillation modes and the frequency response spectrum of such cylindrical bubbles, driven by a spatially uniform temporally oscillating pressure field resulting from ultrasound in the range of $1\,\mathrm{kHz} \lesssim f \lesssim 100\,\mathrm{kHz}$. We find that (i) the appearance of 2D streaming flow patterns is governed by the *relative* amplitudes of bubble azimuthal surface modes (normalized by the volume response), (ii) distinct, robust resonance patterns occur independent of details of the set-up, and (iii) the position and width of the resonance peaks can be understood using an asymptotic theory approach. This theory describes, for the first time, the shape oscillations of a pinned cylindrical bubble at a wall and gives insight into necessary mode couplings that shape the response spectrum. We then briefly explore some modifications of the flow due to changes in geometry; specifically we explore (i) the effect of the channel height on the oscillatory flow field, and (ii) the effect of the rest shape of the bubble on its oscillation dynamics.

2.1 Introduction

The use of acoustic waves ranging from audible frequency to ultrasound in microfluidic environments (denoted by the term *acoustofluidics*) has enabled versatile manipulation of fluid, as well as of micro/nano-sized objects such as particles, bubbles, and cells [22]. Ultrasound standing waves in the MHz range have been used to trap and separate cell/particles [37] through acoustic radiation forces, which can move the suspended particles/cells to different lateral positions within a laminar

[1]This chapter is partly adapted from Wang et al. [112].

stream. Surface acoustic waves (SAWs) of order 100 MHz, which actuate on the fluid as a whole, have demonstrated several practical applications as well, with examples including cell and droplet sorting [20, 21], free surface liquid pumping [122], and concentration of particles [103]. The operation frequency range of the above mentioned methods must be high enough to have acoustic wavelengths comparable to the length scale of cell/particle or microdevices, or to generate momentum flux to move the liquid directly. The potentially undesirable effects are the relatively high power consumption and temperature rise due to heat generation, which may be a concern for biological samples sensitive to temperature. In addition, they both require precise fabrication, such as arrangements of interdigitated structures [20, 21, 103].

Acoustic streaming, a classical phenomenon of driving fluid using sound, has found many useful applications at the microscale over the last decade. As pointed out by other researchers [22, 85, 86], a distinction must be made between two general types of streaming: one being a result of attenuation of energy into the fluid during sound propagation (e.g. "quartz wind"), and the second being due to the Reynolds stresses within a thin boundary layer (known as boundary-induced *steady streaming*). The former type of acoustic streaming needs to operate in the MHz range to drive steady currents in water [68]. By contrast, boundary steady streaming can be used at a much lower driving frequency to generate steady flows [49, 55]. While it is possible to integrate vibrating suspended microstructures [40, 41] into a micro-device to induce streaming, such an approach is usually very complex in microfabrication. An alternative way is to induce fluid oscillation over solid objects [50, 51], which is often limited by the low oscillation frequency and small streaming velocity.

Ultrasound-driven oscillating microbubbles serve as excellent actuators to induce microscale steady streaming, offering several advantages such as simple manufacture, easy integration into microfluidic system, and large oscillatory amplitude and thus larger streaming velocity. Protruding air pockets can form spontaneously from indentations in 3D [55, 56, 65, 88] or from blind side channels in 2D set-ups [1, 73, 110, 111], see figure 2.1. A commercially available piezoelectric transducer can be easily glued anywhere on the substrate to provide excitation, as the direction of acoustic waves is immaterial, in contrast to standing wave or SAW techniques. The compressibility of the bubble enables interface oscillations of large amplitude ϵa with $\epsilon \gtrsim 0.05$, where a is the bubble radius. In the last few years, many microfluidic applications based on bubble streaming have been

developed, including mixing enhancement [1, 114], particle sorting and switching [73, 110], and particle focusing and enrichment [111].

However, a fundamental understanding of microbubble streaming flow lags behind experimental progress. While general theories exist for streaming induced by oscillatory flow over no-slip surfaces [70], or for bubble-induced streaming in bulk fluid [11, 47], the particular situation in practical devices (figure 2.1) is complicated by the combination of (i) the no-stress bubble boundary condition, (ii) the deformability of the bubble interface, (iii) the contact line between the bubble interface and the wall, and (iv) the necessity of matching the oscillatory boundary layers around the bubble and at the wall. Elder [17] in his pioneering work already described the rich and complex flow patterns from a 3D oscillating hemispherical bubble attached to a wall, submerged in liquids of different viscosities. Tho *et al.* reported experimental investigations of flow fields from 3D hemispherical bubbles confined between two plane walls [106]; in this geometry, qualitative and semiquantitative descriptions emerged [56, 57], but without accounting for the problems (iii) and (iv) above. In contrast to these studies, microfluidic devices often have 2D planar geometry due to the lithography-based microfabrication technique, so that 2D microbubbles (menisci) are more commonly encountered in practical microfluidics applications [1, 73, 110, 111, 121].

Here, we study the oscillations of a 2D bubble sandwiched between two plane walls (figure 2.1) and attached to a solid side wall under different driving frequencies, as well as the flow patterns arising from the bubble dynamics. The secondary steady streaming flow is the time-averaged result of the interaction of first order oscillatory flows, which in turn are caused by the oscillating bubble. The bubble oscillation dynamics coupled with the oscillatory flow field are computed using a matched asymptotic expansions, and are compared with experimental data of interface shape, obtained by high-speed imaging.

2.2 Experimental setup and motivation

We briefly describe the experimental setup used here and in subsequent chapters; the setup is similar to the ones previously described [110, 111], schematically shown in figure 2.1. The microfluidic channel is made of Polydimethylsiloxane (PDMS) using soft lithography [62], and is then bonded at the substrate slide (either glass or polystyrene). The microfluidic device has a main channel with

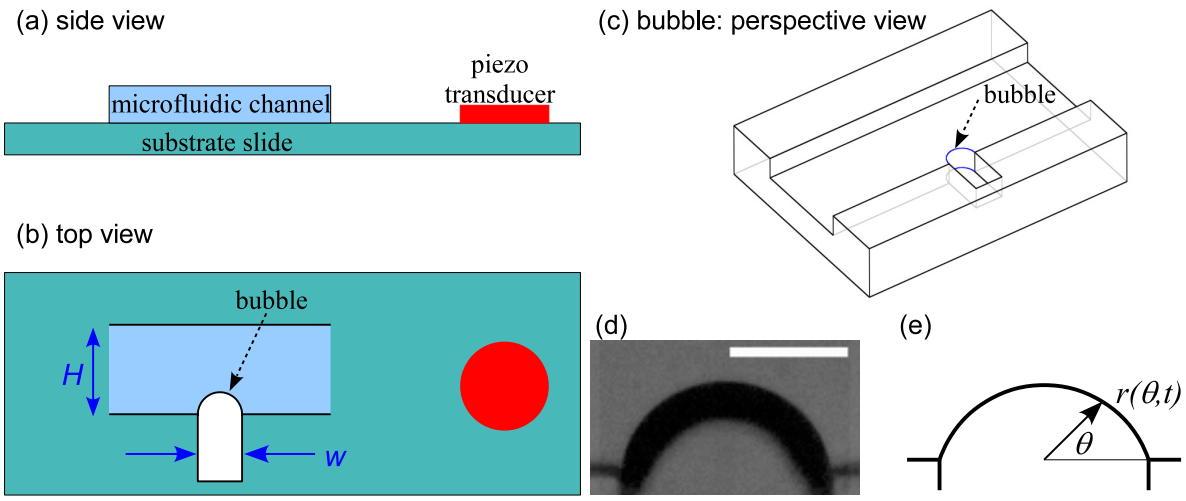

Figure 2.1 Schematic of experimental set-up (not to scale): (a) and (b) show the side view and top view; (c) a perspective view of the semicylindrical bubble; (d) a snapshot of the undisturbed bubble (scale bar is 50 μm); (e) coordinate system used to measure the bubble shape.

a depth of $D = 100\,\mu\text{m}$ and height in the image plane of $H = 1000\,\mu\text{m}$, and a side channel with a opening of $w \approx 80\,\mu\text{m}$ wide (figure 2.1(b)). The introduction of an aqueous glycerol solution (23% glycerol by weight) into the main channel through a syringe pump (via inlets of the channel) traps an air bubble of approximately semi-cylindrical shape in the side channel, protruding into the main channel (figure 2.1(c)). The bubble therefore has a nominal radius $a \approx w/2 \approx 40\,\mu\text{m}$, and an axis that spans the entire depth D of the channel.

A piezoelectric transducer glued to the glass slide provides ultrasonic excitation of the bubble, using sinusoidal signals of frequency $f = 1 - 100\,\text{kHz}$. Streak photographs of the streaming are obtained by superposition of typically 1000 successive images at a frame rate of 1000 fps. To study the dynamics of the bubble interface, we capture images at 100,000 fps and with an exposure time of $1\,\mu\text{s}$ (figure 2.1(d)).

We focus in this chapter on quantifying the high-speed oscillations of the interface. We will show that information about the bubble motion in the radial-azimuthal plane (figure 2.1(e)) is sufficient to explain its behavior, i.e., oscillations in the direction of the axis of the cylindrical bubble have negligible effect and both the bubble surface oscillations and the resulting flow fields can be understood as two-dimensional dynamics in the radial-azimuthal plane. Below, we present both experimental evidence and theoretical justification for this treatment of the problem as an

oscillating 2D bubble.

The shape of the initially undisturbed bubble is in general described by $r_0(\theta) \equiv r(\theta, t = 0)$, where $r(\theta, t)$ is the instantaneous bubble shape during excitation, measured in polar coordinates from an origin at the center of the side channel opening, as shown in figure 2.1(e). The θ-dependent amplitude of the bubble is then characterized by

$$\Delta r(\theta, t) = r(\theta, t) - r_0(\theta).$$

Since the camera frame rate is comparable to the oscillation frequency, we chose it so that information about the oscillation dynamics can be reconstructed stroboscopically [112]. For linear oscillations of the bubble, the interface oscillation frequency is equal to the driving frequency (we show that this is true both from experimental data and theoretical modeling). For the purpose of analysis, it is useful to decompose $\Delta r(\theta, t)$ into a Fourier series

$$\Delta r(\theta, t) = a \sum_{n=0} a_n \cos(2n\theta) \sin(\omega t + \phi_n), \tag{2.1}$$

where $\omega = 2\pi f$ is the angular frequency. a_n are then the dimensionless mode amplitudes, and ϕ_n the phase angles. The decomposition into cosines is suggested by the symmetry of the interface and the presence of the wall, and can be directly used to infer the oscillatory flow field, as we show in following section 2.4.

2.2.1 Frequency response of interface shape and streaming

To motivate the theoretical discussion of the interface dynamics and the streaming, we briefly summarize some key experimental findings. First, it is important to note that in a practical situation, the experimenter has no control over the shape of the bubble. Rather, the interface oscillation shape is determined as a part of a dynamical response to the applied ultrasound field. For a driving frequency of $f = 20$ kHz, the wavelength of the ultrasound, assuming that the speed of sound in water is $c \approx 1500$ ms^{-1} is approx $\lambda_{ultrasound} = c/f \approx 7.5$ cm, much greater than the typical height of microbubbles in microfluidic devices ($\sim 50\,\mu$m). On the scale of the bubble, the applied ultrasound takes the form of an approximately spatially uniform, temporally oscillating pressure

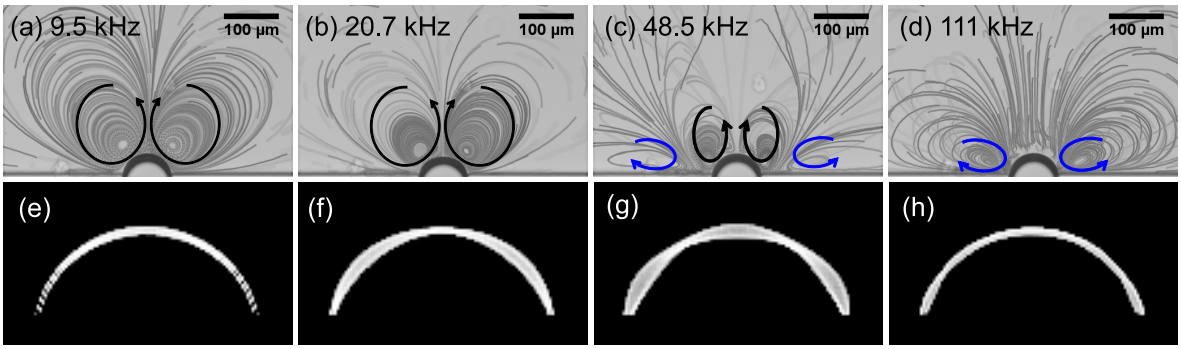

Figure 2.2 The upper row (a–d) shows bubble streaming flow patterns at different driving frequencies, with arrows indicating the orientations of the vortices. The lower row shows outlines of oscillatory bubble superposed over one cycle at different frequencies: (e) 9.6 kHz, (f) 20.6 kHz, (g) 48.6 kHz and (h) 100.3 kHz.

field.

For a free bubble (a bubble suspended in bulk fluid) driven by such a time-varying pressure, only radially uniform volume oscillations (the monopole oscillation mode) is excited effectively, and is done so separately from any shape modes. This is however not the case for a bubble located at a side channel opening, where shape and volume modes have to be excited together to accommodate pinning of the contact line. A range of interface oscillations shapes may therefore be accessed as a function of the frequency of the driving ultrasound, as shown in figure 2.2(e)–(h). Shape oscillations of the interface drive oscillatory motion of the fluid, which becomes rectified into a steady streaming, which is then also frequency dependent, see figure 2.2(a)–(d).

In general, these is a succession of steady flow patterns, as shown in figure 2.2. At lower frequencies (figure 2.2(a)–(b)), there are two symmetric vortices above the bubble, drawing liquid towards the bubble and pushing liquid upwards along the pole of the bubble. We denote this pair as "*fountain*" vortices or loops. This flow pattern has been described as the "generic" streaming pattern near an interface, both in the present 2D set-up [1, 110] and (as an analogous toroidal vortex loop) for 3D hemispherical bubbles [17, 55, 56]. As f increases in our set-up, a second pair of vortices is observed to appear, with orientation opposite ("*anti-fountain*") to the first pair (see figure 2.2(d)). With even higher driving frequencies, the anti-fountain vortices dominate over the fountain vortices (see figure 2.2(d)), reversing the far-field flow pattern.

Two questions arise naturally from the experimental observations of figure 2.2: (i) how are the

interface oscillation shapes determined, and (ii) how are the interface oscillation dynamics connected to the steady secondary flows that are of practical interest? We answer both of these questions in this chapter and the next by developing a rigorous perturbation theory that takes into account (i) the moving interface, (ii) boundary conditions at both the bubble and the walls, and (iii) the dynamic response of the bubble to the applied ultrasound.

2.3 General theoretical formalism for primary and secondary flows

We first describe the well-established general theoretical formalism for primary (oscillatory) and secondary (steady) components of the flow, valid for small amplitude oscillations of a compact object [86]. For a fluid of density ρ and kinematic viscosity ν, the Navier–Stokes equations for incompressible flow are

$$\frac{\partial \boldsymbol{u}}{\partial t} + (\boldsymbol{u}\cdot\boldsymbol{\nabla})\boldsymbol{u} = -\frac{\nabla p}{\rho} + \nu\nabla^2\boldsymbol{u}, \tag{2.2}$$

$$\nabla\cdot\boldsymbol{u} = 0, \tag{2.3}$$

wher $\boldsymbol{u}(\boldsymbol{x},t)$ is the velocity field, $p(\boldsymbol{x},t)$ the pressure.

Now consider the excitation of the fluid through the oscillatory motion of a compact object of characteristic size a, oscillating at a frequency f. The kinematic condition at the surface of the object induces an oscillatory motion of the surrounding fluid. If the dimensionless amplitude of oscillation relative to the size of the object is ϵ, then the characteristic oscillatory flow speed is

$$U_0 = \epsilon a\omega, \tag{2.4}$$

where $\omega = 2\pi f$ is the angular frequency. Using a, ω^{-1} and U_0 as characteristic length, time and velocity scales, and $\rho a\omega U_0$ as the characteristic pressure scale, the dimensionless Navier–Stokes equations read

$$\frac{\partial \boldsymbol{u}}{\partial t} + \epsilon(\boldsymbol{u}\cdot\boldsymbol{\nabla})\boldsymbol{u} = -\nabla p + \frac{\delta^2}{2}\nabla^2\boldsymbol{u}, \tag{2.5}$$

$$\nabla\cdot\boldsymbol{u} = 0, \tag{2.6}$$

where

$$\delta \equiv \sqrt{\frac{2\nu}{a^2\omega}}. \tag{2.7}$$

Here δ may be interpreted as a dimensionless boundary layer thickness, and will play an important role in the subsequent analysis.

In most practical applications, the amplitude of oscillations is small compared to the size of the compact object, i.e. $\epsilon \ll 1$. The equations may be solved by means of a regular asymptotic expansion of the dimensionless flow field in powers of ϵ:

$$\boldsymbol{u}(\boldsymbol{x}, t) = \boldsymbol{u}_0(\boldsymbol{x}, t) + \epsilon \boldsymbol{u}_1(\boldsymbol{x}, t) + ... \tag{2.8}$$

The pressure field follows a similar expansion. In typical microfluidics applications, the boundary layer thickness is also usually small due to the high frequencies used (in the kHz - MHz range). If we assume that the following inequality holds:

$$\epsilon \ll \delta \ll 1, \tag{2.9}$$

the flow can be solved for by means of two linear systems for $\boldsymbol{u}_0$ and $\boldsymbol{u}_1$, readily obtained by inserting (2.8) into (2.5). The primary flow is governed by

$$\frac{\partial \boldsymbol{u}_0}{\partial t} = -\nabla p_0 + \frac{\delta^2}{2}\nabla^2 \boldsymbol{u}_0, \tag{2.10}$$

$$\nabla \cdot \boldsymbol{u} = 0, \tag{2.11}$$

and the secondary flow by

$$\frac{\partial \boldsymbol{u}_1}{\partial t} + \nabla p_1 - \frac{\delta^2}{2}\nabla^2 \boldsymbol{u}_1 = -(\boldsymbol{u}_0 \cdot \boldsymbol{\nabla})\boldsymbol{u}_0, \tag{2.12}$$

$$\nabla \cdot \boldsymbol{u}_1 = 0, \tag{2.13}$$

For a purely oscillatory forcing, the primary flow field $\boldsymbol{u}_0$ is oscillatory at the driving angular frequency ω, and therefore has zero time average over a cycle of the oscillatory motion. The secondary flow $\boldsymbol{u}_1$ however contains in general both steady and oscillatory contributions due to the

forcing term, which is quadratic in $\boldsymbol{u}_0$. The governing equations for the steady part of the secondary Eulerian flow field are obtained by a time average of (2.12), and are

$$\frac{\delta^2}{2}\nabla^2 \langle \boldsymbol{u}_1 \rangle - \nabla \langle p_1 \rangle = -\langle (\boldsymbol{u}_0 \cdot \boldsymbol{\nabla})\boldsymbol{u}_0 \rangle , \tag{2.14}$$

$$\nabla \cdot \langle \boldsymbol{u}_1 \rangle = 0, \tag{2.15}$$

where $\langle \cdot \rangle \equiv (2\pi)^{-1} \int_0^{2\pi} \mathrm{d}t$ denotes the time average. Note that the steady component of the flow is governed by an inhomogeneous Stokes equation (the inertia of $\boldsymbol{u}_1$ is unimportant), with the forcing term determined only by the inertia of the oscillatory flow. We will commonly refer to this forcing as the "Reynolds stress term"; formally $\boldsymbol{u}_0 \cdot \boldsymbol{\nabla} \boldsymbol{u}_0$ is proportional to the divergence of the Reynolds stress tensor, given in dimensional units as $\boldsymbol{R} = \rho U_0^2 \boldsymbol{u}_0 \boldsymbol{u}_0$.

In most practical applications, one is interested in the time averaged *Lagrangian* motion of the fluid through the unsteady velocity field $\boldsymbol{u}(\boldsymbol{x}, t)$. It is relatively straightforward to show that to the order of accuracy that is retained in the flow description, the time averaged Lagrangian fluid motion due to $\boldsymbol{u}(\boldsymbol{x}, t)$ is equivalent to advection through the steady velocity field

$$\boldsymbol{U}(\boldsymbol{x}) = \langle \boldsymbol{u}_1 \rangle + \boldsymbol{u}_d, \tag{2.16}$$

where

$$\boldsymbol{u}_d(\boldsymbol{x}) \equiv \left\langle \left(\int \boldsymbol{u}_0 \mathrm{d}t \cdot \boldsymbol{\nabla} \right) \boldsymbol{u}_0 \right\rangle \tag{2.17}$$

is called the Stokes drift [46, 81, 86]. This Lagrangian fluid motion is the quantity that is in practice referred to as "streaming" and is quadratic in the oscillation amplitude (as are $\langle \boldsymbol{u}_1 \rangle$ and $\boldsymbol{u}_d$). Note that the Stokes drift is identically divergence free ($\nabla \cdot \boldsymbol{u}_d = 0$), making the Lagrangian streaming also divergence free ($\nabla \cdot \boldsymbol{U} = 0$). The time averaged Lagrangian fluid motion is therefore governed by a steady incompressible velocity field; this is a useful property of the streaming which is exploited in subsequent chapters.

The characteristic velocity scale of the streaming is

$$U_s = \epsilon^2 a\omega = \epsilon U_0, \tag{2.18}$$

with a characteristic streaming Reynolds number

$$Re_s \equiv U_s a/\nu = 2\epsilon^2/\delta^2 \ll 1.$$

Streaming flows for which $Re_s \ll 1$ are typically referred to as Reyleigh–Nyborg–Westerwelt (RNW) streaming (this is equivalent to the condition $\epsilon \ll \delta$), and are easily accessed in microfluidics. If this condition is violated, the convective inertia of the secondary flow is not negligible, requiring the governing equations for the secondary flow to be modified [84, 86, 101].

2.4 Theory of cylindrical bubble oscillations

The flow patterns and their symmetries depend on the resonance structure of the bubble shape oscillations. The resonance behavior of free bubbles has long been known [38, 75], and other work has treated oscillations of hemispherical droplets[52, 108], and hemispherical bubbles on solid supports [18]. In many microfluidic devices, as in ours, the bubble is confined by two parallel supporting walls to which it is attached via large contact areas, thus assuming a cylindrical symmetry (it is verified experimentally that these contact areas are immobile). It is additionally pinned to rigid walls by means of two contact lines that span the depth of the bubble along the z-axis (figure 2.3a). This practically relevant case, i.e., that of a bubble whose interface is part of a cylinder, attached to a wall along contact lines, has not previously been treated. We will see that the resonance features of the bubble oscillation can be understood within an asymptotic theory framework that accounts for the coupling of azimuthal modes through the boundary conditions.

We consider here an idealization of the experimental set-up: a cylindrical bubble of radius a confined between parallel plates of distance D, and pinned to a wall by means of two contact lines, as shown in figure 2.3. We will assume that this wall is smooth, rigid, and no-slip, and that the contact lines between the bubble surface and the wall remain stationary. A polar coordinate system coaxial with the bubble is used, with the walls at $\theta = 0$ and $\theta = \pi$. We consider the situation where the surface of the bubble undergoes oscillations at a single angular frequency ω with a characteristic dimensionless amplitude ϵ, producing a characteristic oscillatory velocity $U_0 = \epsilon a\omega$ of the surrounding fluid.

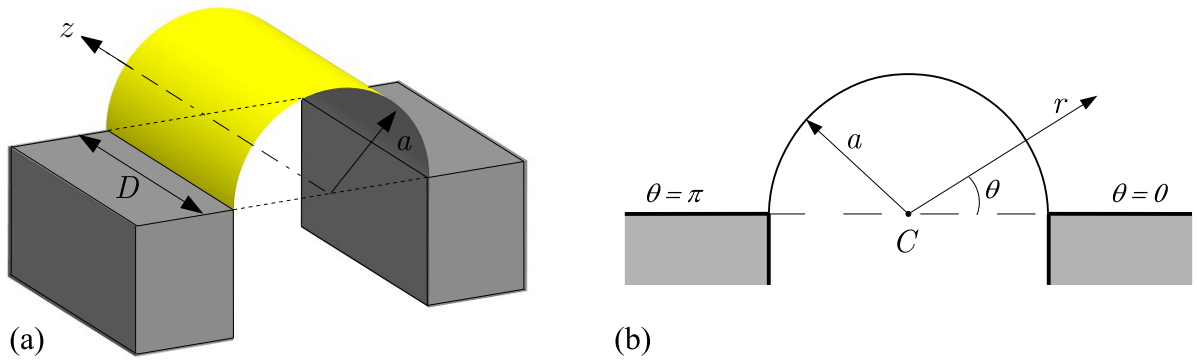

Figure 2.3 (a) Geometry of the cylindrical bubble confined between plates a distance D apart. (b) Coordinate system of the 2D geometry used in the calculation of bubble oscillations.

For $\epsilon \ll 1$, the flow, to leading order, is described by the linearized Navier–Stokes equations, and being driven by surface oscillations of the bubble, shares the same angular frequency ω. For the purpose of analysis, we first neglect axial oscillations of the bubble surface, and assume that the bubble is initially semi-cylindrical. Using a and ω to normalize length and time respectively, the shape of the oscillating interface is given in general by

$$R(\theta, t) = 1 - \mathrm{i}\epsilon \mathrm{e}^{\mathrm{i}t}\zeta(\theta), \tag{2.19}$$

where only the real part of any equality is physically meaningful, and $\zeta(\theta)$ is some complex function of $O(1)$ magnitude.

Within the two-dimensional description, it is useful to introduce a dimensionless stream function $\psi(r, \theta, t)$ (written in units of $U_0 a$) that gives the components of velocity in the plane

$$u_r = r^{-1}\partial\psi/\partial\theta, \quad \text{and} \quad u_\theta = -\partial\psi/\partial r,$$

or more generally as $\boldsymbol{u} = \nabla \times (\psi\hat{\boldsymbol{z}})$. The stream function is a useful mathematical tool for 2D flows that we will continue to use through the dissertation. We will show in chapter 4 that it is also useful in understanding 3D fluid motion in confined geometries.

In the present chapter, we consider only the primary oscillatory components of the flow, corresponding to (2.10). Formally, we are interested in the leading order flow ψ_0 in an asymptotic expansion of ψ in powers of ϵ analogous to (2.8): $\psi \sim \psi_0 + \epsilon\psi_1$. For notational convenience, we

drop the subscript 0 for the remainder of this chapter.

The governing equation for ψ is the linearized form of the 2D vorticity equation — the curl of the (2.10) — which may be written as

$$\left(\frac{\partial}{\partial t} - \frac{\delta^2}{2}\nabla^2\right)\nabla^2\psi = 0. \tag{2.20}$$

If it is assumed that the time dependence of all oscillatory quantities is proportional to $\mathrm{e}^{\mathrm{i}t}$ (the system is linear to first approximation), the governing equation for ψ becomes

$$(\nabla^2 - \alpha^2)\nabla^2\psi = 0, \tag{2.21}$$

where $\alpha = (1+\mathrm{i})/\delta$, with $\delta = a^{-1}\sqrt{2\nu/\omega}$ being the Stokes boundary layer thickness.

We assume that the bubble interface $R(\theta,t) = 1 - \mathrm{i}\epsilon\zeta(\theta)\mathrm{e}^{\mathrm{i}t}$ is impermeable and stress-free. These boundary conditions may be imposed, to leading order in ϵ, at the mean position of the bubble (cf. appendix A) and read

$$\left.\begin{aligned} &\epsilon\frac{1}{r}\frac{\partial\psi}{\partial\theta} = \dot{R} = \epsilon\,\zeta(\theta)\mathrm{e}^{\mathrm{i}t} \\ &\frac{\partial^2\psi}{\partial r^2} - \frac{1}{r}\frac{\partial\psi}{\partial r} - \frac{1}{r^2}\frac{\partial^2\psi}{\partial\theta^2} = 0 \end{aligned}\right\} \quad \text{on} \quad r = 1. \tag{2.22}$$

In addition, the flow must be no-slip on the rigid walls at $\theta = 0$ and $\theta = \pi$, given by

$$\frac{1}{r}\frac{\partial\psi}{\partial\theta} = \frac{\partial\psi}{\partial r} = 0 \quad \text{on} \quad \theta = 0 \quad \text{on} \quad \theta = \pi. \tag{2.23}$$

Separable solutions to (2.21) of azimuthal wave number k are readily obtained as

$$\psi_k(r,\theta) = \hat{\psi}_k(r)\exp(\mathrm{i}k\theta)\,\mathrm{e}^{\mathrm{i}t} = \left(\frac{C_k}{r^k} + D_k\mathrm{K}_k(\alpha r)\right)\exp(\mathrm{i}k\theta)\,\mathrm{e}^{\mathrm{i}t}, \tag{2.24}$$

where k may assume any complex value with a non-negative real part. The corresponding bubble shape ζ is given by the kinematic boundary condition, as

$$\zeta_k(r,\theta) = \hat{\zeta}_k(r)\exp(\mathrm{i}k\theta)\,\mathrm{e}^{\mathrm{i}t}, \quad \text{where} \quad \hat{\zeta}_k(r) = \mathrm{i}k\hat{\psi}_k(r). \tag{2.25}$$

The modified Bessel function of the second kind $\mathrm{K}_k(\alpha r)$ is an exponentially decaying vortical solution that persists only in the boundary layer, while the algebraically decaying term in (2.24) represents the potential flow solution, with a corresponding potential

$$\phi_k(r,\theta) = -\mathrm{i}\frac{C_k}{r^k}\exp(\mathrm{i}k\theta)\,\mathrm{e}^{\mathrm{i}t}\,. \tag{2.26}$$

If, by comparison, we take axial oscillations (along the coordinate z) into account as well, we find potential flow solutions by separation of variables [93, 94] as

$$\phi_{km}(r,\theta,z) = \mathrm{K}_k(mr)\exp(\mathrm{i}k\theta)\,\exp(\mathrm{i}mz)\,\mathrm{e}^{\mathrm{i}t} \tag{2.27}$$

where m is the dimensionless axial wave number. This solution replaces the power-law terms (2.26) for $m \neq 0$. Note that the modified Bessel function decay in (2.27) is much stronger as r grows away from the bubble surface, becoming exponential for $mr > 1$. As the smallest non-zero m is $m = 2\pi a/D$ (at least one axial wavelength must fit along D), this is fulfilled at even a fraction of a bubble radius away from the surface. The oscillatory flow field away from the bubble is therefore dominated by the two dimensional flow solutions given in (2.24). Additionally, we will show below that the expected excitation amplitude of the axial oscillation modes is significantly smaller than that of the azimuthal modes.

2.4.1 Theory of bubble resonance

While the general solutions (2.24) satisfy the kinematic boundary condition, determining coefficients C_k and D_k that satisfy both the stress-free condition at the bubble and the no-slip condition at the wall is not trivial. We address this problem by recognizing [103] that by temporarily relaxing the zero-tangential velocity at the boundary condition at the wall, the general solution (2.24) simplifies to a Fourier sine series, to which the no-stress boundary condition may be applied separately for each mode k, due to orthogonality properties of the series. Assuming symmetry of the bubble shape about $\theta = \pi/2$, we have a general solution ψ_b to this modified problem

$$\psi_b(r,\theta) = \sum_{n=0}^{\infty} A_n\left(\frac{c_{2n}}{r^{2n}} + d_{2n}\mathrm{K}_{2n}(\alpha r)\right)\sin 2n\theta\,\mathrm{e}^{\mathrm{i}t} \tag{2.28}$$

with c_k and d_k given by

$$c_k = \frac{1}{k} - d_k \mathrm{K}_k(\alpha) \quad \text{and} \qquad d_k = -\frac{2(k+1)}{\alpha^2\,\mathrm{K}_{k-2}(\alpha) + 2k\alpha\,\mathrm{K}_{k-1}(\alpha)}\,, \tag{2.29}$$

and the corresponding bubble shape $\zeta_b = \sum A_n \cos 2n\theta$. We have, in (2.28), constructed a general slip solution that is ignorant of viscous effects near the wall, which may then be employed as leading order 'outer solution' in a matched asymptotic expansion. The expansion in integer k reinforces the conclusion that slowly decaying solutions with exclusively azimuthal variation will dominate fast-decaying solutions with axial variation and result in 2D flow, as observed in experiment.

We now invoke the well known solution for an viscous oscillatory flow near a wall [46, 70, 86] in the limit of thin boundary layers ($\delta \ll 1$), composed of a wall boundary layer structure driven by an oscillatory slip. The stream function ψ_w in the boundary layer over the wall at $\theta = 0$ is given as

$$\psi_w(r,\xi) = \delta\, r\, v(r) \left\{ \xi - \frac{1}{r(1+\mathrm{i})} \left(1 - \mathrm{e}^{-(1+\mathrm{i})\xi r} \right) \right\} \mathrm{e}^{\mathrm{i}t} + O(\delta^3)\,, \tag{2.30}$$

with $\xi = \theta/\delta$ a rescaled azimuthal coordinate and $v(r)\,\mathrm{e}^{\mathrm{i}t}$ the oscillatory slip velocity at the edge of the wall boundary layer. Asymptotic matching of the wall boundary layer solution to the outer solution as $\xi \to \infty$, together with the symmetry of the bubble oscillations about $\theta = \pi/2$, enforces that k is a non-negative even integer. We may then write for the slip velocity

$$v(r) = \sum_{n=0}^{\infty} 2nA_n \frac{c_{2n}}{r^{2n+1}} = \sum_{n=0}^{\infty} \frac{A_n}{r^{2n+1}} + O(\delta^2), \tag{2.31}$$

where A_n are the (generally complex) weights of the different angular components of the flow field, and the approximation results from a δ-expansion of (2.29).

We have so far excluded the corner regions near the contact lines, in which the bubble and wall boundary layers overlap and where the wall boundary layer solution might become modified by radial gradients warranted by the no-stress bubble surface. However, an expansion in orders of δ of (2.24) verifies that the bubble boundary layer terms are absent up to the order to which the wall boundary layer solution (2.30) is valid, which enables the extension of (2.30) into the corner regions up to the bubble surface. We must still address any potential modification of the stress-free

condition at the bubble surface that could have been introduced by this extension. The tangential stress in the corner is readily calculated from (2.30) and (2.22) as

$$\frac{1}{\delta^2}\left(\delta^2\frac{\partial^2}{\partial r^2}-\delta^2\frac{1}{r}\frac{\partial}{\partial r}-\frac{1}{r^2}\frac{\partial^2}{\partial\xi^2}\right)\psi_w\Big|_{r=1}=\frac{1+\mathrm{i}}{\delta}v(1)\mathrm{e}^{-(1+\mathrm{i})\xi}+O(\delta) \tag{2.32}$$

Clearly, if the bubble surface is everywhere stress free, it must be true that

$$v\,(1)\sim\sum_{n=0}^{\infty}A_n=O(\delta^2) \tag{2.33}$$

We will henceforth ignore the bubble boundary layer for further calculations, but note its importance in maintaining a stress-free bubble surface. Using (2.24),(2.30), and(2.31), a uniformly valid solution for the oscillatory velocity field is then given as

$$\boldsymbol{u}(r,\theta)\sim\sum_{n=0}^{\infty}\frac{A_n}{r^{2n+1}}\Big[\left\{\cos 2n\theta-\left(\mathrm{e}^{-\alpha\theta r}+\mathrm{e}^{-\alpha(\pi-\theta)r}\right)\right\}\hat{\boldsymbol{r}}+\sin 2n\theta\,\hat{\boldsymbol{\theta}}\Big]\mathrm{e}^{\mathrm{i}t}, \tag{2.34}$$

Using the kinematic condition in (2.22), the bubble shape is described by

$$\zeta(\theta)=\sum_{n=0}^{\infty}A_n\left[\cos 2n\theta-\left(\mathrm{e}^{-\alpha\theta}+\mathrm{e}^{-\alpha(\pi-\theta)}\right)\right]. \tag{2.35}$$

It is worth noting that (2.35) implies pinned contact lines simply by virtue of the walls being strictly no-slip.

In the linear limit, the pressure field is a harmonic function and plays the role of a velocity potential in the bulk of the fluid, where the flow is irrotational. Using a pressure scale $\epsilon\rho a^2\omega^2$, the oscillatory pressure in the liquid is given by

$$P^e(r,\theta,t)=\mathrm{i}\epsilon\rho a^2\omega^2\left(p^*+A_0\log\frac{R_\infty}{r}+\sum_{n=1}^{\infty}\frac{A_n}{r^{2n}}c_{2n}\cos 2n\theta\right)\mathrm{e}^{\mathrm{i}t}\,. \tag{2.36}$$

Note that the pressure at infinity diverges logarithmically as a consequence of the assumption that the flow is two-dimensional, and may be regularized by assuming weak gradients in the axial direction. For the purpose of this discussion, we retain (2.36), and replace the limit $r\to\infty$ by $r\to R_\infty$, assuming that R_∞ is large enough that the pressure at $r=R_\infty$ associated with

the surface modes is negligible. p^* is then the non-dimensional uniform oscillatory pressure that persists at infinity, and may be externally imposed in the case of a long wavelength forcing, as in our experiments.

We now proceed to describe the bubble interfacial dynamics, and thus the coefficients A_n, as functions of the frequency of oscillation and the physical parameters of the system. At the bubble interface, the normal stress balance yields $\sigma^e_{nn} - \sigma^i_{nn} - \Gamma\kappa = 0$, where σ^e_{nn} and σ^i_{nn} are normal stresses on the interface due to the external and internal fluids, respectively, κ is the sum of the principal curvatures of the interface, and Γ is the surface tension coefficient of the interface. To leading order in ϵ, the unit normal at the surface is given by the unit vector in the radial direction and we have $\sigma^e_{nn} = \sigma^e_{rr} = -P^e + \tau_{rr}$, where P^e is external fluid pressure at the interface ($\zeta = 0$), and $\tau_{rr} = \epsilon\omega\mu\partial u_r/\partial r|_{\zeta=0}$ is the interfacial viscous normal stress due to the external fluid.

For a typical air bubble in water, the density and the dynamic viscosity of the interior gas is much smaller than the exterior liquid, so that stresses due to the gas dynamics may be neglected and the internal oscillatory pressure P^i follows the radius dynamics via a polytropic law of exponent η, $P^i \propto R^{-3\eta}$.

The curvature κ of the bubble interface may be calculated using (2.35),which yields to leading order in ϵ

$$\kappa(\theta, t) = \frac{\mathrm{i}\epsilon}{a}\left[\sum_{n=0}^{\infty} A_n(4n^2-1)\cos 2n\theta + (\alpha^2-1)\left(\mathrm{e}^{-\alpha\theta} + \mathrm{e}^{-\alpha(\pi-\theta)}\right)\sum_{n=0}^{\infty} A_n\right]\mathrm{e}^{\mathrm{i}t}. \tag{2.37}$$

If thermal and acoustic effects are negligible, the normal stress balance, rewritten as $P^i - P^e + \tau_{rr} - \Gamma\kappa = 0$, gives the dynamical equation describing the linear oscillations of the bubble, which may be recast as

$$-\omega^2\mathbb{P}(\theta) + 2\mathrm{i}\gamma\Omega\omega\mathbb{T}(\theta) + \Omega^2\mathbb{K}(\theta) + \Omega_v^2 A_0 = \omega^2 p^* \tag{2.38}$$

where $\Omega = \sqrt{\Gamma/\rho a^3}$, $\gamma = \mu/\sqrt{\rho a\Gamma}$, and $\Omega_v = \sqrt{\pi\eta P_0/\rho S_0}$.

Ω is an angular frequency scale for surface mode resonance, and Ω_v is a 2D Minnaert frequency describing volume resonance of a gas bubble with a rest cross-sectional area of S_0. $\mathbb{P}(\theta)$, $\mathbb{T}(\theta)$ and $\mathbb{K}(\theta)$ are the normal stress contributions of the pressure, viscous damping, and curvature,

respectively, and are given by

$$\mathbb{P}(\theta) = A_0 \log R_\infty + \sum_{n=1}^{\infty} A_n \left(\frac{1}{2n} - \mathrm{i}\,\delta^2(2n+1) \right) \cos 2n\theta, \tag{2.39}$$

$$\begin{aligned}\mathbb{T}(\theta) = &\sum_{n=0}^{\infty} A_n(2n+1)\Big[\cos 2n\theta - \left(\mathrm{e}^{-\alpha\theta} + \mathrm{e}^{-\alpha(\pi-\theta)} \right) \Big] \\ &- \alpha \left(\theta \mathrm{e}^{-\alpha\theta} + (\pi-\theta)\mathrm{e}^{-\alpha(\pi-\theta)} \right) \sum_{n=0}^{\infty} A_n,\end{aligned} \tag{2.40}$$

$$\mathbb{K}(\theta) = \sum_{n=0}^{\infty} A_n(4n^2-1)\cos 2n\theta + \sum_{n=0}^{\infty} A_n(\alpha^2-1)\left(\mathrm{e}^{-\alpha\theta} + \mathrm{e}^{-\alpha(\pi-\theta)} \right). \tag{2.41}$$

The $O(\delta^2)$ correction to the pressure produces terms comparable in size to the leading order damping terms in the bulk of the fluid, via $\omega^2\delta^2 = 2\gamma\omega\Omega$, and is therefore retained. The last term of $\mathbb{T}(\theta)$ is negligible if $\gamma \ll 1$, considering (2.33). Note however, that the boundary layer terms in the curvature term $\mathbb{K}(\theta)$ may be sizable due to the prefactor of α^2, in spite of (2.33).

If axial oscillations are again considered, it can be shown that the damping coefficient $\gamma_n = \gamma(2n+1)$ for the n^{th} azimuthal mode is modified in the presence of an oscillation of axial wavenumber m to

$$\gamma_n(m) = \gamma \frac{m}{2} \frac{\mathrm{K}_{2n-2}(m) + 2\mathrm{K}_{2n}(m) + \mathrm{K}_{2n+2}(m)}{\mathrm{K}_{2n-1}(m) + \mathrm{K}_{2n+1}(m)} \tag{2.42}$$

This reduces to γ_n as $m \to 0$, but bearing in mind that m is at least $2\pi a/D$, we find for our experimental parameters that even this lowest axial wave number leads to about five times larger damping as compared to $m = 0$. Therefore, axial oscillations not only induce fast-decaying flow fields, but the amplitude of these flow fields is, at equal excitation, much smaller to start with when compared to the purely azimuthal modes. This further justifies the 2D model and rationalizes the observed planar flow fields.

The corresponding 2D resonance frequencies $\Omega_n = \Omega\sqrt{2n(4n^2-1)}$ are modified to

$$\Omega_n(m) = \Omega \left\{ m(m^2+4n^2-1) \frac{\mathrm{K}_{2n-1}(m) + \mathrm{K}_{2n-1}(m)}{2\mathrm{K}_{2n}(m)} \right\}^{1/2}, \tag{2.43}$$

using a balance between pressure and surface tension that are directly computed from (2.27).

The radius dynamics are described by the component of (2.38) that is independent of θ, and

involves the forcing pressure p^* and the constant R_∞, which was introduced due to the planar flow assumption. They are however, irrelevant in the calculation of the surface mode amplitudes relative to the radial mode. Formally, we evaluate a Fourier cosine series of (2.38), and consider only those components that have explicit θ dependences. Rearranging the equations for the individual Fourier cosine components of (2.38), we have

$$A_n + g_n \sum_{k=0}^{\infty} A_k + h_n \sum_{k=0}^{\infty} (2k+1) A_k = 0; \tag{2.44}$$

for all positive integers n, where $g_n = \tilde{B}_n/\tilde{D}_n$ and $h_n = \tilde{C}_n/\tilde{D}_n$, with

$$\begin{aligned} \tilde{B}_n &= \frac{4\alpha(\alpha^2-1)}{\pi(\alpha^2+4n^2)}, \qquad \tilde{C}_n = -\frac{4\mathrm{i}\gamma\lambda\alpha}{\pi(\alpha^2+4n^2)}, \\ \tilde{D}_n &= -\frac{\lambda^2}{2n} + 4\mathrm{i}\lambda\gamma(2n+1) + (4n^2-1), \end{aligned} \tag{2.45}$$

$\lambda = \omega/\Omega$ being a dimensionless frequency. Mode coupling occurs purely through the boundary layer terms g_n and h_n in the corner regions where the bubble meets the walls. Without these terms, one recovers the 2D analogy of the surface mode dynamics for a spherical bubble in bulk fluid, which remain unexcited by a long wavelength forcing [75].

In order to determine the strength of the surface mode amplitudes relative to the volume mode, we solve (2.44) in conjunction with (2.33), for $A_{n\geq 1}$ in terms of A_0. Truncating the series at $n = N$, we obtain an overdetermined system of $N+1$ equations for the N unknowns A_1 through A_N.

$$A_n + g_n \sum_{k=0}^{N} A_k + h_n \sum_{k=0}^{N} (2k+1) A_k = 0, \tag{2.46a}$$

$$\sum_{n=0}^{N} A_n = 0\,. \tag{2.46b}$$

To accommodate the pinning condition (2.33), we first write $\sum_0^N A_n = K\delta^2$ with a constant $K = O(1)$, and verify that the results are not sensitive to the choice of K, including setting $K = 0$. (2.46) may be concisely written as $G_{in}A_n = A_0\, f_i$, where G_{in} encodes the N dynamical equations (2.46a) and the kinematic condition (2.46b), and f_i contains only terms of (2.46a) proportional to A_0. The Fourier mode amplitudes of the flow field A_n may now be solved for as scalar multiples of

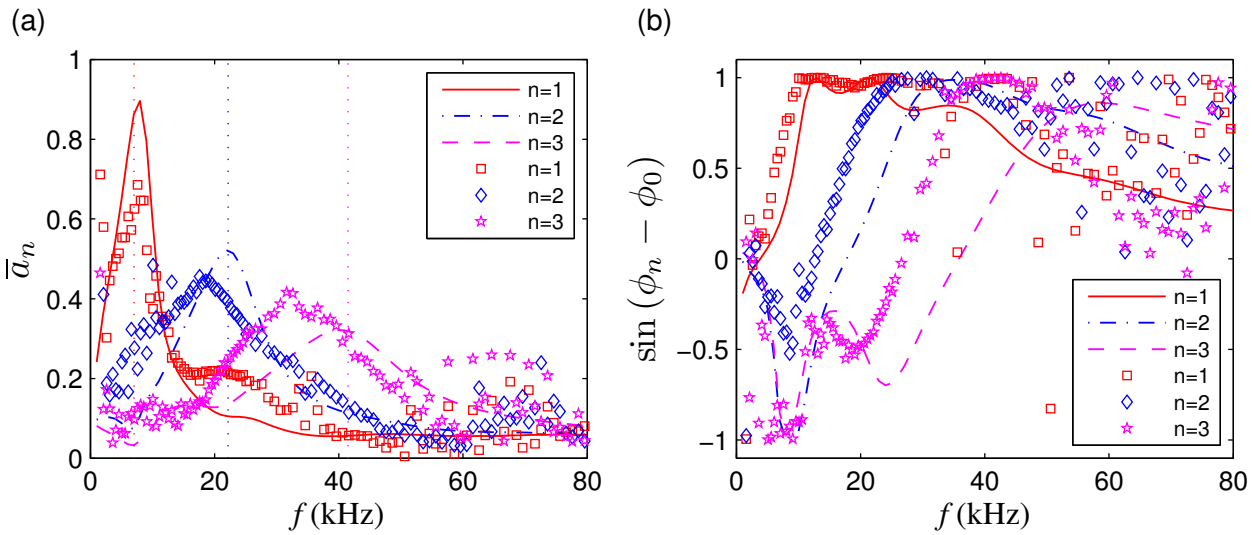

Figure 2.4 (a) Relative amplitudes $\bar{a}_n$ and (b) sine of relative phase angles $\phi_n - \phi_0$ of the first three even surface modes. The symbols correspond to experimentally measured values for a nearly hemicylindrical bubble, and the solid lines are predicted by the theory. Vertical lines indicate the undamped resonance frequencies of corresponding surface modes of free cylindrical bubbles in bulk.

A_0 by a least squares minimization of the norm of the residual $\|\boldsymbol{G.A} - A_0\boldsymbol{f}\|_2$.

Using these A_n, we decompose the bubble outline $\zeta(\theta)$ in (2.35) into its Fourier cosine components ζ_n, and obtain the surface mode shape amplitudes a_n and phases ϕ_n, as given in (2.1),

$$\zeta(\theta) = \sum_{n=0}^{N} \zeta_n \cos 2n\theta = \sum_{n=0}^{N} a_n \mathrm{e}^{\mathrm{i}\phi_n} \cos 2n\theta \,. \tag{2.47}$$

The relative amplitudes $\bar{a}_n = a_n/a_0$ and phases $\phi_n - \phi_0$ can now be compared to experiment (see figure 2.4(a) and figure 2.4(b)). The peaks of the relative amplitude curves occur near the resonance frequencies for the a bubble in free space $\Omega_n = \Omega\sqrt{2n(4n^2-1)}$. The main features of the amplitude and phase curves are reproduced consistently for each surface mode and are a consequence of the surface mode coupling to the volume mode as well as to each other. The widths of the amplitude curves are greater than expected from the damping coefficient γ alone – it must be noted here that the oscillator equation (2.38) contains indirect contributions to damping from the vortical boundary layer flow, leading to higher effective damping. Such contributions were previously noted for shape oscillations of spherical bubbles by Prosperetti [76] and in the context of sonoluminescing bubbles [27]. The shape of the curves is not very sensitive to the choice of truncation N, though larger N

leads to smaller residuals, i.e., better approximations of (2.33). The remaining discrepancies can be attributed to (i) the relatively large size of δ in experiment – expansions in this theory generally demand $n\delta \ll 1$, but for the frequencies in the range considered we have only $n\delta \lesssim 0.4$; (ii) neglected axial oscillations of the bubble may lead to shifts in the azimuthal resonance frequencies [93, 94] and minor components of 3D flow (these effects could become stronger for bubbles of larger axial extent D, as smaller axial wavenumbers become accessible); (iii) the results are rather sensitive to changes in bubble rest shape: While the theory is compared here to experimental data for bubbles very close to hemicylindrical shape, the resonances of slightly smaller (less than hemicylindrical) bubbles show improved agreement.

The theory provides the full oscillatory flow field at any frequency, which is required in the calculation of the steady streaming flow.

2.5 Effect of channel height on the oscillatory flow

We have so far assumed that the fluid is unbounded as $r \to \infty$. While this assumption is reasonable for the present experiments ($h \equiv H/a = 25 \gg 1$), it is desirable in several practical applications to have channel heights that are not much greater than the bubble radius [105, 112]. It has been shown theoretically by Doinikov and Bouakaz [15] that the presence of a rigid wall at a large but finite distance from a spherical bubble undergoing a combination of radial and translational oscillations may drive stronger streaming compared with that due to the same bubble in a fluid of infinite extent.

Here we consider the modification of the oscillatory flow field due to the introduction of a rigid-no slip wall at $y = h$, in the limit $h \gg 1$. The general discussion on the structure of the oscillatory flow field remains unchanged, except for the introduction of a second no slip boundary layer near $y = h$. In order to suitably develop a suitably valid oscillatory flow field valid for finite h, we start with the half-space oscillatory solution (2.28). Only potential flow solutions (algebraically decaying terms of equation 2.28) survive outside the bubble boundary layer, and are given to leading order in δ by

$$\psi_b^{outer} = \sum_{n=0}^{N} A_n \frac{1}{r^{2n}} \frac{\sin 2n\theta}{2n} \mathrm{e}^{\mathrm{i}t} + O(\delta). \tag{2.48}$$

The velocity due to a mode n of (2.48) decays in general as r^{-2n-1}. The half-space oscillatory solution therefore introduces normal velocities at $y = h$ of $O(h^{-1})$ due to the monopole ($n = 0$), while surface modes ($n > 0$) result only in h^{-3} normal velocity at $y = h$. To leading order in h^{-1} it is therefore sufficient to modify only the $n = 0$ term of (2.48) in order to satisfy the additional no-penetration condition at $y = h$. This is easily accomplished by the use of either a potential flow image system (point sources) or a Schwartz–Christoffel transformation, see e.g. [58]. In general, a modified version of (2.48), additionally satisfying the no-penetration condition at the opposite wall ($y = h$) up to $O(h^{-2})$ can be written as

$$\psi_b^{outer} = B_0 \,\mathrm{e}^{\mathrm{i}t}\,\mathrm{Im}\left\{\log\left(\sinh\frac{\pi w}{2h}\right)\right\} + \sum_{n=1}^{N} B_n \frac{1}{r^{2n}}\frac{\sin 2n\theta}{2n}\mathrm{e}^{\mathrm{i}t} + O(\delta) \tag{2.49}$$

$$= B_0\,\mathrm{Im}\left\{\log\left(\sinh\frac{\pi w}{2h}\right)\right\} - \sum_{n=1}^{N} B_n\,\mathrm{Im}\left\{\frac{w^{-2n}}{2n}\right\}\mathrm{e}^{\mathrm{i}t} + O(\delta), \tag{2.50}$$

where $w = x + \mathrm{i}y$ [58]. Note that in principle, the $n > 1$ contributions may also be written in terms of complex variables. The coefficients B_n are determined by kinematic conditions at the oscillating interface. For $\zeta(\theta) = \sum_{n=0}^{N} a_n \mathrm{e}^{\mathrm{i}\phi_n}$ (cf. (2.47)), the one finds to $O(\delta, h^{-4})$ that

$$B_n = \begin{cases} a_n \mathrm{e}^{\mathrm{i}\phi_n}, & n \neq 1, \\ a_n \mathrm{e}^{\mathrm{i}\phi_n} - \dfrac{\pi^2}{12h^2} a_0 \mathrm{e}^{\mathrm{i}\phi_n}, & n = 1. \end{cases} \tag{2.51}$$

Note that while the oscillatory flows corresponding to $n > 0$ have not been modified, the modification of the $n = 0$ solution by the opposite wall introduces a coupling between $n = 0$ and $n = 1$ modes through through the coefficients B_n.

We are now in a position to compute the bubble boundary layer terms, or equivalently write down a modified form of (2.24). In particular, the modification of the $n = 0$ solution due to the opposite wall results in additional $O(h^{-2})$ tangential velocity components at the bubble surface, resulting in additional bubble boundary layer terms. The boundary layer structure associated with $n > 1$ remains unchanged. Using an expansion of (2.49) in powers of h^{-1} one can show that the

flow field outside wall boundary layers is

$$\psi_b(r,\theta) = B_0 \mathrm{e}^{\mathrm{i}t}\left(\mathrm{Im}\left\{\log\left(\sinh\frac{\pi w}{2h}\right)\right\} + \frac{\pi^2}{12h^2} d_{-2}\mathrm{K}_2(\alpha r)\sin 2\theta\right) + \sum_{n=1}^{\infty} B_n\left(\frac{c_{2n}}{r^{2n}} - d_{2n}\mathrm{K}_{2n}(\alpha r)\right)\sin 2n\theta\, \mathrm{e}^{\mathrm{i}t} \tag{2.52}$$

This is the proper form of the oscillatory flow field for channels of finite height h, outside of the wall boundary layers at $y = 0$ and $y = h$. It should be remarked that the modification of the oscillatory flow field due to the introduction of the wall is reflected in the dynamic response of the interface itself, i.e. a_n and ϕ_n are non-trivial functions of h. This is evidenced by the experimental results of Wang [109]. The interface oscillation dynamics $a_n(h)$ and $\phi_n(h)$ for finite h, may in principle be recomputed using techniques similar to those used for $h \to \infty$ in this chapter, although we do not carry out this calculation here.

As a final remark on the effect of geometry on the primary flow, we note that the mean shape of the bubble (assumed here to have semicircular cross-section) may also affect the interfacial dynamics [80, 109]. It has been shown that for bubbles with slightly non-semicircular mean shapes in cross-section, coupling between volume and surface mode oscillations can occur without relying on the viscous wall boundary layer terms [80].

2.6 Conclusions

The present work advances research towards a quantitative description of microstreaming from a semi-cylindrical oscillating bubble attached to a wall, experimentally measuring as well as modeling the oscillation modes of the bubble interface, which are an indispensable input for the calculation of the mixed-mode streaming relevant in practical applications. It is shown that the relative amplitudes of azimuthal surface modes to the volume mode provide a robust measure and predictive characteristic of the flow structure and that the features of the associated resonance structures in frequency space can be explained by asymptotic theory. Axial modes are both more strongly damped and more strongly decaying with distance from the bubble, leading to a flow field that can be described as two-dimensional. As frequency increases and higher-order shape modes significantly contribute to the bubble oscillation, more intricate vortex structures develop close to the bubble.

The positions of the resonance peaks for the individual oscillation modes are well approximated by the expected resonance frequencies of free-bubble shape modes. However, the shape of the peaks (height and width) can only be understood through the coupling of different modes owing to the viscous effects in the boundary layers that govern the flow near the bubble interface and the wall. The relatively wide peaks help explain the robust flow field response obtained from bubbles in experiment, where an accurate fine-tuning of frequencies is generally unnecessary, and frequency drift does not compromise the flows. The flow field and dynamics are in general modified in channels of finite height.

Chapter 3

Two-dimensional streaming theory

In the previous chapter, we established that oscillations of the interface are effectively described by assuming linear oscillations of the interface. These oscillations drive a primary oscillatory flow, which is expressed analytically in the limit of a small oscillatory shear layer thickness. While the oscillatory flow itself is not of direct practical interest, it is directly responsible for driving steady secondary streaming flows – streaming. This chapter[1] will aim at developing a rigorous description of these steady flows, using a method of matched asymptotic expansions in the limit of small boundary layer thickness. We first develop a steaming theory that is valid in the half-space for an arbitrary two dimensional oscillations of the interface. We then consider in greater detail the specific problem at hand, viz. one where the interface oscillation shapes of the bubble are determined by the interfaces dynamics described in the previous chapter, allowing the streaming flow to be described entirely as a function of the driving frequency and damping parameter.

The theory shows that several oscillation modes can be involved in the generation of the typical streaming flow pattern and explains why the "fountain" is generically observed over a wide range of driving ultrasound frequencies. It also demonstrates that for large enough frequencies, the fountain flow is altered and eventually replaced by a vortex pattern of reversed orientation ("anti-fountain", figure 3.1*b*). These findings are in good agreement with experiment and constitute a complete derivation of sessile microbubble streaming flow with only the (dimensionless) driving frequency and a damping coefficient as input parameters. Lastly, we advance a semi-analytical formalism that allows the generalization of the half-space solution to a steaming flow within two-dimensional channels of arbitrary height.

[1] This chapter is adapted from Rallabandi et al. [77] and parts of Rallabandi et al. [78].

3.1 Introduction

Steady streaming is the name given to flow phenomena resulting from a time average over oscillatory fluid motion, arising in a variety of scientific and engineering applications, see e.g. Lighthill [39], Lutz et al. [51], Marmottant and Hilgenfeldt [55], Riley [86], Wang et al. [112]. We focus here on streaming induced by oscillatory boundary motion, a subject that has long been studied in the context of translational oscillations of objects and resulting transport phenomena [51, 81, 83]. Large oscillation amplitude is a desirable feature to ensure strong streaming flows (streaming flow speed being quadratically dependent on the amplitude), which has led to recent interest in streaming induced by the oscillation of bubbles [1, 55, 110]. While translational bubble oscillations (without volume change) lead to weak streaming [11, 47], the presence of volume oscillations causes much stronger flows that have been demonstrated as efficient tools for transport [111], shear force actuation [55], particle trapping and size sorting [73, 110], or micromixing [1, 112] applications. In practically relevant situations, ultrasound-driven bubbles are sessile at walls in microfluidic devices, and the generic streaming flow pattern consists of a vortex system above the bubble, expelling liquid upwards along the bubble's symmetry axis ("fountain" streaming flow, see figure 3.1*a*).

A systematic theoretical analysis of such sessile bubble streaming flows has, however, been missing. While some direct numerical simulations of specific cases exist [44], asymptotic theories [14, 45, 47, 56] have neglected one or several of the salient features that make the problem unique and different from other streaming situations: (i) the bubble oscillation occurs not in bulk, but the fluid is a half-space defined by the wall; (ii) the bubble is attached to the wall by contact lines; (iii) two different oscillatory boundary layers exist at the wall (no-slip) and around the bubble (no-stress); and (iv) the bubble's free surface is capable of oscillations in various modes. In this chapter, we derive a streaming solution taking into account all these factors.

3.2 2D Bubble Streaming Theory

We consider the steady flow induced by a harmonically oscillating semi-cylindrical bubble (of semi-circular cross-section) attached to a rigid wall via stationary contact lines as shown in figure 3.1*c*. The bubble has a rest radius a and its surface oscillates with angular frequency $\omega = 2\pi f$ and

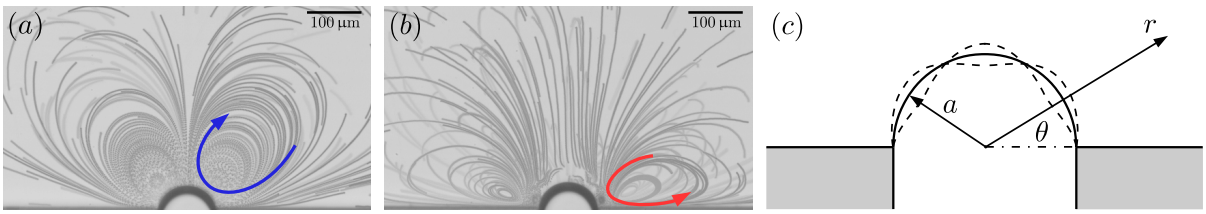

Figure 3.1 (a,b) Pathlines of the steady streaming around an oscillating bubble of radius $a = 40\,\mu\text{m}$ (bottom centre), visualized by neutrally buoyant tracer particles of 1 µm radius. Arrows indicate the orientation of the flow at (a) $f = 20$ kHz (fountain), and (b) $f = 84$ kHz (anti-fountain); (c) geometry of the problem showing the coordinate system. Dashed lines in (c) indicate the position of the interface at two instants of time.

characteristic amplitude ϵa, where $\epsilon \ll 1$, driving the fluid around it at the characteristic oscillatory velocity $U_0 = \epsilon a\omega$. As is typical of several microfluidics applications [1, 44, 55], oscillations of the interface in our experiments are set up by an externally applied acoustic field ($f \sim$ 1–100 kHz), whose wavelength ($\sim$ 1 cm–1 m) is much greater than the radius of the bubble ($a \approx 40\,\mu\text{m}$), and may therefore be considered as spatially uniform in practice.

We are interested primarily in the two-dimensional flow excited by such a bubble, which is both useful and accurate as an approximation in the context of flows in microfluidic devices [110, 111]. In particular, axial oscillations of the bubble are only weakly excited due to much stronger damping, and drive three dimensional flows which decay much more rapidly away from the bubble, so that the dominant oscillations of the interface are in the plane perpendicular to the bubble axis [112]. In our experiments, the bubble has an axial dimension $D = 100\,\mu\text{m} \approx 2.5a$, which is also the wavelength of the lowest permitted axial mode (cf. chapter 2). Since oscillation modes of small wavelengths are more strongly damped, axial modes are expected to become comparably excited only for larger values of D, as shown by Wang et al. [112].

In a polar coordinate system (r, θ) coaxial with the axis of the bubble, with the rigid walls to which the bubble is attached at $\theta = 0$ and $\theta = \pi$, the bubble surface is described in units of a as $R(\theta, t) = 1 - \mathrm{i}\epsilon\zeta(\theta)\mathrm{e}^{\mathrm{i}t}$, where $\zeta(\theta)$ is $O(1)$ and only the real part of any complex quantity is physically meaningful, cf (2.19). Using characteristic length, time and velocity scales a, ω^{-1} and U_0 respectively, we define a dimensionless stream function ψ, related to radial and azimuthal velocity components by $u = r^{-1}\partial_\theta\psi$ and $v = -\partial_r\psi$ respectively. The planar flow is governed by the

Navier–Stokes equations, which in 2D, is conveniently written in terms of the vorticity equation as

$$\frac{\partial \nabla^2 \psi}{\partial t} - \frac{\epsilon}{r}\frac{\partial(\psi, \nabla^2\psi)}{\partial(r,\theta)} = \frac{\delta^2}{2}\nabla^4\psi, \tag{3.1}$$

where

$$\frac{\partial(f,g)}{\partial(x,y)} \equiv \frac{\partial f}{\partial g}\frac{\partial g}{\partial y} - \frac{\partial f}{\partial y}\frac{\partial g}{\partial x}$$

denotes the Jacobian determinant. $\delta \equiv \sqrt{2\nu/(a^2\omega)}$ is the dimensionless oscillatory boundary layer thickness, assumed small compared to the radius of the bubble ($\delta \ll 1$), a condition practically realised in many microfluidics applications [e.g. 56, 73, 110]. Note that the vorticity vector is itself given by $\boldsymbol{\omega} = \nabla \times \boldsymbol{u} = -\nabla^2\psi\hat{\boldsymbol{z}}$. The motion of the interior gas will be neglected, as its density and dynamic viscosity are negligible compared with those of the exterior liquid.

As is standard practice in analytical treatments of streaming [47, 70, 84, 86], we develop an asymptotic solution in powers of ϵ : $\psi = \psi_0 + \epsilon\psi_1 + O(\epsilon^2)$. The leading order stream function ψ_0 is then governed by

$$\left(\frac{2}{\delta^2}\frac{\partial}{\partial t} - \nabla^2\right)\nabla^2\psi_0 = 0, \tag{3.2}$$

along with effective boundary conditions (kinematic and zero tangential stress) at the mean position of the interface

$$\left.\begin{aligned} &\frac{1}{r}\frac{\partial\psi_0}{\partial\theta} = \zeta \mathrm{e}^{\mathrm{i}t} \quad \text{on} \quad r = 1, \\ &\frac{\partial^2\psi_0}{\partial r^2} - \frac{1}{r}\frac{\partial\psi_0}{\partial r} - \frac{1}{r^2}\frac{\partial^2\psi_0}{\partial\theta^2} = 0 \quad \text{on} \quad r = 1, \end{aligned}\right\} \tag{3.3}$$

in addition to no-slip conditions at the walls,

$$\frac{\partial\psi_0}{\partial r} = \frac{1}{r}\frac{\partial\psi_0}{\partial\theta} = 0 \quad \text{on} \quad \theta = 0 \text{ and } \theta = \pi\,. \tag{3.4}$$

The oscillatory stream function ψ_0 has already been described in detail as a function of frequency in chapter 2 (where it has been called ψ).

In general, ψ_1 consists of both oscillatory and steady components, of which we are interested primarily in the latter, here denoted by the time average $\langle\psi_1\rangle$. This constitutes the Eulerian mean

flow and is governed by an inhomogeneous Stokes equation

$$\nabla^4\langle\psi_1\rangle = -\frac{2}{\delta^2}\left\langle \frac{1}{r}\frac{\partial(\psi_0, \nabla^2\psi_0)}{\partial(r,\theta)}\right\rangle, \tag{3.5}$$

provided that the streaming Reynolds number $Re_s \equiv 2\epsilon^2/\delta^2 \ll 1$, see e.g. [101]. In practice, the steady motion of individual fluid elements is of greater practical relevance, which is evaluated by augmenting the Eulerian stream function with a Stokes drift term ψ_d, defined as [81]

$$\psi_d = \left\langle \frac{1}{r}\frac{\partial\psi_0}{\partial\theta}\int -\frac{\partial\psi_0}{\partial r}\mathrm{d}t\right\rangle. \tag{3.6}$$

In analogy to the work of [47], but more generally, it can be shown (Appendix A) that for periodic interfacial motion with arbitrary $\zeta(\theta)$, a consistent expansion of the no-penetration and no-stress boundary conditions in ϵ yields particularly simple expressions for the first-order time-averaged terms when expressed in the Lagrangian stream function $\Psi = \langle\psi_1\rangle + \psi_d$. In particular, both radial velocity and tangential stress due to Ψ vanish at the mean position of the interface, i.e.,

$$\left.\begin{aligned} &\frac{1}{r}\frac{\partial\Psi}{\partial\theta} = 0 \quad \text{on} \quad r = 1, \\ &\frac{\partial^2\Psi}{\partial r^2} - \frac{1}{r}\frac{\partial\Psi}{\partial r} - \frac{1}{r^2}\frac{\partial^2\Psi}{\partial\theta^2} = 0 \quad \text{on} \quad r = 1, \end{aligned}\right\} \tag{3.7}$$

in addition to no-slip conditions at the walls, given by

$$\frac{\partial\Psi}{\partial r} = 0, \quad \text{on} \quad \theta = 0 \text{ and } \theta = \pi, \tag{3.8a}$$

$$\frac{1}{r}\frac{\partial\Psi}{\partial\theta} = 0, \quad \text{on} \quad \theta = 0 \text{ and } \theta = \pi\,. \tag{3.8b}$$

We note that in typical microfluidics applications, the presence of surfactants may in general modify the no-stress condition at the interface. However, a remobilization of the interface occurs if the concentration of surfactant exceeds its critical micelle concentration (CMC), and if the the rate of micellization is faster than the rate of convective transport along the interface [98, 115]. In our experiments, we use the polyexthoxylated (PEO) surfactant Tween 20 [98] at 1 % w/w in solution (far greater than its CMC). Additionally, the relaxation times of typical PEO surfactants ($\sim 100\,\mu$s) [6] are much shorter than characteristic time scales of mass transport along the interface by the

streaming flow (1–2 ms). This suggests that the surfactants do not retard the fluid motion near the interface, and a no-stress condition at the interface is indeed applicable. This is further validated by experimental measurements that indicate no drop in tangential velocity near the interface (e.g. figure 3.3 *c*), and also by additional experiments with oscillatory channel flow over bubbles that show flow patterns that differ greatly from those induced by oscillating cylinders [see e.g. 50].

3.3 General solutions to the Lagrangian mean flow

From the above, we see that the streaming flow follows as a second-order effect from the first-order oscillatory flow, which is in turn a function of the dynamics of the interface as a response to the driving frequency. While the system of equations (3.2) – (3.8) is not amenable to a general analytical solution for ψ_0 and ψ_1, an approximate solution using matched asymptotic expansions can be developed for $\delta \ll 1$.

We build here on our own previous results on the bubble interface dynamics (chapter 2, [112]) as well as on long-standing results on the streaming flow near a rigid no-slip wall [46, 70, 86]. For $\delta \ll 1$, Longuet-Higgins [46] showed that for an imposed oscillatory slip velocity $u_s(r)\mathrm{e}^{\mathrm{i}t}$, the steady Lagrangian slip velocity that persists at the outer edge of the wall boundary layer is given by

$$U_s = -\frac{3-5\mathrm{i}}{4} u_s^* \frac{\mathrm{d}u_s}{\mathrm{d}r}, \tag{3.9}$$

where u_s^* is the complex conjugate of u_s.

We now develop a formalism to evaluate the Lagrangian streaming *outside* the wall boundary layer, which must satisfy both the boundary conditions at the bubble (3.7) and support the steady slip velocity U_s at the wall, in order to match the steady wall boundary layer solution. As shown in chapter 2, the solution to the oscillatory flow problem (3.2) – (3.4), valid outside the wall boundary layer ($r\theta \gg \delta$) is, to leading order in δ,

$$\psi_{0b}(r,\theta) = \sum_{n=0}^{\infty} \psi_0^n(r,\theta) = \sum_{n=0}^{\infty} A_n \left(\frac{c_{2n}}{r^{2n}} + d_{2n} K_{2n}(\alpha r) \right) \sin 2n\theta \, \mathrm{e}^{\mathrm{i}t}, \tag{3.10}$$

where A_n is in general complex, $\alpha \equiv (1+\mathrm{i})/\delta$,

$$c_k = \frac{1}{k} - d_k K_k(\alpha), \text{ and } \quad d_k = -\frac{2(k+1)}{\alpha^2 K_{k-2}(\alpha) + 2k\alpha K_{k-1}(\alpha)}\,. \tag{3.11}$$

The oscillatory slip velocity at the edge of the wall boundary layer is then

$$u_s(r) = \sum_{n=0}^{\infty} \frac{A_n}{r^{2n+1}} + O(\delta^2), \tag{3.12}$$

and ultimately determines the steady slip velocity U_s via (3.9).

Since ψ_{0b} represents the oscillatory flow outside the wall boundary layer, it may be used in place of the full oscillatory stream function ψ_0 in (3.5) and (3.6) to obtain the Lagrangian mean flow function in this region. Taking Ψ to henceforth denote the Lagrangian mean stream function *outside* the wall boundary layer, (3.8b) is replaced to leading order by the slip condition

$$\frac{1}{r}\frac{\partial \Psi}{\partial \theta} = U_s \quad \text{on} \quad \theta = 0 \text{ and } \theta = \pi\,, \tag{3.13}$$

to properly match the steady Lagrangian wall boundary layer solution, while retaining the boundary conditions (3.7) and (3.8a). The flow resulting from Ψ can be directly compared with experimental trajectory data from passive tracer particles.

The analysis is aided by the explicit decomposition of $\langle\psi_1\rangle$ into a homogeneous solution ψ_{hom} and a particular solution ψ_p. As a general feature of streaming flows with $\delta \ll 1$, the particular solution of (3.5) decays exponentially over a scale of δ away from the boundaries of the domain [46]. Specifically, while the particular solution of (3.5) with (3.10) can be written in closed form using classical techniques [see e.g. 81], it is more appropriate to retain the asymptotic behaviour of ψ_p only, in order to remain consistent with the boundary layer treatment of the flow. To determine ψ_p outside the wall boundary layer, both (3.5) and (3.10) are expanded in powers of δ, using a bubble boundary layer coordinate $\eta \equiv (r-1)/\delta$. This yields a linear fourth order ordinary differential equation which is solved for $\psi_p(\eta)$. On the other hand, the Stokes drift (3.6) evaluated with (3.10) exhibits slower algebraic decay that persists in the bulk of the fluid, in addition to exponentially decaying terms. Note also that in the evaluation of time averages of products of oscillatory quantities in (3.5) and

(3.6), we use the identity $\left\langle \mathrm{Re}(p\,\mathrm{e}^{\mathrm{i}t})\,\mathrm{Re}(q\,\mathrm{e}^{\mathrm{i}t})\right\rangle = \frac{1}{2}\mathrm{Re}(p\,q^*)$, valid for any complex time-independent quantities p and q. We provide the details of this computation appendix B.

Using equations (14), (15) and (25) of the analysis of Wang et al. [112], it can be shown that the coefficients A_n are to $O(\delta^3)$ equal to the Fourier cosine coefficients $\zeta_n = a_n \mathrm{e}^{\mathrm{i}\phi_n}$ of the interface deformation $\zeta(\theta)$, where a_n is a positive mode amplitude and ϕ_n is a real phase angle. Note that in [112] these amplitudes and phases were derived directly from the physical parameters of the bubble oscillator (ω, a, ν) and can be taken as inputs for the calculation below. In the following, we will normalize the a_n by the volume mode amplitude a_0, defining $\bar{a}_n \equiv a_n/a_0$, and use relative phase angles $\phi_{m,n} \equiv \phi_m - \phi_n$. In order to determine the streaming flow pattern, we set $a_0 = 1$ without loss of generality, as it can be absorbed in the amplitude scale ϵ.

While the individual expressions for ψ_p and ψ_d are rather involved (cf. appendix B), their combined contribution to the flow field is simpler, and is more favourably written by the rearrangement $\psi_p + \psi_d = \Psi^+ + \Psi^-$, where

$$\Psi^{\pm} = \sum_{m>n}^{\infty}\sum_{n=0}^{\infty} \Psi^{\pm}_{m,n} \sin 2(m \pm n)\theta\,, \quad \text{with} \tag{3.14}$$

$$\left.\begin{aligned} \Psi^{+}_{m,n} &= \frac{\overline{a}_m \overline{a}_n}{1+\delta_{mn}} 2\delta^2\,(2m+1)(2n+1)\cos\phi_{m,n}\,\mathrm{e}^{-(1+\mathrm{i})\eta} \quad \text{and} \\ \Psi^{-}_{m,n} &= \overline{a}_m \overline{a}_n \left\{ \frac{1}{2r^{2(m+n+1)}} + 2\mathrm{i}\,\delta^2 (2m+1)(2n+1)\,\mathrm{e}^{-(1+\mathrm{i})\eta} \right\} \sin\phi_{m,n}\,, \end{aligned}\right\} \tag{3.15}$$

so that the Lagrangian stream function is given by $\Psi = \psi_{hom} + \Psi^+ + \Psi^-$. Note that algebraically decaying terms in (3.15) are due entirely to the Stokes drift and appear only in Ψ^-.

The homogeneous Stokes solutions ψ_{hom} must be chosen so that the Lagrangian stream function Ψ satisfies the boundary conditions (3.7) and provides the steady slip U_s at the edge of the wall boundary layer. We also note that the $O(\delta^2)$ boundary layer terms in (3.15) do not contribute to the velocity field at leading order, but can in general make a leading-order contribution to the tangential stress at the bubble. However, we find that to this leading order, the real part of the tangential stress at the interface due to Ψ^+ vanishes identically, which allows us to neglect Ψ^+ altogether in further calculations. Ψ^- thus carries the sum total of contributions to the streaming that arise directly from the specific oscillations of the bubble itself, independent of the presence of

the wall. It is also worth noting that all Ψ^- terms arise from the coupling of *distinct* oscillation modes (*mixed-mode streaming*), rather than from interaction of a mode with itself.

The slip condition at the edge of the wall boundary layer, evaluated using (3.9) and (3.12), is accommodated by expressing ψ_{hom} as a sum of elementary Stokes solutions that are either no-slip solutions (zero velocity at the wall) or slip solutions (zero normal velocity at the wall). The Lagrangian stream function then takes the form

$$\begin{aligned}\Psi &= \sum_{k=1}^{\infty} \frac{e_k}{r^{2k-1}} \left\{ \cos(2k-1)\theta - \cos(2k+1)\theta \right\} \\ &\quad + \sum_{k=1}^{\infty} \frac{f_k}{r^{2k}} \left\{ \frac{1}{2k} \sin 2k\theta - \frac{1}{2(k+1)} \sin 2(k+1)\theta \right\} + \psi_s + \Psi^-, \end{aligned} \tag{3.16}$$

where e_k and f_k are coefficients of two series of no-slip Stokes solutions, and ψ_s represents homogeneous slip solutions of (3.5). The slip condition on the Lagrangian mean flow (3.13) is then simply a condition on ψ_s, written explicitly in terms of normalized mode amplitudes and relative phase angles between modes as

$$\frac{1}{r}\frac{\partial \psi_s}{\partial \theta} = \sum_{m \geq n}^{\infty} \sum_{n=0}^{\infty} \frac{\overline{a}_m \overline{a}_n}{r^{2m+2n+3}} \frac{3}{2} \left\{ \frac{(m+n+1)\cos\phi_{m,n}}{1+\delta_{mn}} + (m-n)\sin\phi_{m,n} \right\} \quad \text{on} \quad \theta = 0 \text{ and } \theta = \pi. \tag{3.17}$$

Since ψ_s may be any fundamental slip solution of (3.5) that satisfies (3.17), we choose it to be a harmonic function without loss of generality, to obtain

$$\psi_s = \sum_{m \geq n}^{\infty} \sum_{n=0}^{\infty} \frac{\overline{a}_m \overline{a}_n}{r^{2(m+n+1)}} \frac{3}{4} \left\{ \frac{\cos\phi_{m,n}}{1+\delta_{mn}} + \frac{(m-n)\sin\phi_{m,n}}{m+n+1} \right\} \sin 2(m+n+1)\theta. \tag{3.18}$$

With this definition of ψ_s, the Lagrangian stream function Ψ defined by (3.16) spans the entire family of solutions satisfying (3.13). The boundary conditions (3.7) at the surface of the bubble, applied to the Lagrangian steady stream function in (3.16), lead to two equations valid for $0 < \theta < \pi$, which when written in an orthogonal Fourier basis, yield a system of linear algebraic equations in

e_k and f_k,

$$\left.\begin{aligned} f_k - f_{k-1} - \frac{128}{\pi}\sum_{j=1}^{\infty} \frac{jk^2\, e_j}{16j^4+16k^4-32j^2k^2-8j^2-8k^2+1} &= g_k, \\ (k+1)f_k - (k-1)f_{k-1} - \frac{32}{\pi}\sum_{j=1}^{\infty} \frac{jk(2j+1)(2j-1)\, e_j}{16j^4+16k^4-32j^2k^2-8j^2-8k^2+1} &= \frac{h_k}{2}, \end{aligned}\right\} \tag{3.19}$$

valid for all positive integers k, where it is understood that e_k and f_k are identically zero for $k \leq 0$. g_k and h_k are the negatives of Fourier sine and cosine components respectively of the contribution of $\hat{\psi} \equiv \psi_s + \Psi^-$ to normal velocity and tangential stress, defined as

$$\left.\begin{aligned} g_k &\equiv -\frac{2}{\pi}\int_0^{\pi} \frac{1}{r}\frac{\partial \hat{\psi}}{\partial \theta} \cos 2k\theta \,\mathrm{d}\theta \quad \text{on} \quad r=1, \\ h_k &\equiv -\frac{2}{\pi}\int_0^{\pi} \left(\frac{\partial^2 \hat{\psi}}{\partial r^2} - \frac{1}{r}\frac{\partial \hat{\psi}}{\partial r}\right) \sin 2k\theta \,\mathrm{d}\theta \quad \text{on} \quad r=1, \end{aligned}\right\} \tag{3.20}$$

terms of $O(\delta)$ and higher being neglected in both g_k and h_k. Note that definitions for g_k and h_k follow directly from (3.7), with the simplification that the no-penetration condition allows us to drop the azimuthal derivatives in the expression for the tangential stress at the interface. The linear system (3.19) after some manipulation yields analytical expressions for e_k and f_k:

$$\left.\begin{aligned} f_k &= \frac{1}{4}\Big((k+1)h_k - k\,h_{k+1}\Big) - \frac{1}{2}\Big((k+1)(k-1)g_k - k(k+2)g_{k+1}\Big), \\ e_k &= \frac{4}{\pi}\sum_{j=1}^{k}\sum_{i=1}^{\infty} \frac{f_i - f_{i-1} - g_i}{(2j+2i-1)(2j-2i-1)}\,. \end{aligned}\right\} \tag{3.21}$$

The normalized amplitudes $\overline{a}_n$ and relative phases $\phi_{m,n}$ may either be extracted directly from shape oscillations of the bubble, or via a theoretical calculation of the dynamics of bubble oscillation [112], which enables the evaluation of the Lagrangian mean flow up to the scaling factor ϵ^2 (determined experimentally by the amplitude of the driving ultrasound). The bubble dynamics itself is a function of two dimensionless parameters: the driving frequency normalized by the frequency scale governing surface mode excitation (λ), and a viscous damping constant (γ), defined as $\lambda \equiv \omega(\rho a^3/\Gamma)^{1/2}$ and $\gamma \equiv \lambda\delta^2/2$. Here, Γ is the surface tension and ρ is the density of the liquid, cf. chapter 2. In practically relevant situations, the damping is small ($\gamma \ll 1$).

We remark that the solutions (3.21) are in principle applicable to forced 2D Stokes flows in a

half-space with arbitrary kinematic and stress conditions at $r = 1$, and slip conditions at $y = 0$ being accommodated by the choice of $\hat{\psi}$. These solutions are used in subsequent sections of the chapter to construct the 2D streaming flow in fluid additionally bounded by a no-slip wall at $y = h$.

3.4 Results and Discussion

We evaluate the steady streaming using mode amplitudes and phases both from experimental measurements and dynamical calculations, which are in good agreement with each other. In practice, the infinite sums in (3.14)–(3.16) can be truncated at a finite N to good accuracy; for the theoretical results reported here, we take $N = 3$, which is also the number of surface modes that have been identified quantitatively in experiment. While higher modes may be excited in experiment, their amplitudes are smaller due to stronger damping and play a negligible role in determining the shape of the interface; we will justify this more precisely in the next paragraph. We find that the steady flow pattern is characterized by closed vortical flow lines. Over a wide range of frequencies and damping parameters, the velocity field in the bulk of the fluid is inward close to the wall, and radially outwards near the pole of the bubble in a "*fountain*" vortex pair, precisely the generically observed flow pattern of bubble microstreaming devices, see figures 3.1(a) and 3.2(a,b). A tiny secondary vortex pair near the pole of the bubble is also typically predicted and observed in experiment (figure 3.2a,b).

A quantitative comparison between experiment and theory in terms of non-dimensional variables requires the determination of the value of ϵ in experiment, which is identified with the amplitude a_0 of volume oscillations and sets the velocity scale in the system. Over a cycle of its oscillation, the interface sweeps a range of radial coordinates $R(\theta, t)$ as defined in (2.19), over an interval of size $\Delta R(\theta)$, cf. the dashed lines in figure 3.1(c). From experimental images, we determine the maximal value ΔR_m of $\Delta R(\theta)$. The theory of chapter 2 predicts the normalized mode amplitudes $\overline{a}_n$ and relative phases $\phi_{n,0}$, and therefore also predicts the ratio $\Delta R_m/(2\epsilon)$. Due to the dominance of the monopole amplitude (ϵ) over surface mode amplitudes, this numerical factor is of $O(1)$ over the entire range of frequencies of interest. Furthermore, the precise value of the ratio $\Delta R_m/(2\epsilon)$ depends only very weakly on the number of modes N taken into account as long as $N \geq 3$, and agrees well with the value obtained by using experimentally measured amplitudes and phases. This

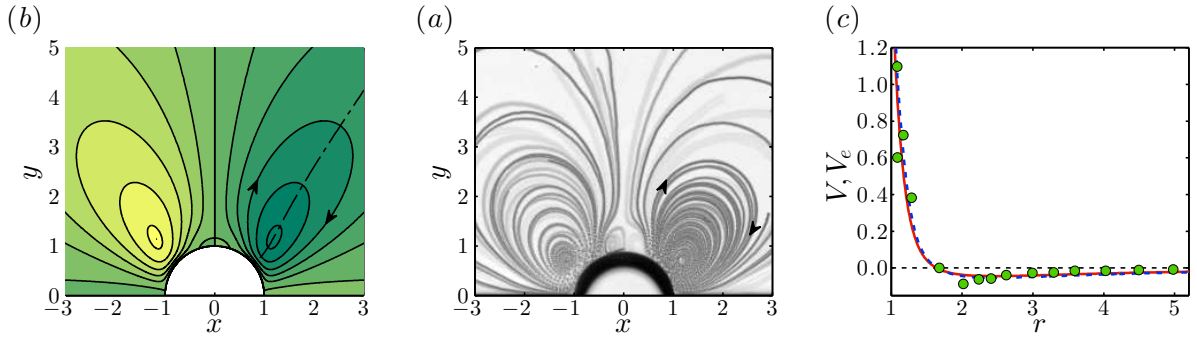

Figure 3.2 Comparison of fountain flows in experiment and theory. (a) Experimental streamlines of Lagrangian steady flow at $f = 26.7$ kHz; (b) computed streaming pattern at the corresponding dimensionless frequency $\lambda = 9.32$, using amplitudes and phases from the analysis of Wang et al. [112]. The agreement is representative of the entire regime of fountain flow patterns. (c) Steady Lagrangian azimuthal velocity v along lines of zero radial velocity (indicated as dot-dashed line in b), as a function of radial distance r: direct measurements from an experimental run at $f = 26.7\,\text{kHz}$ ($\circ$), computed from bubble oscillation amplitudes obtained from interface tracking experiments [112] of a different run at the same f (– –), and computed from theoretical bubble oscillation amplitudes using only $\lambda = 9.32$ as input (——).

determines ϵ and therefore the interface shape $R(\theta, t)$ to good accuracy using the experimental images, and is further justification for the truncation at $N = 3$.

In order to compare not just the flow patterns, but the observed velocities, we evaluate the azimuthal velocity along a line through the points of zero radial velocity in one of the vortices (figure 3.2b). From experimental movies, we determine the monopole amplitude ϵ using the method detailed in the previous paragraph (for figure 3.2c, $\epsilon \approx 0.025$, with a difference of 2.5% if we take $N = 10$). The azimuthal velocity is then scaled to the streaming velocity scale $U_1 = \epsilon U_0$ to yield V_e. We compare with theoretical calculations of the Lagrangian azimuthal velocity $V = -\partial_r \Psi$ for (i) velocities computed from experimentally measured a_n and $\phi_{m,n}$ values (dashed line in figure 3.2c) and (ii) velocities computed without experimental input directly from the experimental values of λ and γ (solid line). The agreement is very good, and we emphasize that neither the theoretical calculations nor the experimental streaming measurements involve any adjustable parameters. The radial distance of the vortex centre (the zero of the curve in figure 3.2c) is also accurately reproduced, an important quantity for experimental design of vortex traps [51], size sorters [110, 111], or micromixers [112]. The theory also gives insight into the observed reversal of vortex orientation at high frequency (figure 3.1b). At low frequency, it predicts a weak counter-rotating "*anti-fountain*" vortex pair very close to the wall (figure 3.3a), in order to support the outward slip velocity U_s.

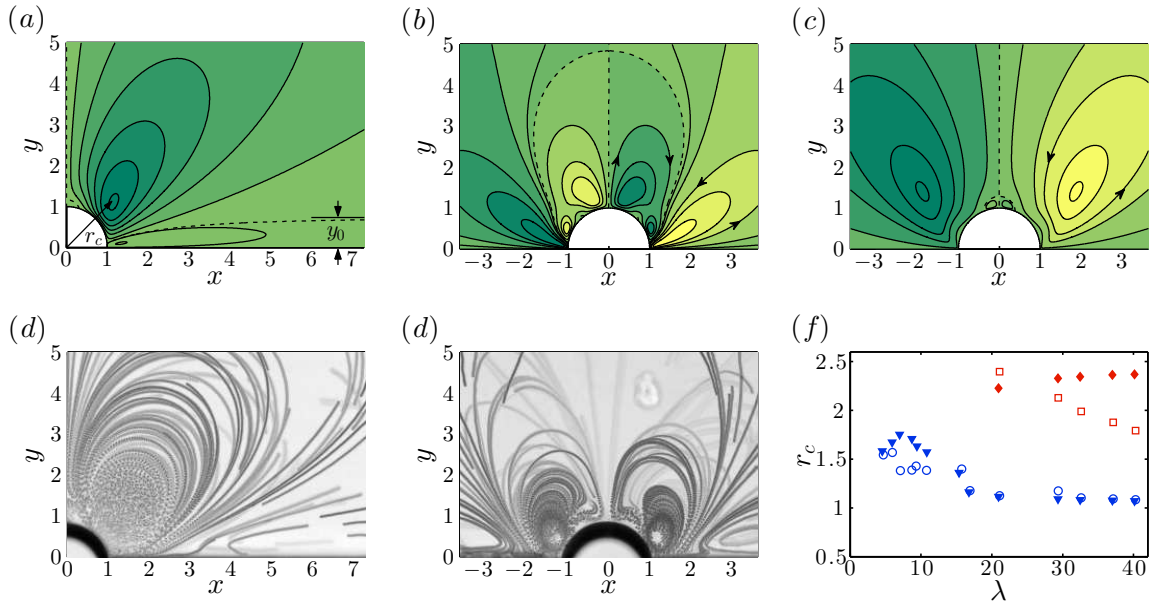

Figure 3.3 Streamlines of Lagrangian steady flow at (a) $\lambda = 11.3$, (b) $\lambda = 15.4$ and (c) $\lambda = 29.3$ indicating the orientation of flow (arrows) and the separatrices between counter rotating vortical systems (dashed lines); Experimental streakline images at (d) $\lambda = 11.3$ and (e) $\lambda = 16.9$ visualized using tracers of 1 μm radius; and (f) radial location of vortex centres (▼, ∘ : fountains; ♦, □: anti-fountains) as a function of dimensionless driving frequency. Filled and open symbols in (f) represent theoretically computed and experimentally measured positions, respectively. The experimental streakline image corresponding to (c) has been presented in figure 3.1*b*.

As the driving frequency is increased, this near-wall anti-fountain pair grows in size (figure 3.3*b*) and eventually (for $\lambda \gtrsim 15$) dominates the entire bulk, confining the fountain vortex pair to small structures near the bubble interface (figure 3.3*c*). A comparison with experiment at corresponding low (figure 3.3*d*), intermediate (figure 3.3*e*) and high driving frequency (figure 3.1*b*) shows that the salient features of the flowlines are captured. Figure 3.3*f* shows, in addition, that the experimental location of the fountain vortex centre is explained by the theory in very good quantitative agreement throughout the entire range of frequencies, while the position of the anti-fountain vortex centre is in fair agreement. Anti-fountain positions are only given for a range of λ where the theory gives unambiguous predictions, i.e., beyond the intermediate-frequency transition range, in which results are strongly dependent on higher-order mode details. It should be emphasized, though, that none of the theory predictions relies on any adjustment of free parameters.

This frequency dependent flow reversal is understood from the far-field behavior of the stream

function. The radially most slowly decaying parts of Ψ take the form

$$\Psi = \frac{3}{8r^2}\left(1 + \frac{16}{3}e_1 r\sin\theta + \frac{8}{3}f_1\sin^2\theta\right)\sin 2\theta + O(r^{-3}), \tag{3.22}$$

so that the sign of the coefficient e_1 indicates the orientation of the streaming in the bulk, and the far-field velocities decay as r^{-2}. Figure 3.4(a) shows the dependence of e_1 on λ and the agreement of its sign change with the flow reversal: at low frequencies, $e_1 < 0$ and fountain streaming dominates the bulk of the flow. The frequency of flow reversal depends only weakly on the damping coefficient γ. To describe the transition more quantitatively, we obtain the location of the separatrix between the two counter-rotating vortical systems by evaluating the stream function (3.22) to zero. Close to the wall in the far-field ($\sin\theta \to 0, r \to \infty$), the vertical height of the separatrix asymptotes to a constant $y_0 \equiv -3/(16e_1)$, indicated in figure 3.3a. For $e_1 < 0$, the anti-fountains are thus confined to a narrow strip ($0 < y < y_0$) above the wall, where the stream function assumes the form

$$\Psi \sim \frac{3y}{4r^3}\left(1 - \frac{y}{y_0}\right). \tag{3.23}$$

Thus, the radial velocity in this region decays more rapidly (r^{-3}) than the velocity in the bulk, explaining the very weak flow observed here. The radial velocity on the separatrix itself is the negative of the slip velocity U_s at the edge of the wall boundary layer. We will show in section 3.5 that in most practical situations, this weak antifountain structure is further suppressed due to the wall boundary layer, and vanishes entirely above a critical boundary layer thickness.

As the driving frequency is increased, the near-wall anti-fountains grow in azimuthal extent, and as e_1 becomes positive, the fountain vortices are confined to a finite region near the polar axis of the bubble (cf. figure 3.3b). The separatrix shape can again be understood by setting (3.22) to zero, but now for $\theta = \pi/2$, yielding a positive intersection with the z-axis, as our calculations show that $f_1 < 0$ for all λ where $e_1 \geq 0$. The fountains ultimately diminish to very small structures at high frequency (figure 3.3c). At the transition point between the fountain and the anti-fountain regimes where $e_1 = 0$, the far-field becomes dominated by the stronger-decaying velocity components (r^{-3}), as per (3.22). In addition to being weaker, the flow is characterized by two systems of closed streamlines per quadrant, easily understood by the azimuthal dependence of (3.22), setting e_1 to

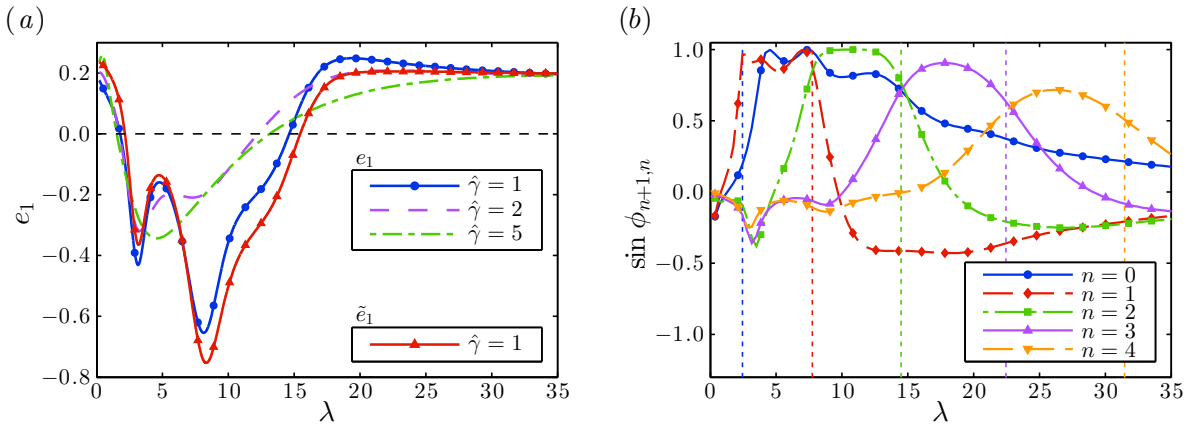

Figure 3.4 (*a*) Coefficient of the most slowly decaying Stokes solution e_1, vs. the dimensionless driving frequency λ, for different values of the reduced damping parameter $\hat{\gamma} \equiv \gamma/\gamma_0$, where $\gamma_0 \approx 0.0381$ is the damping constant in the experiments. (*b*) Sine of the relative phase angle $\phi_{n+1,n}$ for various n at $\hat{\gamma} = 1$, indicating a significant contribution in (3.24) primarily between the inviscid surface mode bulk resonance frequencies $\lambda_n = \sqrt{2n(4n^2-1)}$ and λ_{n+1} (vertical dashed lines, see chapter 2 or [112] for details of the bubble oscillation dynamics).

zero. The weakening of the flow near the transition frequency is also present in experiment, where a reduction in the extent of closed stable orbits of tracer particles is observed.

In order to understand the relationship of the far-field streaming with the oscillation modes of the bubble, we first recognize that the no-slip Stokes solution with the slowest radial decay also exhibits the most gradual *azimuthal* variation. Since the coefficients of the no-slip solutions (e_k and f_k) are ultimately determined by the boundary conditions at the bubble, the far-field no-slip solution depends most strongly on the lowest azimuthal Fourier component of $\hat{\psi}$, i.e., $\sin 2\theta$. This amounts to retaining only g_1 and h_1 in (3.21), yielding an approximation to e_1,

$$e_1 \approx \tilde{e}_1 = \frac{3}{5\pi}\left(1 - \frac{4}{9}\sum_{n=0}^{N-1} \overline{a}_n \overline{a}_{n+1}(4n+1)(4n+5)\sin\phi_{n+1,n}\right), \tag{3.24}$$

which agrees very closely with the full expression, see figure 3.4*a*. The term of (3.24) independent of $\overline{a}_n$ originates from the outward slip along the wall and is driven by volume oscillations of the bubble. In addition to this "wall-streaming" effect, the far-field flow depends directly on the coupling between pairs of *neighbouring* oscillation modes n and $n+1$, whose sign is determined by the sine of the relative phase difference $\phi_{n+1,n}$. For realistic cases of small damping ($\gamma \ll 1$), we find from the frequency response of the bubble [112] that for any $n \geq 1$ the phase factor $\sin\phi_{n+1,n}$ is of

significant size only over a range $\lambda_n \lesssim \lambda \lesssim \lambda_{n+1}$, i.e., between the resonance frequencies of the modes in question (figure 3.4*b*). Furthermore, within this range the quantity $\sin\phi_{n+1,n}$ is positive, resulting by (3.24) in a negative contribution to e_1. While higher order surface modes typically have smaller amplitudes (cf. the analysis of [112]), the n-dependence in (3.24) ensures that the mixed-mode contribution to e_1 overcomes the wall-streaming contribution for a large range of λ, resulting in $e_1 < 0$ and hence fountain streaming. Equation (3.24) emphasizes the dominance of *mixed-mode* streaming for sessile microbubbles. We note that while different mixed-mode pairs are dominant at different frequencies, the transitions between mode pairs are smooth and do not show marked changes in the appearance of the flow.

The dominance of coupling between neighbouring modes is understood from general considerations of the oscillation dynamics of the bubble. Every surface mode n, driven by volume oscillations of the bubble, exhibits similar amplitude and phase behaviour when driven far from resonance. There is therefore a band of frequencies (of width proportional to γ) around the resonance frequency λ_n, characterized by strong excitation of amplitude $\overline{a}_n$ and significant phase differences with other modes $\phi_{m,n}$. For neighbouring mode-pairs $(n, n+1)$, whose resonance frequencies are relatively close together, an overlap of the individual excitation regions results in a range of frequencies *between* these modes $\lambda_n \lesssim \lambda \lesssim \lambda_{n+1}$ where the amplitudes $\overline{a}_n$, $\overline{a}_{n+1}$ and phase difference $\phi_{n+1,n}$ are substantial. On the other hand, two modes whose resonance frequencies differ greatly will not simultaneously have significant amplitudes, ensuring that non-neighbour mode coupling is only a weaker secondary effect.

This mixed-mode streaming is eventually suppressed at high frequencies, where the mode amplitudes are considerably damped and the phase difference of neighbouring modes is smaller (also note the steady decline of $\sin\phi_{1,0}$ in figure 3.4). In this limit, the outward slip along the wall takes over as the dominant mechanism for streaming, with $e_1 \to 3/(5\pi)$ and (3.16) simplifying to the analytical expression

$$\Psi = \mathrm{Im}\left\{\frac{3(w-w^*)}{8\pi\, w^3}\left[\pi + \mathrm{i}w^3\left\{2\left(w^2+\frac{1}{w^2}\right)+\left(w^3+\frac{1}{w^3}\right)\ln\frac{w-1}{w+1}\right\}\right]\right\}, \tag{3.25}$$

where $w = r\exp\mathrm{i}\theta$ is a complex variable.

In this wall-dominated high frequency regime, we find in both theory and experiment that the

long axis of the vortex structures appears to point towards the "corners" where the bubble meets the wall, rather than towards the origin (cf. figure 3.3c). In experiments, however, we find that the vortex centres are located closer to the wall than is predicted by the theory (cf. also the deviations in figure 3.3f at high λ), which may be attributed to out-of-plane streaming flows driven by the walls parallel to the field of view confining the experimental set-up. The influence of these walls is expected to be significant in the large-λ limit, where wall streaming dominates.

It is worth remarking that the slip-driven component of the streaming flow depends primarily on the monopole amplitude and remains essentially constant over the frequency range of interest, in the normalization employed here ($a_0 = 1$); this corresponds to the term in (3.24) independent of $\overline{a}_n$. While the streaming speed measured in experiments can be quite sensitive to the geometry and materials of the experimental setup [112], the present approach shows that the mixed-mode streaming contribution to the flow *relative* to this wall-streaming component diminishes at higher frequency, with the dimensionless velocity in the far-field being proportional to e_1. Our theory therefore provides a consistent description of the steady flow field under the appropriate normalization, independent of the details of the setup.

3.5 Effect of wall boundary layer terms

We have thus far only considered the "outer" solution, strictly valid outside the wall boundary layer. Equation (3.15) shows that the bubble boundary layer terms are $O(\delta^2)$ in stream function, and therefore velocity contributions are at most $O(\delta)$. This is not however the case within the steady wall boundary layer, which accommodates both the slip U_s of the outer Lagrangian streaming, as well as the no-slip condition at $y = 0$. The rationale for this argument is that the outer flow consists of flow features on scales much greater than the boundary layer thickness δ.

While this is a good approximation for the majority of the outer flow, certain regions of the outer flow do in fact exhibit features on length scales much smaller than a bubble radius. In particular, we have already shown that while $e_1 < 0$ results in vortices with a fountain orientation in the bulk, these are accompanied by secondary anti-fountains near the walls of characteristic size $y_0 = -3/(16e_1)$ in the far-field, cf. figure 3.3(a). If y_0 becomes comparable to δ, one may expect a non-trivial interaction of secondary anti-fountains with the wall-boundary layer structure.

In order to probe this interaction, we now consider in detail the shape of the leading order Lagrangian wall boundary layer solution, which is given in general by Longuet-Higgins [46] as

$$\Psi_w = \left(-(1-\mathrm{i})\delta \mathrm{e}^{-(1-\mathrm{i})r\xi} - \frac{3}{8}(1+\mathrm{i})\delta \mathrm{e}^{-2r\xi} + \frac{\delta}{8}(11-5\mathrm{i}) - (3-5\mathrm{i})\frac{\delta}{4} r\xi \right) u_s \frac{\mathrm{d}u_s^*}{\mathrm{d}r} + c_1(r)\delta^2\xi^2 + c_2(r)\delta^3\xi^3, \tag{3.26}$$

where $\xi = \theta/\delta$ (cf. chapter 2), and $c_1(r)$ and $c_2(r)$ are determined by asymptotic matching. Here, they are determined by the form of the outer solution as $\theta \to 0$. In particular, in the far-field (see (3.22)), the outer solution near $\theta = 0$ has the asymptotic form

$$\Psi(r \to 0, \theta \to 0) = \frac{3}{8r^2}\left(1 + \frac{32}{3}e_1 r\theta^2 + \frac{16}{3}f_1\theta^3\right) + O(\theta^4), \tag{3.27}$$

which determines that

$$c_1(r) = \frac{4e_1}{r} \quad \text{and} \quad c_2(r) = \frac{2f_1}{r^2}. \tag{3.28}$$

In the limit $r \to \infty$ the wall boundary layer solution at $\theta \sim 0$ may therefore be written as

$$\Psi_w = U_s\delta\left(\frac{4}{3}(1-\mathrm{i})\mathrm{e}^{-(1-\mathrm{i})\eta_w} + \frac{1}{2}\mathrm{e}^{-2\eta_w} - \frac{11}{6} + \eta_w - \eta_w^2\beta\right), \tag{3.29}$$

where $U_s = 3/4r^3$, and $\eta_w \equiv y/\delta$ is a wall-normal boundary layer coordinate, and is equivalent to $r\xi$ to the order of δ employed in the boundary layer approximation. The quantity $\beta \equiv \delta/y_0$ characterizes the boundary layer thickness relative to the nominal thickness of the secondary anti-fountain near the wall.

The tangential velocity within the boundary layer is then

$$U_w = \frac{\partial \Psi_w}{\partial y} = U_s\left(1 - \beta\eta_w - \mathrm{e}^{-2\eta_w} - \frac{8}{3}\mathrm{e}^{-\eta_w}\sin\eta_w\right). \tag{3.30}$$

The presence of a vortical re-circulation region near the wall is in general indicated by a reversal in the sign of the tangential velocity U_w as a function of η_w. Consider the case where $e_1 < 0$ ($\beta > 0$), so that the flow in the bulk (outside boundary layers) is predominantly of fountain orientation. From the outer solution alone (non exponentially decaying terms of U_w), a recirculation region of height

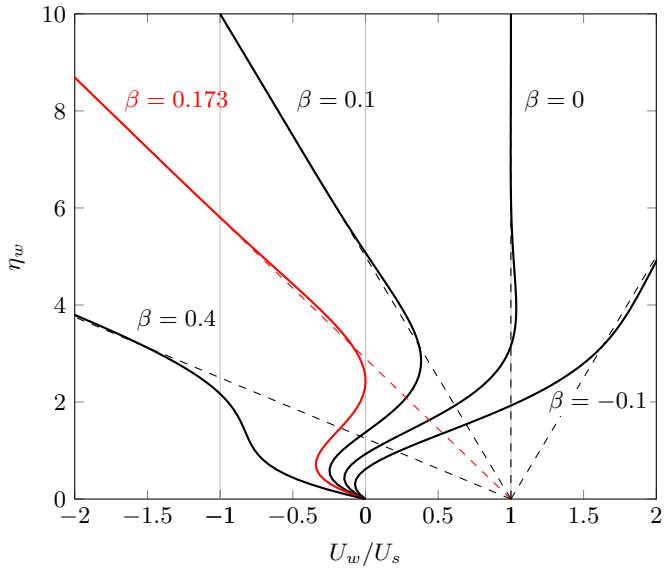

Figure 3.5 Tangential velocity profiles as function of the wall-normal boundary layer coordinate η_w for different values of $\beta = y_0/\delta$, showing the full wall-boundary layer solution (solid lines) and outer solution (dashed lines). The outer solution indicates the presence of secondary anti-fountain vortices within the region $y_0 < y < 0$, corresponding to $-1 < U_w/U_s < 1$. The inclusion of boundary layer terms, however, in general suppresses the size and strength of recirculation regions for $\beta > 0$, and completely suppresses any flow reversal near the wall for $\beta > 0.173$ (indicated in red).

$y = y_0$ (i.e. $\eta_w = 1/\beta$) is always expected for $\beta > 0$, corresponding to the region $-1 < U_w/U_s < 1$, cf. (3.23) and figure 3.3(a).

This is however generally not the case when boundary layer terms are included. Figure 3.5 plots the tangential velocity as a function of η_w for different values of β, showing that wall boundary layer terms greatly diminish both the flow speed and the extent of regions with radially outward velocity ($U_w/U_s > 0$) for $\beta > 0$, compared with the results from the outer solution (dashed lines). In particular, we find that for $\beta \geq \beta_c \approx 0.173$, $U_s(\eta)$ is negative definite. This means that the secondary anti-fountain is suppressed entirely if $y_0 \geq 0.173\,\delta$, or equivalently if $e_1 \leq -0.032/\delta$. For typical experimental parameters, we have $\delta \approx 0.14$, which implies that no flow reversal can occur near the wall for $e_1 \leq -0.2$, a condition that is easily satisfied for strongly excited surface mode amplitudes (cf. figure 3.4a). This dampening of the anti-fountain by the wall boundary layer, compounded with the faster radial decay of the flow velocity near the wall (r^{-3}) compared with the bulk (r^{-2}) justifies the absence of strong secondary vortices near the wall in experiments.

A useful simplification is therefore to neglect the contributions of the wall boundary layer to

the outer streaming entirely, i.e. to set ψ_s to zero in (3.16), and the analysis that follows it. Note that this completely suppresses the wall anti-fountain (and the wall boundary layer structure), and therefore does not predict any transition to anti-fountains at large frequencies (which relies on the radially outward slip velocity at the edge of the wall boundary layer). Nevertheless, this leads to a consistent description of the flow at low frequencies, where the strength of the mixed-mode bubble streaming (fountains) greatly outweighs wall-streaming (anti-fountains) contributions.

3.6 Two dimensional bubble streaming in a channel

We outline a method to modify the steady two-dimensional half-space streaming flow solution Ψ developed in section 3.3 of this chapter (see also Rallabandi et al. [77]), so as to incorporate a no-slip wall at $y = h$, while leaving boundary conditions at the bubble and the $y = 0$ wall undisturbed. We will employ the modification

$$\Psi \mapsto \Psi + \chi,$$

where χ is a correction flow to account for finite h. If ψ already satisfies the appropriate boundary conditions at $r = 1$ and $y = 0$, and χ is a Stokes flow (neglecting boundary layer terms), we have (temporarily neglecting bubble boundary conditions)

$$\begin{aligned}
&\nabla^4 \chi = 0 \quad \text{in} \quad \Omega \\
&\partial_x \chi = \partial_y \chi = 0, \quad \text{on} \quad y = 0 \\
&\partial_y \chi = -\partial_y \Psi \equiv u(x), \quad \text{on} \quad y = h \\
&\partial_x \chi = -\partial_x \Psi \equiv -v(x), \quad \text{on} \quad y = h.
\end{aligned} \tag{3.31}$$

Solutions to (3.31) can be obtained using a Fourier transform pair in x defined by

$$\hat{f}(k) = \int_{-\infty}^{\infty} f(x) \mathrm{e}^{-\mathrm{i}kx} \mathrm{d}x, \quad f(x) = \frac{1}{2\pi} \int_{-\infty}^{\infty} \hat{f}(k) \mathrm{e}^{\mathrm{i}kx} \mathrm{d}k. \tag{3.32}$$

The solution to the Fourier transform of χ is then

$$\hat{\chi}(k, y) = \hat{a} \cosh ky + \hat{b} \sinh ky + \hat{c} y \cosh ky + \hat{d} y \sinh ky, \quad k \neq 0, \tag{3.33}$$

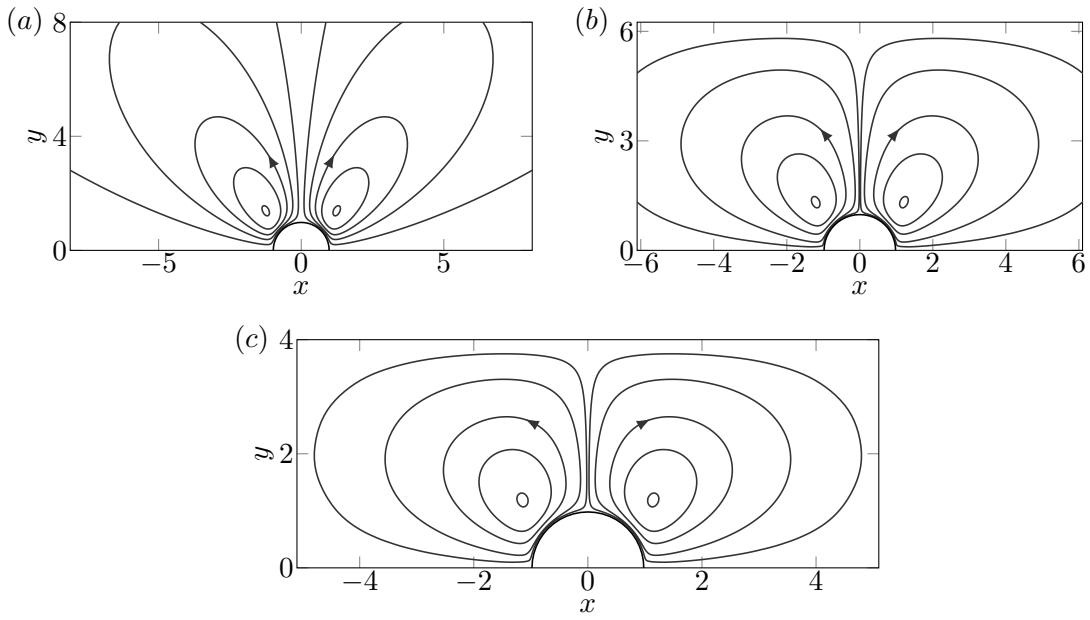

Figure 3.6 Streamline portraits of the flow at 20 kHz for (a) the half-space solution $h \to \infty$, (b) $h = 6.25$ and (c) $h = 4$. The experimental data presented in the dissertation most commonly correspond to $h = 6.25$ ($H = 250\mu$m, $a = 40\mu$m).

where

$$\begin{aligned}
\hat{a} &= 0 \\
\hat{b} &= -\frac{2\mathrm{i}}{k}\frac{\hat{v}\,kh\cosh kh + (\mathrm{i}\hat{u}\,kh + \hat{v})\sinh kh}{1 + 2k^2h^2 - \cosh 2kh} \\
\hat{c} &= -\hat{b}k \\
\hat{d} &= 2\frac{\hat{u}\,kh\cosh kh - (\hat{u} + \mathrm{i}\hat{v}\,kh)\sinh kh}{1 + 2k^2h^2 - \cosh 2kh}.
\end{aligned} \tag{3.34}$$

The superposition $\Psi + \chi$ obeys both $y = 0$ and $y = h$ wall boundary conditions, but now ignores bubble boundary conditions, applying inhomogeneous normal velocities and tangential stresses at $r = 1$. These inhomogeneities are accommodated by a second complementary flow obtained by a combination of half-space no-slip Stokes solutions [see e.g. 77], which introduce new inhomogeneities at $y = h$. Iterative application of (i) Fourier analysis to satisfy boundary conditions at $y = h$ and (ii) half-space no-slip solutions to satisfy bubble boundary conditions yields the appropriate two-dimensional streaming solution ψ for arbitrary h. For $h \gtrsim 4$, two of these iterations are sufficient to implement all boundary conditions to excellent accuracy. Figure 3.6 shows streamline portraits at different channel heights. Streamlines are in general flattened in the y directions and broadened

in the x direction. The introduction of an opposite wall at finite h typically does not influence the maximum streaming speed, which occurs close to the bubble, for a fixed combination of oscillatory modes. It should be noted however that the presence of the opposite wall may however modify the dynamic response itself, which we do not probe in this work.

3.7 Conclusions

This work has completed an asymptotic derivation of two-dimensional microstreaming from sessile bubbles: Using only the dimensionless driving frequency λ and damping coefficient γ as inputs, bubble mode oscillation amplitudes and phases can be derived, from which in turn follow the coefficients of the functions governing the streaming flow. For low to moderate λ, the flow is a mixed-mode streaming dominated by neighbouring-mode contributions that, because of their relative phase, lead to the generic fountain streaming pattern observed in experiment. As different pairs of neighbouring modes contribute very similarly at their respective resonance frequencies, the fountain pattern remains robust for a large range of λ. At high frequencies, the product of neighbouring-mode amplitudes is too small, however, to overcome the – always present – effect of wall-induced streaming, which contributes a second, anti-fountain (counter-rotating) vortex system to the flow. These predictions are borne out by experimental results. Exceedingly weak at low frequencies, the anti-fountain flow dominates at high λ and allows for complete reversal of the flow pattern upon frequency modulation, a valuable strategy e.g. in mixing applications [79, 112].

Simple analytical expressions have been obtained for the dominant (far-field) flow terms in both the fountain and anti-fountain cases, as well as for the positions of vortex centres and separatrices in the streaming flow. With this added insight, streaming flows from individual bubbles can now be described with just a few coefficients and tailored to suit the needs of a particular experiment. Moreover, as all flows are described in the limit of small streaming Reynolds number, they can be superimposed, and the design of devices featuring multiple bubbles in varying positions as well as superimposed channel flows is feasible without extensive calculations or trial-and-error. The half-space solutions are modified using a combination of Fourier transforms and Stokes singularities to yield streaming flows within channels of arbitrary height. The two-dimensional flows thus obtained satisfy all boundary conditions at the bubble and and the surrounding walls, and therefore serve as

building blocks for the description of flows in practically realizable experiments.

Chapter 4

Three-dimensional streaming under confinement

Steady streaming vortex flow from microbubbles has been developed into a versatile tool for microfluidic sample manipulation. For ease of manufacture and quantitative control, set-ups have focused on approximately two-dimensional flow geometries based on semi-cylindrical bubbles. In this chapter[1], we build upon our two-dimensional streaming theory and demonstrate how the necessary flow confinement perpendicular to the cylinder axis gives rise to non-trivial three-dimensional flow components. This is an important effect in applications such as sorting and micromixing. Using asymptotic theory and numerical integration of fluid trajectories, it is shown that the two-dimensional flow dynamics is modified in two ways: (i) the vortex motion is punctuated by bursts of strong axial displacement near the bubble, on time scales smaller than the vortex period; and (ii) the vortex trajectories drift over time scales much longer than the vortex period, forcing fluid particles onto three-dimensional paths of toroidal topology. Both effects are verified experimentally by quantitative comparison with APTV measurements of streaming flows. We apply our theory to qualitatively describe previously observed axial flows in nominally 2D microstreaming flows driven by oscillating cylinders. It is further shown that the long-time flow patterns obey a Hamiltonian description that is applicable in general to confined Stokes flows beyond microstreaming.

4.1 Introduction

Oscillations of a boundary relative to surrounding viscous fluid can give rise to secondary steady currents. These steady flows, driven by non-zero Reynolds stresses due to the inertia of the fluid oscillation, have been termed (boundary) "streaming flows" and are observed in a wide variety of applications [39, 46, 70]. Classical studies of such streaming phenomena have focussed on translational

[1]This chapter is adapted from parts of Rallabandi et al. [78] and Marin et al. [54].

oscillations of solids [81–83, 101]. More recently there has been increased interest in streaming due to bubbles undergoing a combination of volume and shape oscillations primarily for two reasons: (a) bubbles allow for a more powerful actuation of the flow due to the large amplitudes that may be accessed (the streaming speed being quadratic in the oscillation amplitude) and (b) flows over bubbles, which generally permit slip, are subject to little frictional resistance compared to those over solid no-slip surfaces. This makes acoustically excited bubbles particularly attractive for microfluidics, where they have been successfully used for applications such as particle trapping [51, 87, 110], size-selective sorting [111], shear force actuation [55] and microfluidic mixing [2, 44, 112, 114].

In order to obtain streaming flows that are not only powerful, but conceptually simple and easy to manufacture in a microfluidic context, initial work on hemispherical bubbles [55, 56] has widely been replaced by a two-dimensional geometry [73, 74, 110, 111, 118, 120]: In such microstreaming devices, the bubble has a semi-cylindrical shape and is sessile on the wall of the device (see figure 4.1*a*). The bubble is confined axially by two parallel walls (henceforth called top and bottom walls), which establishes a stable interface attached to the device by means of pinned contact lines. It has been shown that the symmetry of the set-up establishes approximately two-dimensional flows close to the mid-plane of the channel (where the flow is fastest) [77, 109, 112]. The two-dimensional theory, however, must have limitations close to the top and bottom walls of the channel, where the flow speed approaches zero. It is important to quantify any three-dimensional flow effects, which may affect applications such as mixing or sorting either beneficially or adversely. Until now, no study has developed a systematic theory of 3D streaming.

In the present chapter, we build on the two-dimensional streaming theory of chapter 3 and show that the presence of the top and bottom walls, together with the oscillatory properties of the bubble surface, introduce characteristic secondary axial flow components that are not confined to the vicinity of the walls, but introduce qualitative changes to the entire flow field. The superposition of the primary two-dimensional streaming and the secondary axial flows results in a three-dimensional flow field that explains recent experimental particle trajectory data measured by Astigmatism Particle Tracking Velocimetry (APTV) experiments [9, 54]. We show how our theory describes new aspects of particle motion in streaming flows over both short and long time scales, adding important new insight. The results are then generalized to any simple superposition of two-dimensional and

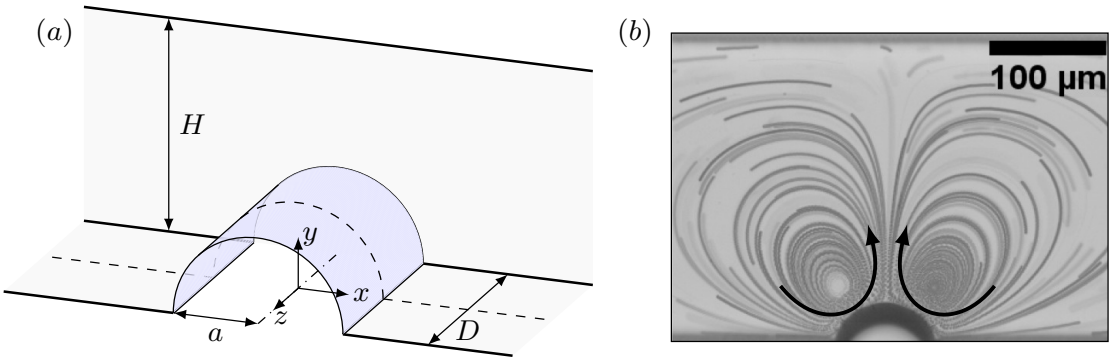

Figure 4.1 (a) Geometry of the microchannel, showing the bubble and the coordinate system; (b) Experimental flow lines in a $d = 2.5$, $h = 6.25$ channel showing the predominant two-dimensional "fountain mode" streaming (indicated by arrows), visualized using signals from tracer particles of 2 µm diameter in a region of $\sim 10\,\mu$m around the channel mid-plane ($z = 0$).

axisymmetric flow components in the framework of a Hamiltonian flow theory on long time scales, establishing a broader applicability to general axially confined two-dimensional flows.

4.2 Problem definition and governing equations

Figure 4.1 illustrates the typical geometry of a microbubble used to drive streaming flows in a microfluidic device: The semi-cylindrical bubble of radius a protrudes from a blind side channel of width $2a$ branching off a main channel, whose opposite wall (in the y-direction) is at a distance of $H = ha$. The entire structure has a uniform depth $D = da$ in the z-direction for ease of manufacture, so that the bubble axis spans the depth of the microchannel, see figure 4.1(a). The bubble contact lines at $(x = \pm a, y = 0)$ are pinned to the side channel corners. The channel is filled with a fluid of kinematic viscosity ν and density ρ. The application of an acoustic driving pressure at an angular frequency $\omega = 2\pi f$ (via a piezoelectric transducer) drives harmonic oscillations of the bubble surface at a characteristic amplitude ϵa, where $\epsilon \ll 1$. Note that for the typical sizes ($a \sim 50\,\mu$m) and frequencies ($f \sim 20\,$kHz) the acoustic wavelength is much greater than the bubble size. We use a and ω^{-1} to normalize length and time respectively for the rest of this chapter, consistent with previous chapters.. Oscillations of the interface drive a flow field which, in the limit of small oscillation amplitude, is conveniently solved for by an expansion in powers of ϵ [11, 47, 77, 84, 86, 90].

The primary oscillatory flow $\boldsymbol{u}_0$ (characteristic scale $\epsilon a\omega$) is irrotational except in viscous boundary layers of dimensionless thickness $\delta \equiv a^{-1}\sqrt{2\nu/\omega} \ll 1$, near the boundaries of the domain

[46, 47, 70]. Steady Reynolds stresses due to the oscillatory flow drive a secondary steady Eulerian flow $\langle \boldsymbol{u}_1 \rangle$ ($\langle \cdot \rangle$ denotes the time average over an oscillation cycle), with a characteristic velocity scale $U_s = \epsilon^2 a\omega$ and a streaming Reynolds number $Re_s = U_s a/\nu$, which is $\ll 1$ in many practical situations [47, 70, 86, 119], including microfluidics applications [90, 110, 112]. The time-averaged motion of fluid elements under the combination of the primary and secondary flows can be described in terms of a steady Lagrangian velocity field $\boldsymbol{U} = \langle \boldsymbol{u}_1 \rangle + \boldsymbol{u}_d$, where $\boldsymbol{u}_d$ is the Stokes drift, defined in (2.17).

It is this time averaged *Lagrangian* motion of the fluid that is practically relevant for fluid transport and is normally referred to as the "steady streaming". Figure 4.1(b) shows the typical appearance of the steady streaming flow from a sessile bubble as viewed along the axis of the bubble. It was observed experimentally [109, 112] and shown theoretically [77] that this pattern of a vortex pair in "fountain" orientation (flow upwards at $x = 0$) persists virtually unchanged over a range of frequencies. It was also observed [109] that the pattern does not vary much with the depth z (compare out-of-focus tracks with the in-focus tracks closer to $z = 0$, in figure 4.1b). However, the latter observations of the 2D character of the flow were limited by the microscopic depth of field ($\gtrsim 10\,\mu$m) and the general inability to follow individual particles over long times. We will show here that new flow features appear beyond 2D flow, and that they can be verified by more sophisticated experimental techniques.

For a theoretical description of the streaming $\boldsymbol{U}$, it is convenient to first write the Reynolds stress term $\boldsymbol{\sigma} \equiv \langle \boldsymbol{u}_0 \cdot \boldsymbol{\nabla} \boldsymbol{u}_0 \rangle$ as $\boldsymbol{\sigma} = \boldsymbol{\nabla} \left\langle \frac{1}{2} |\boldsymbol{u_0}|^2 \right\rangle + \langle (\boldsymbol{\nabla} \times \boldsymbol{u}_0) \times \boldsymbol{u}_0 \rangle$. Using the viscous stress scale $\rho \nu u_s/a$ to non-dimensionalize the time-averaged pressure, the dimensionless governing equations for the Lagrangian steady flow in the limit $Re_s \ll 1$ are

$$\begin{aligned} \boldsymbol{\nabla} \cdot \boldsymbol{U} &= 0, \\ \nabla^2 \boldsymbol{U} &= \nabla^2 \boldsymbol{u}_d + \nabla p + \boldsymbol{f}\,, \end{aligned} \tag{4.1}$$

where

$$p = \langle p_1 \rangle + \frac{2}{\delta^2} \left\langle \frac{|\boldsymbol{u}_0|^2}{2} \right\rangle, \quad \text{and} \quad \boldsymbol{f} = \frac{2}{\delta^2} \langle (\boldsymbol{\nabla} \times \boldsymbol{u}_0) \times \boldsymbol{u}_0 \rangle\,. \tag{4.2}$$

Here, p is a dimensionless effective pressure that incorporates both the time-averaged fluid pressure

$\langle p_1 \rangle$ and the kinetic energy of the oscillatory flow, and $\boldsymbol{f}$ is a body force related to the advection of oscillatory vorticity, which is confined to viscous boundary layers [86]. The Lagrangian mean flow is no-penetration with a vanishing tangential stress at the mean bubble surface $\partial\Omega_b$, and satisfies no-slip boundary conditions at the rigid wall surfaces $\partial\Omega_w$,

$$\begin{aligned} \boldsymbol{U} &= 0 \quad \text{on} \quad \partial\Omega_w \\ U_r &= 0 \quad \text{on} \quad \partial\Omega_b \\ \boldsymbol{S}_{r\theta} &= \boldsymbol{S}_{rz} = 0, \quad \text{on} \quad \partial\Omega_b, \end{aligned} \tag{4.3}$$

where $\boldsymbol{S}$ is the symmetric part of $\boldsymbol{\nabla U}$. Outside viscous boundary layers, where $\boldsymbol{f}$ is exponentially small, the Eulerian steady flow $\langle \boldsymbol{u}_1 \rangle = \boldsymbol{U} - \boldsymbol{u}_d$ satisfies the Stokes equations, supported by the effective pressure p.

4.3 Axial streaming

To motivate the streaming solutions that will be developed in this section, we first provide the general form of the oscillatory flow $\boldsymbol{u}_0$, which ultimately drives (4.1) through the Reynolds stress and the Stokes drift. For typical practical applications, $\delta \ll 1$, allowing $\boldsymbol{u}_0$ to be evaluated using matched asymptotic expansions, with an "outer" potential flow outside boundary layers and "inner" (viscous boundary layer) solutions described by the unsteady Stokes equations [46, 70, 86]. The oscillatory outer flow may in general be expressed as a modal decomposition

$$\boldsymbol{u}_0 = \sum_{n=0}^{\infty} \sum_{m=0}^{\infty} \boldsymbol{u}_0^{mn}, \tag{4.4}$$

where

$$\boldsymbol{u}_0^{mn} = \mathrm{e}^{\mathrm{i}t} A_{mn} \left(2n\beta \mathrm{K}'_{2m}(2n\beta)\right)^{-1} \nabla\varphi_{mn}, \tag{4.5}$$

and

$$\varphi_{mn} = \mathrm{K}_{2m}(2n\beta r) \cos 2m\theta \cos 2n\beta z \tag{4.6}$$

is a cylindrical harmonic function ($\nabla^2\varphi_{mn} = 0$). Here, K_ν represents a modified Bessel function of the second kind, with $\mathrm{K}'_\nu(z) = \mathrm{d}/\mathrm{d}z(\mathrm{K}_\nu(z))$ and $\beta \equiv \pi/d$. A_{mn} are the (generally complex) coefficients of the Fourier decomposition of the interface deformation $\zeta(\theta, z)$ and are determined by bubble interface dynamics and the pinning of contact lines [112][2].

Of this general combination of modes, planar modes ($n = 0$) have the largest amplitudes due to their relatively small damping, driving flows that decay algebraically away from the interface. On the other hand, axial modes ($n > 0$), which drive flows that decay exponentially ($\sim \mathrm{e}^{-2n\beta r}$) away from the bubble surface are only weakly excited due to greater damping [see e.g. 94, 112]. Therefore to leading order, only planar modes of $\boldsymbol{u}_0$ contribute to (4.1), driving two-dimensional streaming in the absence of the confining top and bottom walls [77, 112], see figure 4.2(b). Such a two-dimensional description of the flow has been used successfully to explain the experimentally observed streaming patterns and velocity fields in the xy-plane in the case of oscillating bubbles [77], cf. figure 4.1(b) and solid cylinders [51]. In general, however, steady axial flow components (in the z-direction) should be present.

Such axial velocity components of the steady streaming may in particular be excited by two separate effects that are neglected in the two-dimensional theory: (i) the top and bottom walls necessitate that the steady fluid velocity vanish identically at the top and bottom walls ($z = \pm d/2$), and (ii) axial oscillation modes of the bubble introduce Reynolds stress components that drive axial motion of the fluid.

We focus our attention on solutions of (4.1) that are valid outside steady boundary layers of thickness $\delta \ll 1$ near the boundaries of the domain. Formally, we are interested in the outer steady solution of a matched asymptotic expansion; this will be understood henceforth unless otherwise stated. Linearity of the governing equations makes it convenient to express the (three-dimensional) Lagrangian steady velocity field $\boldsymbol{U}$ as a superposition of a two-dimensional steady solution $\boldsymbol{u}$ (cf. figure 4.2a, b) and a secondary solution $\boldsymbol{v}$ with non-zero axial velocity components, i.e.,

$$\boldsymbol{U}(r, \theta, z) = \boldsymbol{u}(r, \theta) + \boldsymbol{v}(r, \theta, z),$$

[2]The notation used for azimuthal and axial mode numbers (m and n respectively), differs slightly from that used in chapters 2 and 3.

so that $\boldsymbol{v}$ satisfies (4.1), with $\boldsymbol{u}_d$, p and $\boldsymbol{f}$ now taken expressly to be axially non-uniform, while planar components are addressed by $\boldsymbol{u}$.

The outer flow must also satisfy appropriate matching conditions for proper asymptotic matching with the boundary layer solutions at the mean bubble surface ($r = 1$) and at the top and bottom walls ($z = \pm d/2$). Since normal velocity variations are small over the boundary layer thickness, kinematic boundary conditions are directly applicable to the outer solution at all boundaries $\partial\Omega = \partial\Omega_w + \partial\Omega_b$,

$$\boldsymbol{v} \cdot \boldsymbol{n}_{\partial\Omega} = 0 \quad \text{on} \quad \partial\Omega, \tag{4.7}$$

where $\boldsymbol{n}_{\partial\Omega}$ is the unit normal to $\partial\Omega$.

No-slip conditions at the top and bottom walls are enforced with the help of steady boundary layers, which in general support large axial gradients of planar velocity components near $z = \pm d/2$. This establishes effective slip conditions on the Lagrangian outer flow at the top and bottom walls (generally a slip velocity of $O(1)$) that depend on the particulars of the oscillatory flow $\boldsymbol{u}_0$ [see e.g 46, 70]. Consider now the mixed boundary layer region near the contact line at the bottom wall, defined by $r = 1 + O(\delta)$, $z = -d/2 + O(\delta)$, where the structure of the no-slip wall boundary layer must conform to that of the no-stress bubble boundary layer. Within this region, the pinning of contact lines, reflected in (4.7), ensures that $U_r \sim U_z \sim O(\delta)$, which along with no-stress conditions at the bubble ($\partial_r(r^{-1}U_\theta) + r^{-2}\partial_\theta U_r = 0$), requires that $U_\theta \sim O(\delta^2)$. By symmetry, the same arguments are applicable to the flow in the vicinity of the contact line between the bubble and the top wall $r = 1$, $z = d/2$. All boundary layer velocity components are therefore $O(\delta)$ or smaller in the vicinity of the contact lines at the top and bottom walls. For proper asymptotic matching, the Lagrangian *outer flow* must therefore, to leading order in δ, satisfy no-slip conditions at $r = 1$, $z = \pm d/2$, which may be written as

$$\boldsymbol{v} = -\boldsymbol{u} \quad \text{on} \quad r = 1,\ z = \pm d/2. \tag{4.8}$$

The bubble boundary conditions are more involved, since Reynolds stresses at the bubble may in general depend on a large number of mode combinations that are sensitive to the oscillatory boundary layer structure [see e.g. 11, 47, 77]. Rather than compute these conditions exactly, we

analyze the azimuthal and axial symmetries of these terms, which are ultimately manifested in the streaming through the bubble boundary conditions (4.3) enforced at $r = 1$. Let us consider the Reynolds stress term engendered by the product of two arbitrary oscillatory flow modes $\boldsymbol{u}_0^{kl}$ and $\boldsymbol{u}_0^{mn}$ of (4.5), defined by $\boldsymbol{\sigma}^{kl,mn} = \left\langle \boldsymbol{u}_0^{mn} \cdot \boldsymbol{\nabla} \boldsymbol{u}_0^{kl} + \boldsymbol{u}_0^{kl} \cdot \boldsymbol{\nabla} \boldsymbol{u}_0^{mn} \right\rangle$. Outside steady boundary layers, we have

$$\begin{aligned}
\boldsymbol{\sigma}^{kl,mn} &= \frac{A_{mn}^* A_{kl}}{8nl\beta^2 \, \mathrm{K}_{2m}'(2n\beta)\mathrm{K}_{2k}'(2l\beta)} \nabla \left(\nabla \varphi_{mn} \cdot \nabla \varphi_{kl} \right) \\
&= \frac{A_{mn}^* A_{kl}}{8nl\beta^2 \, \mathrm{K}_{2m}'(2n\beta)\mathrm{K}_{2k}'(2l\beta)} \times \\
&\qquad \nabla \sum_{i=1}^{2} \sum_{j=1}^{2} \lambda_{ij}^{kl,mn}(r) \, \cos[2(m + (-1)^i k)\theta] \, \cos[2(n + (-1)^j l)\beta z], \qquad (4.9)
\end{aligned}$$

where the asterisk denotes the complex conjugate and

$$\lambda_{ij}^{kl,mn} = \frac{1}{4} g_{mn}'(r) g_{kl}'(r) - \left[(-1)^i mk + (-1)^j \beta^2 nl \right] g_{mn}(r) g_{kl}(r), \qquad (4.10)$$

with $g_{mn}(r) \equiv \mathrm{K}_{2m}(2\beta n r)$. The same azimuthal and axial symmetries also appear in analogous modes of the Stokes drift terms $\boldsymbol{u}_d^{kl,mn}$ defined by

$$\boldsymbol{u}_d^{kl,mn} \equiv \left\langle \left(\int \boldsymbol{u}_0^{mn} \mathrm{d}t \cdot \boldsymbol{\nabla} \right) \boldsymbol{u}_0^{kl} + \left(\int \boldsymbol{u}_0^{kl} \mathrm{d}t \cdot \boldsymbol{\nabla} \right) \boldsymbol{u}_0^{mn} \right\rangle. \qquad (4.11)$$

Through (4.1), these axial and azimuthal dependences of $\boldsymbol{\sigma}^{kl,mn}$ and $\boldsymbol{u}_d^{kl,mn}$ are reflected directly in the steady outer solution [see e.g. 11, 47, 113].

To first approximation, due to their large amplitudes, products of planar modes ($n = 0$) contribute most strongly to (4.9), driving two-dimensional flow. Non-trivial axial dependences of $\boldsymbol{\sigma}$ arise predominantly from the product of the most strongly excited axial mode $m = 0, n = 1$ (oscillating axisymmetric quadrupole) with the dominant two-dimensional mode $k = l = 0$ (oscillating line source). The resulting forcing $\boldsymbol{\sigma}^{00,01}$, by (4.9), is axisymmetric, with an axial wavelength equal to the channel depth d, forming the most strongly excited mode of the forcing term $\boldsymbol{\sigma}$. Decomposed into its components in cylindrical coordinates, and neglecting higher order mode combinations, $\boldsymbol{\sigma}$

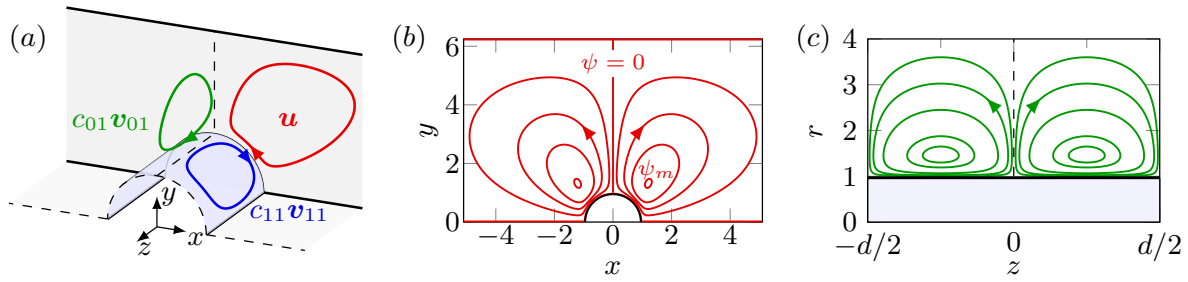

Figure 4.2 (a) Schematic of the flow superposition of modes in (4.20), indicating the planar fountain $\boldsymbol{u}$, the axisymmetric fountain $c_{01}\boldsymbol{v}_{01}$, and the mixed axial-azimuthal mode $c_{11}\boldsymbol{v}_{11}$. ($b$) streamline portrait of the planar flow $\boldsymbol{u}$ for a channel height $h = 6.25$, indicating limiting streamlines ψ: $\psi = \psi_m$ corresponds to the vortex center of the 2D flow (smallest streamline) and $\psi = 0$, the largest streamline. (c) indicates flow lines of the axisymmetric flow in an $r - z$ plane, showing a fountain orientation (radially outward velocities at $z = 0$). The shaded region $r < 1$ indicates the bubble.

therefore takes the approximate form

$$\boldsymbol{\sigma} \approx \boldsymbol{\sigma}^{00,01} = A_{00}A_{01}^{*}\left\{\sigma_r(r)\cos 2\beta z, 0, \sigma_z(r)\sin 2\beta z\right\}, \tag{4.12}$$

where $\sigma_r(r)$ and $\sigma_z(r)$ are determined by the oscillatory flow functions. Note also that retaining the same axial modes $(0, 1)$, but including higher order planar modes $(k > 0, l = 0)$ results in Reynolds stresses with both axial and azimuthal variation. Reynolds stress terms quadratic in axial mode amplitudes, as well as contributions involving higher-order axial modes, are subdominant due to the their weak excitation and will be ignored here. As we shall show presently, flows excited due to these modes are further suppressed by their strong radial decay away from the bubble surface.

4.3.1 Separable Stokes solutions

Motivated by the axial and azimuthal symmetries of the Reynolds stresses at the bubble (4.9), we seek separable solutions of (4.1). In general, the velocity field $\boldsymbol{v}$ may be decomposed into its irrotational (conservative) part $\boldsymbol{v}^C$ and a rotational (non-conservative) part $\boldsymbol{v}^N$ [13, 14]. The irrotational part of the flow has a form similar to (4.5) and is expressible in terms of the cylindrical harmonics φ_{mn} given by (4.6), allowing $\boldsymbol{v}^C_{mn} \equiv \nabla\varphi_{mn}$ to satisfy the kinematic condition at all solid walls, but not at the bubble. For completeness, we give the expression for the components of $\boldsymbol{v}^C_{mn}$

in cylindrical coordinates (r, θ, z):

$$\boldsymbol{v}^C_{mn} = \left\{ u^C_{mn}(r) \cos 2m\theta \cos 2n\beta z, v^C_{mn}(r) \sin 2m\theta \cos 2n\beta z, w^C_{mn}(r) \cos 2m\theta \sin 2n\beta z \right\}, \tag{4.13}$$

where

$$\left.\begin{aligned} u^C_{mn}(r) &= -\frac{2n\beta}{2} \left(\mathrm{K}_{2m+1}(2n\beta r) + \mathrm{K}_{2m-1}(2n\beta r) \right) \\ v^C_{mn}(r) &= -\frac{2m}{r} \mathrm{K}_{2m}(2n\beta r) \\ w^C_{mn}(r) &= -2n\beta \mathrm{K}_{2m}(2n\beta r). \end{aligned}\right\} \tag{4.14}$$

The no-penetration condition at the bubble is satisfied by making use of the rotational, pressure dependent solutions of the Stokes equations ($\boldsymbol{v}^C$ is, by definition, pressure independent). The effective pressure p itself is harmonic outside boundary layers ($\nabla^2 p = 0$) due to (4.1), and may be decomposed into cylindrical harmonics (4.6). For the dimensionless pressure mode $p_{mn} = \varphi_{mn}$, rotational solutions $\boldsymbol{v}^N_{mn}$ of the Stokes equations ($\nabla^2 \boldsymbol{v}^N_{mn} = \nabla p_{mn}$) take the form

$$\boldsymbol{v}^N_{mn} = \left\{ u^N_{mn}(r) \cos 2m\theta \cos 2n\beta z, v^N_{mn}(r) \sin 2m\theta \cos 2n\beta z, w^N_{mn}(r) \cos 2m\theta \sin 2n\beta z \right\}, \tag{4.15}$$

where

$$\left.\begin{aligned} u^N_{mn}(r) &= -\frac{m}{2n\beta} \mathrm{K}_{2m+1}(2n\beta r) + \frac{r}{2} \mathrm{K}_{2m+2}(2n\beta r) \\ v^N_{mn}(r) &= \frac{m+1}{2n\beta} \mathrm{K}_{2m+1}(2n\beta r) \\ w^N_{mn}(r) &= \frac{r}{2} \mathrm{K}_{2m+1}(2n\beta r). \end{aligned}\right\} \tag{4.16}$$

Neglecting any axial Stokes drift contributions to the Lagrangian flow, the corresponding Lagrangian streaming mode $\boldsymbol{v}_{mn}$ that satisfies the no-penetration condition at the interface $r = 1$ and at the walls $\partial\Omega_w$, normalized to have unit peak axial velocity at $\partial\Omega_b$, may be written as

$$\boldsymbol{v}_{mn} = \left(\frac{w^C_{mn}(1)}{u^C_{mn}(1)} - \frac{w^N_{mn}(1)}{u^N_{mn}(1)} \right)^{-1} \left(\frac{\boldsymbol{v}^C_{mn}}{u^C_{mn}(1)} - \frac{\boldsymbol{v}^N_{mn}}{u^N_{mn}(1)} \right). \tag{4.17}$$

A general class of no-penetration Stokes solutions may be constructed using linear combinations of $\boldsymbol{v}_{mn}$ (over m and n), determined simultaneously by boundary conditions at the bubble and at the walls. Note, however, that $\boldsymbol{v}_{mn}$ are characterized by exponential radial decays ($\propto \mathrm{e}^{-2n\beta r}$). The

dominance of the lowest axial mode in the Reynolds stress, together with the exponential radial decays of (4.17) into the fluid away from the bubble surface ensures that the lowest (non-trivial) axial modes are both (i) the most strongly forced, and (ii) the predominant axial streaming solutions in the bulk of the flow. It is therefore appropriate to consider only the lowest axial modes ($n = 1$) of (4.17), so that

$$\boldsymbol{v} \approx \sum_{m=0}^{\infty} c_{m1} \boldsymbol{v}_{m1}, \tag{4.18}$$

where the c_{m1} are determined by the slip condition (4.8) at the top and bottom wall. Since (4.18) is only a truncated representation of the flow, rather than satisfying the slip condition rigorously for all $r > 1$, we will focus on satisfying it only at $r = 1$. This is an appropriate simplification since the axial solutions presented here modify the flow significantly only near $\partial\Omega_b$, where the slip at walls due to the planar solution $\boldsymbol{u}$ is the greatest [77]. At $r = 1$, the slip condition (4.8) along with (4.18) when decomposed into a Fourier series in θ, yields the coefficients

$$c_{m1} = -\frac{\displaystyle\int_0^{\pi} \boldsymbol{u}(1,\theta) \cdot \hat{\boldsymbol{\theta}} \sin 2m\theta \, \mathrm{d}\theta}{\displaystyle\int_0^{\pi} \boldsymbol{v}(1,\theta,d/2) \cdot \hat{\boldsymbol{\theta}} \sin 2m\theta \, \mathrm{d}\theta}, \tag{4.19}$$

where $\hat{\boldsymbol{\theta}}$ is the unit vector in the azimuthal direction.

Note that (4.19) does not determine the strength of the axisymmetric solution c_{01}, since (4.19) is specifically a statement of vanishing azimuthal velocity at the interface. It should be expected, however, that such a flow component is in general excited, in particular due to bubble oscillations that set up axisymmetric Reynolds stresses (4.12). The structure of the axisymmetric flows (r, z) is entirely analogous to planar flows (r, θ) in the xy-plane with respect to the governing equations and boundary conditions, albeit weaker in overall magnitude due to weaker forcing (smaller axial oscillation amplitudes). This suggests that the axisymmetric solution also inherits the "fountain" structure of the two-dimensional solution due to the pinning of contact lines at the top and bottom walls [see e.g. 77, 112], with radially outward velocities at the mid-plane ($z = 0$) and radially inward velocities near the top and bottom walls (cf. figures 4.2*b* and 4.2*c*) .

In principle c_{01} may be evaluated from a detailed calculation of the Reynolds stresses. This however requires both (i) a resolution of the axial oscillation mode amplitudes A_{mn} as functions

of frequency [see e.g. 23, 112], and (ii) a detailed description both oscillatory and steady no-stress boundary layers due to these flow modes, accurate up to $O(\delta^2)$ [see e.g. 11, 47, 77]. We do not attempt to carry out this analysis rigorously here, but rather estimate c_{01} by considering the ratio between damping coefficient γ_{00} of the monopole ($m = 0, n = 0$) to that of the lowest axial mode ($m = 0, n = 1$), denoted by γ_{01}; cf. equation (21) of Wang et al. [112]. In the limit of small damping, the relative mode amplitude scales inversely with the relative damping coefficient; for the channel aspect ratio used in the present experiments ($d/a = 2.5$), this results in $|A_{01}|/|A_{00}| \approx \gamma_{00}/\gamma_{01} \approx 0.32$. Under the present normalization ($|A_{00}| = 1$), the velocity scale due to product of the monopole and the axisymmetric quadrupole is therefore $\sim 0.32u_s$, resulting in $|c_{01}| \sim 0.32$. The value of c_{01} inferred from experimental measurements, described in more detail in section 4.5, agrees closely with this estimate.

For $m \geq 1$, the coefficients c_{m1} may be computed directly from the two-dimensional theory, using (4.19). The "fountain" structure of the planar flow $\boldsymbol{u}$ (one vortex per quadrant, cf. figure 4.2b), naturally leads by (4.19) to $|c_{11}| \gg |c_{m1}|$ for $m > 1$. Retaining therefore only terms of (4.18) proportional c_{01} and c_{11}, the leading contributions to the three-dimensional streaming flow may be written as

$$\boldsymbol{U} = \boldsymbol{u} + c_{01}\boldsymbol{v}_{01} + c_{11}\boldsymbol{v}_{11} \qquad (\boldsymbol{v} = c_{01}\boldsymbol{v}_{01} + c_{11}\boldsymbol{v}_{11}). \tag{4.20}$$

The two axial contributions $c_{01}\boldsymbol{v}_{01}$ and $c_{11}\boldsymbol{v}_{11}$ represent, respectively, the lowest axisymmetric and axial-azimuthal modes, and are depicted in figure 4.2. These contributions address, respectively, the excitation of steady flow due to axial bubble oscillations (axial oscillatory flow gradients) and the observance of no-slip conditions at axially confining walls.

4.4 Results and discussion

Before we discuss the resultant flow $\boldsymbol{U}$ in detail, it will prove useful to write the planar flow $\boldsymbol{u} = \{u_r, u_\theta, 0\}$ in terms of a stream function $\psi(r, \theta)$ so that $u_r = r^{-1}\partial_\theta\psi$ and $u_\theta = -\partial_r\psi$[3]. The steady two-dimensional flow is in general composed of a dominant fountain vortex and a sub-dominant anti-fountain vortex near the wall at $y = 0$ [77, 112]. Here, we neglect the effect of

[3]Note that ψ here represents the 2D steady Lagrangian streaming flow, introduced as Ψ in chapter 3 to distinguish it from other flow quantities. Similarly, $\boldsymbol{u}$ is the steady Lagrangian 2D streaming velocity field.

the anti-fountain near the wall, which is typically confined to a region comparable in extent to the boundary layer thickness δ, and is therefore greatly suppressed by the (no-slip) wall boundary layer structure (cf. chapter 3). The stream function ψ describing the two-dimensional Lagrangian streaming flow in a channel of finite height h is in general obtained by a modification of the solution obtained in the half-space ($h \to \infty$), by the procedure outlined in section 3.6. Focusing on the quadrant ($x > 0, y > 0$), the two-dimensional steady flow is characterized by a single vortex system (closed streamlines) governed by $\psi \in (\psi_m, 0)$, where $\psi = 0$ delineates the boundaries of the domain (largest enclosed area), and $\psi = \psi_m < 0$ identifies the two-dimensional vortex center (vanishing enclosed area, see figure 4.2*b*). The fountain vortex flow of figure 4.2(b), with its radially outward velocity near the symmetry plane $\theta = \pi/2$ [77, 111, 112] has a simple far-field approximation to the stream function for large channel height ($h \to \infty$), namely,

$$\psi \sim \frac{4e_1}{r} \sin^2\theta \cos\theta, \quad \text{as} \quad r \to \infty, \tag{4.21}$$

where e_1 is an $O(1)$ constant related to planar oscillation mode amplitudes and phases, and is negative for fountain-mode streaming [77], see also chapter 3.

The superposition of the two-dimensional Lagrangian streaming with the flows computed in the previous section yields a three-dimensional steady flow that satisfies (i) the Stokes equations, (ii) no-penetration conditions at all boundaries and (iii) no-slip conditions at the confining walls close to the interface. We will focus on material trajectories in this flow, given by solutions $\boldsymbol{x}(t)$ of $\dot{\boldsymbol{x}}(t) = \boldsymbol{U}(\boldsymbol{x}(t))$, which are integrated numerically using a fourth order Runge–Kutta scheme. Due to the symmetry of the problem, we focus our results on the region $x > 0, 0 < y < h, 0 < z < d/2$. The smallest time scale relevant to the steady flow is the time scale of fluid advection along the bubble interface, which we define as $T_s \equiv a/U_s = 1/(\epsilon^2\omega)$, and use to non-dimensionalize time for all the results following below.

The 2D vortex motion occurs over the nominal orbit time along closed 2D streamlines (under the action of $\boldsymbol{u}$ alone), which is much greater than T_s due to the algebraic decay of the flow velocity away from the bubble. In units of T_s, the dimensionless planar orbit time on a streamline $T(\psi)$ is

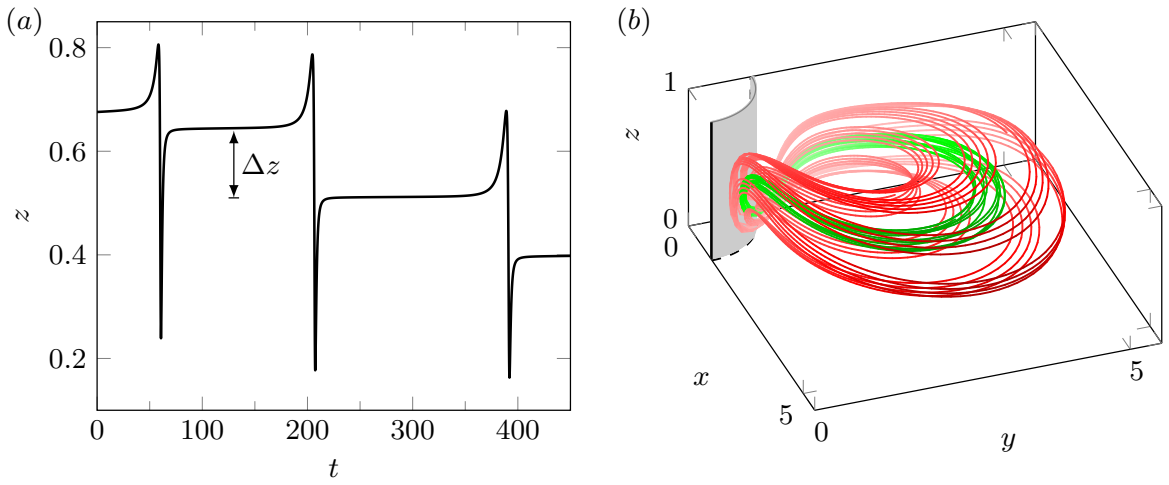

Figure 4.3 (a) Axial motion $z(t)$ of a typical fluid particle trajectory, showing the strong bursts of axial displacement (when the trajectory is close to the bubble surface) and the net axial displacement Δz over one cycle of radial motion. (b) Fluid particle trajectories for two different initial conditions, showing the nested torus structure: red is a trajectory of large axial extent, while green indicates a trajectory close to the "core" of the tori. Thick solid black lines indicate contact lines with bounding walls, dashed lines indicate the locations of symmetry planes.

in general defined by

$$T(\psi) = \oint_\psi \frac{1}{|\boldsymbol{u}|}\mathrm{d}s = \oint_\psi \frac{1}{|\nabla\psi|}\mathrm{d}s, \tag{4.22}$$

where $\mathrm{d}s = |\boldsymbol{u}|\mathrm{d}t$ is a differential arc length element along the streamline and the path of integration along ψ is counterclockwise. Using the far-field solution (4.21), one may estimate $T(\psi)$ as

$$T_{h\to\infty}(\psi) \approx \int_{\pi/2}^{0} \frac{r(\psi,\theta)}{u_\theta(\psi,\theta)}\mathrm{d}\theta = -\frac{\pi e_1^2}{2\psi^3}. \tag{4.23}$$

This estimate, valid for $h \to \infty$, becomes quantitatively modified for flow fields with finite h (see section 3.6), but the order of magnitude of $T(\psi) \sim 10T_s - 100T_s$ obtained from (4.23) remains valid.

4.4.1 3D effects on short and long time scales

The axial flows modify the 2D motion in at least two significant ways. Perhaps most strikingly, a fluid particle trajectory close to the bubble ($r \lesssim 1+d/(2\pi)$) shows strong bursts of axial displacement on the short time scale $\sim T_s$, much shorter than the 2D orbit time. Figure 4.3(a) shows an example of such a trajectory: as axial flow components of $\boldsymbol{v}$ very close to the bubble are in general comparable to planar velocity components due to the coupling (4.8), the fluid element approaches the bubble

and is advected along the interface (in the direction $\theta \to \pi/2$), suffering $O(1)$ axial displacements over the timescale T_s. The axial confinement necessitates a spatial reversal of the axial velocity components, so that a fluid element experiences axial displacements both towards and away from the mid-plane during the course of its motion near the bubble. As a consequence, the net axial displacement (Δz) of a fluid element over intermediate time scales $T(\psi)$, averaged over its nominal two-dimensional orbit, is typically small compared to the bubble radius (figure 4.3a).

Figure 4.3(b) illustrates the long-time effect of these net displacements: Similar to the axial Δz, planar components of $\boldsymbol{v}$ result in small deviations of the planar projections of fluid trajectories from nominally closed two-dimensional orbits. If the depth of the channel is on the order of the bubble radius (or greater), the small axial and planar drifts result in a motion over times scales longer still than $T(\psi)$, over which a fluid element explores a significant fraction of the half-channel by systematically sampling a succession of planar orbits of varying planar extents (varying ψ) at different depths z (cf. figure 4.8). The superimposed axial and radial motions result in quasi-periodic trajectories that fill toroidal structures in 3D (figure 4.3b). It can be seen that fluid elements at different initial positions follow toroidal trajectories of considerably varying spatial extents, none of which intersect. At the core of this nested system of tori is a singly periodic trajectory of vanishing toroidal volume.

The long-time toroidal motion of a fluid element is further illustrated in figure 4.4(a): its quasi-period τ depends on the initial position of the fluid particle, with net motion towards the mid-plane $z = 0$ occurring over the widest planar orbits ($\psi \sim 0$), followed by motion towards the wall ($z = d/2$) occurring over "tight" planar orbits that are closer to the two-dimensional vortex center ($\psi \sim \psi_m$). Reversals in the direction of the slow axial motion occur near the wall and the mid-plane, involving relatively large change in the planar extent of the quasi-planar orbits, i.e. a widening of tight orbits near the wall, and a tightening of wide orbits close to the mid-plane (see figure 4.4). As discussed in section 4.5, all elements of this motion are observed in experiment as well (figure 4.4b).

4.4.2 Generalized Hamiltonian theory of 3D effects

The wide spatial range explored by different material points underscores the importance of understanding the kinematics of these trajectories, particularly in the context of applications such as fluid

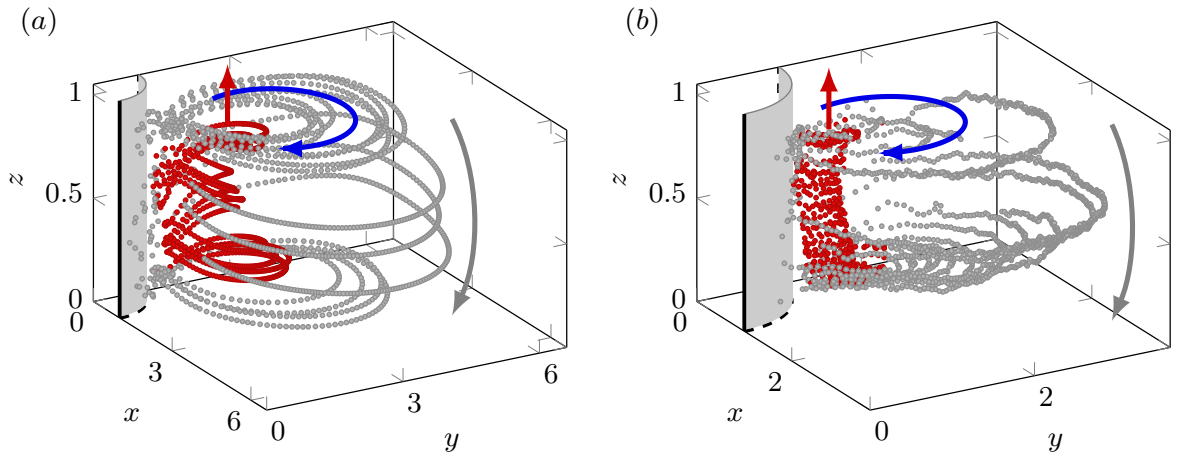

Figure 4.4 Typical toroidal trajectory, as (a) predicted by the theory for a fluid element, and (b) measured experimentally for an approximately passive tracer by APTV. The motion is towards the channel walls on the tight orbits (close to the nominal 2D vortex center), indicated in red, and towards the channel mid-plane during wider planar orbits, coloured grey. Arrows indicate these axial motions as well as the 2D fountain orientation (blue).

mixing and manipulation of microparticles in these flows.

By definition, the displacement in the z coordinate of a fluid element is simply the time integral of the axial component of the velocity field as a function of its instantaneous position $\boldsymbol{x}(t)$. However, the drift in the z coordinate of a fluid element over a time $T(\psi)$, denoted by Δz, is typically much smaller than the channel depth d (see figure 4.3a), with significant axial motion only occurring over much longer time scales. In the limit $\Delta z/d \ll 1$ (or otherwise $|\boldsymbol{v}| \ll |\boldsymbol{u}|$), the motion of the particle over a time $T(\psi)$ is therefore approximately planar to leading order in Δz, i.e. $\boldsymbol{x}(t) \approx \tilde{\boldsymbol{x}}(t) = \{r(t), \theta(t), z\}$ such that z and $\psi = \psi(r(t), \theta(t))$ are approximately constant over the motion. For $\Delta z/d \ll 1$, one may therefore compute Δz as the integral axial displacement of a fluid element as it traverses a nominally closed two-dimensional orbit (constant z and ψ), over the time $T(\psi)$. To first approximation, we may write

$$\Delta z(\psi, z) = \int_0^{T(\psi)} v_z(\boldsymbol{x}(t))\,\mathrm{d}t \approx \int_0^{T(\psi)} v_z(\tilde{\boldsymbol{x}}(t))\,\mathrm{d}t. \tag{4.24}$$

Note that the absolute values of the limits in the time integral are unimportant as long as their difference is $T(\psi)$ – this ensures an integral over the entire closed orbit ψ, valid for all material points on ψ. The Δz defined by (4.24) therefore represents the deviation of a material orbit from

planarity over the time $T(\psi)$.

The deviation from *closedness* of orbits over a time $T(\psi)$, when projected on the x-y plane, may be similarly quantified by a drift in ψ (denoted by $\Delta\psi$) of a fluid element. The time rate of change of the stream function value ψ sampled by a fluid element as it is advected by the 3D flow field $\boldsymbol{U}$ is simply the material derivative of ψ, which for steady flow is given by $\boldsymbol{U}\cdot\nabla\psi = \boldsymbol{v}\cdot\nabla\psi$. If we again assume small deviations from closedness over a planar orbit time scale, $\Delta\psi$ incurred over the time $T(\psi)$ is computed to first approximation as

$$\Delta\psi(\psi, z) = \int_0^{T(\psi)} \boldsymbol{v}(\boldsymbol{x}(t))\cdot\nabla\psi(\boldsymbol{x}(t))\,\mathrm{d}t \approx \int_0^{T(\psi)} \boldsymbol{v}(\tilde{\boldsymbol{x}}(t))\cdot\nabla\psi(\tilde{\boldsymbol{x}}(t))\,\mathrm{d}t \tag{4.25}$$

It may be shown (see Appendix C.2) that for an arbitrary incompressible velocity field $\boldsymbol{v}$, the approximate drifts Δz and $\Delta\psi$ (using $\tilde{\boldsymbol{x}}(t)$) defined respectively by (4.24) and (4.25), identically satisfy the differential continuity equation

$$\frac{\partial\Delta\psi}{\partial\psi} + \frac{\partial\Delta z}{\partial z} = 0, \tag{4.26}$$

This automatically allows them to be expressed in terms of a Hamiltonian $\mathcal{H}(\psi, z)$ as

$$\Delta\psi = \frac{\partial\mathcal{H}}{\partial z}, \quad \Delta z = -\frac{\partial\mathcal{H}}{\partial\psi}, \tag{4.27}$$

where $\mathcal{H}(\psi, z)$ may be written as

$$\mathcal{H}(\psi, z) \equiv -\int\oint_{\psi} \boldsymbol{v}\cdot\boldsymbol{n}\,\mathrm{d}s\,\mathrm{d}z, \tag{4.28}$$

and $\boldsymbol{n} \equiv -\nabla\psi/|\nabla\psi|$ is the local unit normal to streamlines in the xy plane; see appendix C.2 for a more detailed discussion. Since these drifts occur over a planar orbit time $T(\psi)$, one may define mean drift velocities as

$$\overline{v}_\psi(\psi, z) \equiv \frac{1}{T}\frac{\partial\mathcal{H}}{\partial z}, \quad \overline{v}_z(\psi, z) \equiv -\frac{1}{T}\frac{\partial\mathcal{H}}{\partial\psi}. \tag{4.29}$$

The system (4.29) constitutes precisely an incompressible two-dimensional flow field in the abstract ψ-z space, governed by the Hamiltonian $\mathcal{H}(\psi, z)$, which plays the role of a stream function

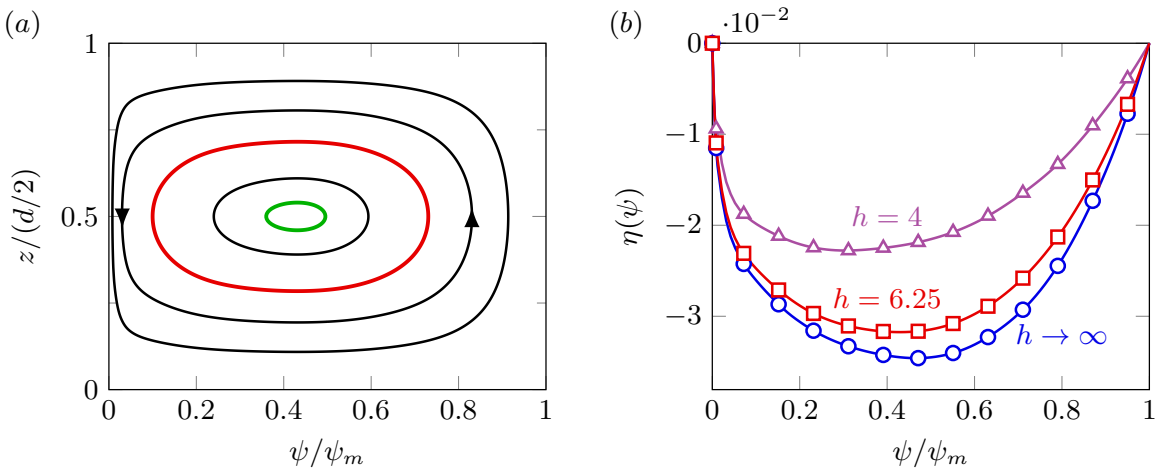

Figure 4.5 (a) Phase portrait of the Hamiltonian system in ψ-z space, computed for $h \to \infty$. Closed lines are curves of constant $\mathcal{H}$ representing 3D tori in real space, with the red and green trajectories corresponding to the respective tori in figure 4.4b. (b) Functions $\eta(\psi)$ at $f = 20\,\mathrm{kHz}$ and $d = 2.5$ for different channel heights h.

and remains invariant over the long-time three-dimensional steady motion of a fluid element. Since both $\boldsymbol{u}$ and $\boldsymbol{v}$ involve vanishing normal velocities on $\partial\Omega$, it follows from (4.28) and (4.29) that the flow in the abstract space does not penetrate its boundaries, i.e.

$$\overline{v}_\psi(\psi_m, z) = \overline{v}_\psi(0, z) = \overline{v}_z(\psi, 0) = \overline{v}_z(\psi, d/2) = 0. \tag{4.30}$$

This automatically ensures the existence of at least one elliptic point (ψ_c, z_c) at which $\partial_\psi \mathcal{H} = \partial_z \mathcal{H} = 0$, which represents a two-dimensional curve in real space given by $\psi(r, \theta) = \psi_c$, $z = z_c$. Any material point on this curve, by virtue of lying on a (stable) stagnation point of the ψ-z flow, remains confined to it under the action of the three-dimensional flow field, i.e. the curve in real space defined by (ψ_c, z_c) approximates the core of the system of nested toroidal fluid trajectories (cf. figure 4.3b). Curves of constant $\mathcal{H}$ in the vicinity of the core are concentric about it, spanning finite ranges of axial coordinates z and streamlines ψ and therefore delineate surfaces of the tori on which fluid elements move in real space. Figure 4.5(a) shows the ψ-z phase portrait that provides this simplified description of the 3D motion. It is noteworthy that this description assumes no particular forms for $\boldsymbol{u}$ and $\boldsymbol{v}$, only requiring that the two-dimensional flow is steady and characterized by closed streamlines, and is therefore in principle applicable to any perturbed two-dimensional flow under confinement.

For $\boldsymbol{v}$ given by (4.20) (single axial wavenumber), the Hamiltonian is separable and takes the form

$$\mathcal{H} = \eta(\psi) \sin 2\beta z, \tag{4.31}$$

so that

$$\overline{v}_\psi = \frac{2\beta}{T(\psi)} \eta(\psi) \cos 2\beta z, \quad \overline{v}_z = -\frac{1}{T(\psi)} \eta'(\psi) \sin 2\beta z. \tag{4.32}$$

The core trajectory is therefore located at $z_c = d/4$ and $\eta'(\psi_c) = 0$; note that $\eta'(\psi)$ is guaranteed to have at least one zero within the relevant range of stream function values $(\psi_m, 0)$. The temporal evolution of the stream function is therefore given by

$$\frac{\mathrm{d}\psi}{\mathrm{d}t} = \pm \frac{2\beta}{T(\psi)} \sqrt{\eta^2 - \mathcal{H}^2} \tag{4.33}$$

The characteristic function $\eta(\psi)$ itself is obtained from evaluating (4.28) and (4.31), and displayed in figure 4.5(b). Its shape is relatively insensitive to the channel width for not too small h.

Equation (4.33) may be solved numerically for given initial conditions (z_0, ψ_0). For trajectories that approach the core, $\mathcal{H} \sim \mathcal{H}(\psi_c, z_c)$, orbits in the ψ-z plane are elliptical so that $\psi(t)$ and $z(t)$ both vary sinusoidally with a single frequency. For arbitrary $\mathcal{H}$, the temporal motion is asymmetric over a 3D period τ due to the dependence of the drift velocities on $1/T(\psi)$, so that the axial dynamics are faster for smaller orbits $\psi/\psi_m \sim 1$, and slower for larger planar orbits $\psi/\psi_m \sim 0$. In real space, this corresponds to the faster axial motion towards the top wall ($z = d/2$) over tight planar orbits, and the slower axial drift towards the mid-plane ($z = 0$) over wider orbits, as depicted in figure 4.6(a), where the red line indicating the Hamiltonian theory captures the asymmetry of the long-time motion. The ψ-motion depicted in figure 4.6(b) is much more symmetric, but is also subject to abrupt jumps on the short time scale.

4.5 Experimental data for three-dimensional streaming flows

A microbubble streaming set-up of the type depicted in figure 4.1(a) was used to obtain three-dimensional trajectory data for approximately passive tracer particles (polystyrene beads of diameter 2 μm) utilizing Astigmatism Particle Imaging Velocimetry (APTV) [8, 9, 89]. In this optical

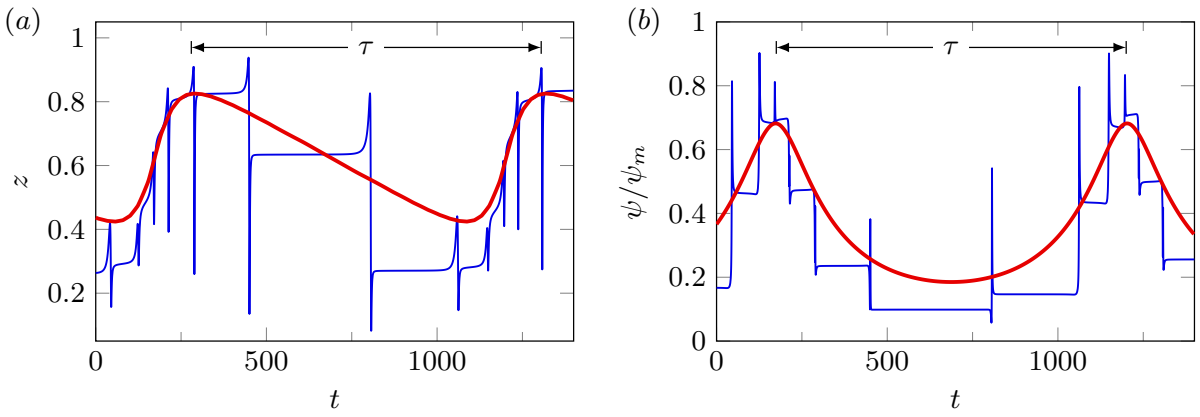

Figure 4.6 (a) Axial coordinate z and (b) normalized streamfunction ψ/ψ_m as functions of time, over approximately one 3D quasi-period τ. Blue lines represent the numerical integration of particle trajectories, while red lines show the predictions of the Hamiltonian theory, which captures the long-time kinematics while averaging over the shorter time scales.

imaging technique, the image of a spherical tracer particle is distorted by a cylindrical lens into elliptic shapes whose eccentricity depends on the depth coordinate of the particle along the optical axis. This allows for the quantification of all three velocity components of moving tracer particles in a 3D domain with a single camera. The experiments were conducted using $a = 40\,\mu\text{m}$, $f = 20\,\text{kHz}$, $d = 2.5$, and $h = 25$, with particle images taken by a high-speed camera connected to an inverted microscope, at a recording speed of 500 fps. The measurement uncertainty of this technique arises primarily from errors in particle detection and tracking, and the degree to which the elliptical shapes of the particle images can be accurately determined (see Rossi and Kähler [89] for details). For the present experiments, the measurement uncertainty in the position of a particle is $\approx \pm 0.1$ μm in the x and y directions and $\approx \pm 1$ μm in the z direction, much smaller than typical length scales of interest ($\sim 10\,\mu\text{m}$). More details about this use of the technique in a microfluidic context and more experimental data on bubble microstreaming are presented in Marin et al. [54]. Figure 4.4(b) displays an example trajectory that shows all the qualitative features predicted by the three-dimensional streaming theory: one trajectory typically occupies half the channel (between one wall and the midplane) and consists of approximately 2D trajectory loops whose radial extent is small as the particle displaces towards the wall, then widens to a greater radial extent as the z-motion reverses and the particle moves towards the midplane.

In order to model the axial motion quantitatively, we obtain the value of c_{01} from the experi-

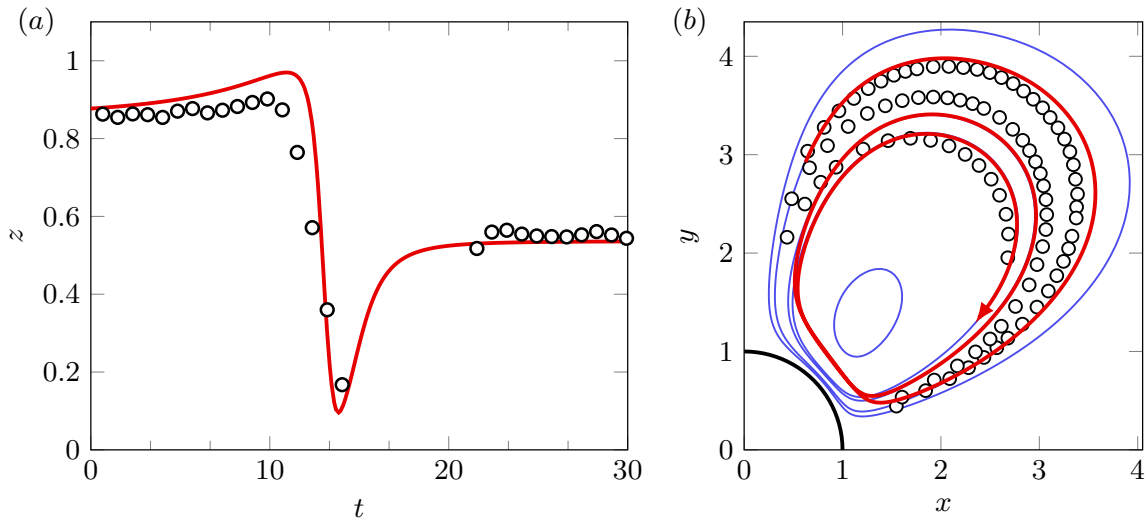

Figure 4.7 (a) Axial motion of a particle over short time scales in the vicinity of the bubble, predicted by the theory (solid line) and measured experimentally (markers). Note the large $O(1)$ axial excursion of the particle on the shortest time scales $\sim T_s$ as it passes close to the bubble, which ultimately results in a smaller net axial displacement Δz, informing the long-time 3D motion. (b) Projection of a part of a 3D particle trajectory in the xy-plane computed from $\boldsymbol{U}$ (red), showing the radial drift as a systematic spiraling deviating from the 2D periodic orbits (blue), with deviations concentrated at locations close to the bubble surface.

mentally measured azimuthal profile of the axial velocity component $U_z(\theta)$ near the bubble ($r \approx 1$), which determines the ratio c_{01}/c_{11}. This yields c_{01}, since $c_{11} \approx -1.41$ is given automatically by (4.19) and the theoretical $\boldsymbol{u}$, thereby fixing the shape of the flow. The value of $c_{01} \approx -0.34$ obtained by this procedure confirms that the axisymmetric component flow in the experiment (i) has the "fountain" orientation ($c_{01} < 0$) and (ii) is weaker than the planar component, with a magnitude that agrees well with the theoretical estimate (using damping coefficients) of $|c_{01}| \sim 0.32$ (cf. section 4.3). In order to non-dimensionalize the experimental times, we first extrapolate the experimentally measured velocity onto the bubble surface, which yields a maximum slip velocity u_{max} at the interface, which is then translated into an experimental oscillation amplitude ϵ using the prediction (from 2D theory) of $u_{max}/(\epsilon^2 a\omega) \approx 1.54$. The computed value of ϵ determines the time scale $T_s = 1/(\epsilon^2\omega)$, which is used to scale time in the experiments for a comparison with theory. It should be stressed that, therefore, all theoretical figures and computations in the present work (unless explicitly stated otherwise) directly use parameters employed in practical bubble microstreaming experiments: $d = 2.5, h = 6.25$ for the channel geometry, $a = 40\mu$m, $f = 20\,$kHz, and the appropriate c_{01} inferred above.

We show here that the experiment confirms the theoretical results on all three distinct time scales: (i) the fast time scale $\sim T_s$ of strong axial displacement, (ii) the intermediate time scale $\sim 10T_s - 100T_s$ of the approximately 2D vortex motion, and (iii) the very long time scale $\tau \sim 1000T_s$ involving the toroidal motion with systematic variation of the axial position of the particle, accompanied by a slow variation of the extent of the planar motion. Figure 4.7(a) demonstrates that the strong, fast displacements along the z-axis are temporally resolved in experiment and in very good agreement with the theoretical prediction, including the characteristic asymmetry between the positive and negative portions of the z-displacement motion, which ultimately leads to the drifts Δz. Figure 4.7(b) shows that the motion projected into the $x - y$ plane still reproduces the "typical" 2D fountain dynamics. Limitations in the experimental time resolution prevent us from verifying directly the predicted deviations of the projected 3D trajectories (red) near the bubble from the streamlines resulting from the 2D theory (blue). It is interesting to note, though, that the xy-projection of a tracer particle on such a trajectory shows a spiraling motion towards the 2D vortex center, an observation commonly made in cylinder streaming [50, 51] and ascribed to inertial forces on the particles (as supported by numerical computations, cf. [7]). Finally, figure 4.8 confirms that the pattern of motion over long time scales $\tau \sim 1000T_s$ is also modeled successfully: both the pattern of slow displacement along the z-axis as well as the pattern of widening and tightening radial extent of trajectories is confirmed in experiment, as is the strong correlation between the two motion patterns. Figure 4.8 thus allows for a quantitative verification of the toroidal motion pattern of figure 4.4(b).

Prior to these new APTV experiments, there has only been one report of three-dimensional boundary streaming flow, for a cylinder oscillated along a diameter [50], cf. figure 4.9(a). The patterns of streaming along the cylinder axis show significant differences to the bubble streaming, but it must be realized that even a strictly two-dimensional theory of cylinder streaming [5, 30, 113] reveals very different patterns from 2D bubble streaming. In particular, a "DC boundary layer" is typically present, i.e., every quadrant of the streaming flow in the xy-plane has two radially stacked vortices. Thanks to the general nature of our approach to describing 3D flows as a perturbation of the 2D patterns, however, it is possible to obtain a 3D solution for cylinder streaming as well. This is helped by the absence of axial oscillations of the (solid) cylinder, so that c_{01} is identically zero.

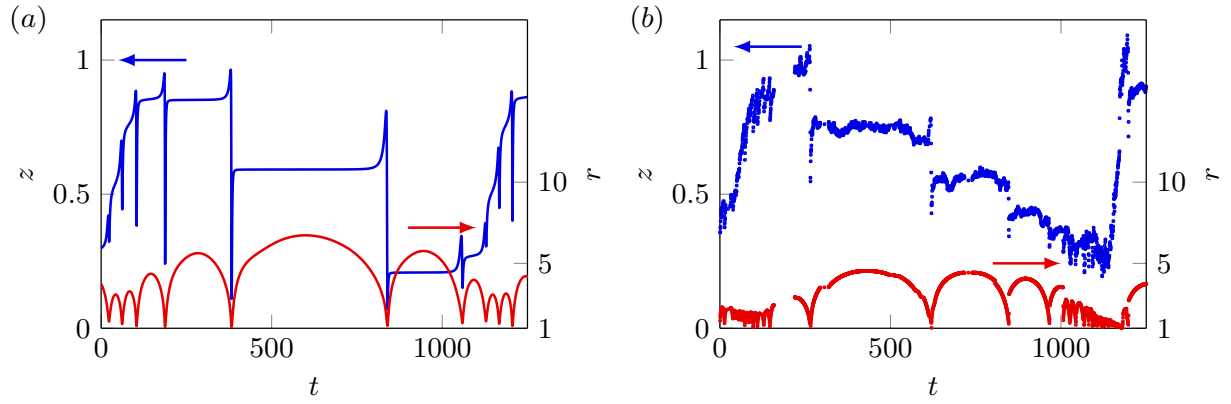

Figure 4.8 Axial and radial positions of a fluid element determined by numerical integration (a) and of an approximately passive tracer in experiment (b). Both show that the long-time three-dimensional motion is organized into simpler two-dimensional orbits (constant z). The slow axial motion is towards the wall $z = d/2$ on tight orbits (small maximum r in regions of constant z) and in the opposite direction for wide orbits (large maximum r in regions of constant z), quantitating the toroidal motion seen in figure 4.4(b).

The only flow mode c_{11} is determined again by 4.19, with $\boldsymbol{u}$ now representing the steady streaming flow outside the no-slip cylinder boundary layer, as given by an leading order expansion in powers of δ of the solution derived by Bertelsen et al. [5].

The qualitative experimental image of figure 4.9(a) from Lutz et al. [50] does not contain 3D information, but is a projection with finite depth of field showing multiple flow lines. Likewise, figure 4.9(b) shows characteristic flow lines projected onto the x-z plane (x being the axis of oscillation of the cylinder), the same plane as in figure 4.9(a). Streamlines point away from the bubble and towards the walls outside the nominal "DC boundary layer", whose radial extent is marked by the "box" outlines in the experimental and theoretical figures. Close to the mid-plane, the flow appears two-dimensional, with axial motion being restricted to regions close to the wall; these flow features are in qualitative agreement with the results of Lutz et al. [50] and demonstrate the wider applicability of our formalism to 3D streaming flows.

4.6 Conclusions

We have developed the first description of three-dimensional boundary streaming flow patterns by employing a perturbation approach to microbubble streaming of planar symmetry. We found that the requirement of no-slip boundary conditions at the top and bottom walls (where the axis of

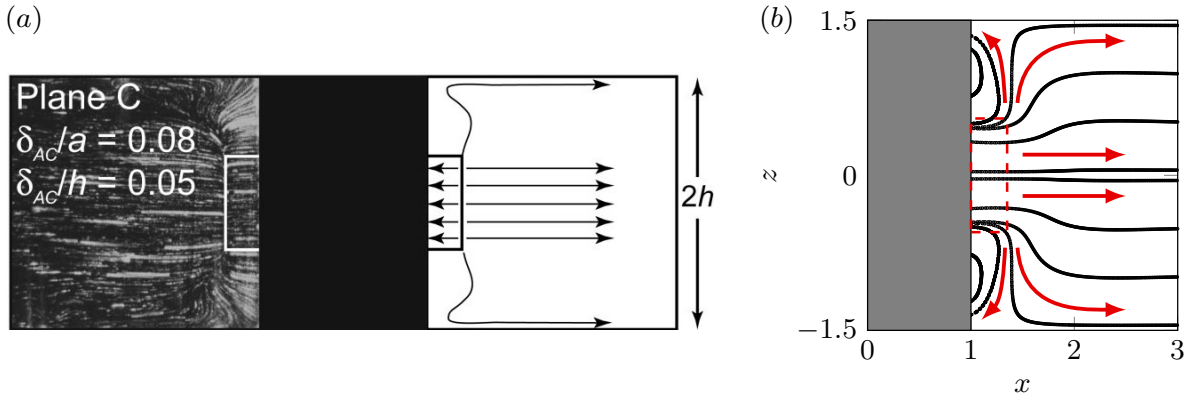

Figure 4.9 (a) Fluid trajectories under three-dimensional streaming due to an oscillating solid cylinder under axial confinement, projected in a plane containing the cylinder axis z and the axis of oscillation x. The right-hand part of the figure sketches the direction of motion of some tracer particles. From Lutz et al. [50]. (b) Analogous figure utilizing the present theory, showing qualitative agreement with the flow directions and the flow organization, including the "DC boundary layer" region indicated by boxed outlines in experiment and theory. The length of the cylinder axis relative to its radius in both the experimental image of Lutz et al. [50] and the present theory is $d = 3$.

the cylindrical bubble ends), as well as the presence of axial oscillations on the bubble surface, cause steady streaming modes that break the cylindrical symmetry, but do so in a very systematic fashion: Axisymmetric modes are excited by axial bubble oscillations, while higher azimuthal modes are excited to satisfy no-slip conditions at the top/bottom walls. These flow contributions modify the 2D trajectories in distinctive ways and on different time scales: While the flow remains 2D to very good approximation over times comparable to the orbit time of this idealized 2D motion, tracer particles experience (i) strong axial excursions over short time scales, when they are in the vicinity of the bubble surface, and (ii) systematic small radial and axial displacements over long times, which give rise to a longer-time periodicity of motion, in which the particles follow quasi-periodic orbits on a toroidal surface. All of these features are observed and confirmed in quantitative APTV experiments.

The long-time motion allows for an analytical description as a Hamiltonian flow in an abstract space, giving a reduced-order description of the flow in the spirit of a time-scale separation. The very general character of this approach should make it amenable to a large class of confined Stokes flow problems where the three-dimensionality of the confinement interferes with an original greater symmetry of the imposed flow. The formalism has shown its merits by comparison with streaming

from a solid cylinder.

The three-dimensional flow effects in bubble streaming discussed here have important implications for applications of this microstreaming technique. In micromixing set-ups using such bubbles [2, 44, 79, 112] the basic two-dimensional character of the flow makes it difficult to achieve strong (exponential) mixing, necessitating specific protocols of unsteadiness. The presence of axial flow components, in particular when it can be enhanced over the case presented here, should help achieve mixing more efficiently and quickly. In applications of particle sorting [105, 110, 111], selective displacement of particles by size is achieved close to the bubble over very short time scales – while the long-time motion of the 3D trajectories is of no concern in this case, the axial displacements of particles near the bubble need to be figured into the description of the sorting phenomenon. It could potentially be used to concentrate particles near the center of the channel, and thus assist a sorting of greater selectivity. For a much wider range of microfluidics set-ups, the tools developed here will be helpful to assess, model, and either minimize or enhance 3D flow effects that could be desirable or undesirable in numerous applications e.g. in the context of lab-on-a-chip, cell diagnostic, or microTAS devices.

Chapter 5

Systematic open flow mixing strategies using microbubble arrays

In the present chapter and the next, we focus on analyzing applications of microbubble streaming. In most practical microfluidics applications, it is important to maintain a continuous throughput of fluid in the channel (in addition to local flow actuation elements), usually implemented using a pressure-driven (Poiseuille) flow through the microchannel. We will therefore now place greater emphasis on superpositions of microbubble streaming and Poiseuille flow, the precise mathematical modeling of which is deferred to chapter 6.

In this chapter[1], we study the use of microbubble streaming for microfluidic mixing under a continuous throughput of fluid elements through the microchannel. We restrict our attention to two-dimensional advective mixing due to flows resulting from the superposition of a Poiseuille flow through the channel, and the streaming due to a microbubble array. Further, we consider only the advective mixing (stirring) properties of such flows, i.e. mixing in the absence of molecular diffusion.

We first show through a combination of numerical simulation and theory that mixing due to a steady superposition becomes ineffective beyond a characteristic time scale set by the stirring properties of vortical regions of the flow (arising due to the streaming), necessitating the introduction of unsteadiness. In this particular study, we generate unsteady (temporally modulated) flow fields, through a duty cycling of the streaming, while keeping the Poiseuille flow steady. Such unsteady flows achieve exponential mixing of the fluid (chaotic advection), with the rate of mixing dependent on the particular duty cycle chosen. We show using numerical simulation that the mixing rate is optimized for a particular duty cycle, i.e. a particular combination of times for which the streaming is turned "on" and "off", which can be understood using the *steady* properties of the streaming vortices and the Poiseuille flow. Finally, we estimate the maximum time for which advective mixing

[1]This chapter is adapted from Rallabandi et al. [79].

must be carried out (or equivalently the number of bubbles in the array) before the mixture is completely homogenized by diffusion.

5.1 Introduction

Fluid mixing is a crucial part of several natural and industrial processes, where it is often desirable to homogenize two species that are initially separate to aid a chemical reaction [35, 72, 96]. Mixing in general occurs as a combination of advection (stirring), which increases the surface area of contact between the two species by stretching and folding of fluid elements, and diffusion, which is ultimately responsible for homogenization at the molecular scale [63, 72, 107].

At macroscopic scales, fluid inertia allows the different species to continuously generate advective structures at small length scales (e.g. due to turbulence), which allows diffusion to quickly homogenize the mixture [69]. In most microfluidics applications however, fluid inertia is small, (low Reynolds numbers) making flows laminar [69, 100], while mixing by diffusion alone over typical channel sizes used in microfluidics is prohibitively long for most applications, usually requiring several seconds [34]. The focus of mixing studies at the microscale has therefore been on tailoring protocols of *stirring* the fluid in order to establish advective patterns at finer length scales, which are then rapidly homogenized by diffusion. Such optimal stirring protocols have been studied theoretically in a number of situations, focusing primarily on mixing in closed systems with zero throughput [63, 92].

For practical applications however, it is usually desirable to have a continuous throughput through the mixer, making microfluidic devices particularly attractive for micromixing. This is typically achieved by augmenting the transport flow through the channel with secondary cross flows that are actuated either by geometric features built into the construction of the device (passive) or by an external energy source (active) such as electrokinetics, dielectrophoresis or thermal currents [69, 71, 100]. In many cases, these cross flows are locally actuated, and therefore have decaying flow strength away from the actuator, resulting in vortical flow structures [69, 100].

The strength of the cross flow relative to the primary transport determines the topology of the resulting flow field, and thereby its mixing properties. Weakly excited flows only slightly modify the transport, resulting in flows that allow continuous transport of fluid elements through the device,

but require long mixing times and consequently large channel lengths. By contrast, stronger cross flows, while offering better mixing capabilities, confine the mixing to localized recirculation regions due to their vortical structure, preventing mixed fluid from being transported through the channel. This makes it necessary to actively modulate the secondary flow to achieve rapid mixing at a high throughput.

A protypical example of such a situation arises in the use of acoustically excited microbubbles, where applied acoustic energy (at ultrasound frequencies) is rectified into a powerful steady "streaming" flow. The ease of manufacture and actuation makes bubble-driven streaming particularly attractive for microfluidics, where they have been utilized for a variety of applications such as shear force actuation[55], particle trapping and focusing [105, 110, 111], size-sorting and fluid mixing [1, 44, 112]. While the effectiveness of microbubble streaming in mixing applications has been demonstrated experimentally in a number of configurations and geometries, previous studies [1, 2, 43] have (i) not systematically isolated the effect of molecular diffusion from the mixing due to advection alone, and (ii) have utilized only steady flow strategies, indicating a scope for much greater improvement by the use of flow modulation.

Here we present a systematic study of mixing due to the streaming driven by a periodic array of bubbles of semi-cylindrical shape with continuous transport. Using a combination of numerical simulation and the analytical streaming theory developed in chapter 3, we first quantify the stirring processes that occur within closed streamlines in the absence of diffusion, which will provide us with the length and time scales relevant to the generation of advective stirring patterns. We then demonstrate that the introduction of unsteadiness by means of duty cycling of the streaming results in (i) exponentially fast mixing, and (ii) allows for continuous transport of the mixed fluid through the device. Using simple physical and geometric arguments, we show that the mixing is optimized by a well-chosen duty cycle that depends only on the desired throughput and the channel geometry, providing general guidelines for the design of open flow micromixers utilizing secondary flows.

5.2 Set-up and methods

The geometry of the set-up considered here for open flow micromixing with a continuous throughput is illustrated in figure 5.1, indicating the location of bubbles (blue semicircular outlines) relative

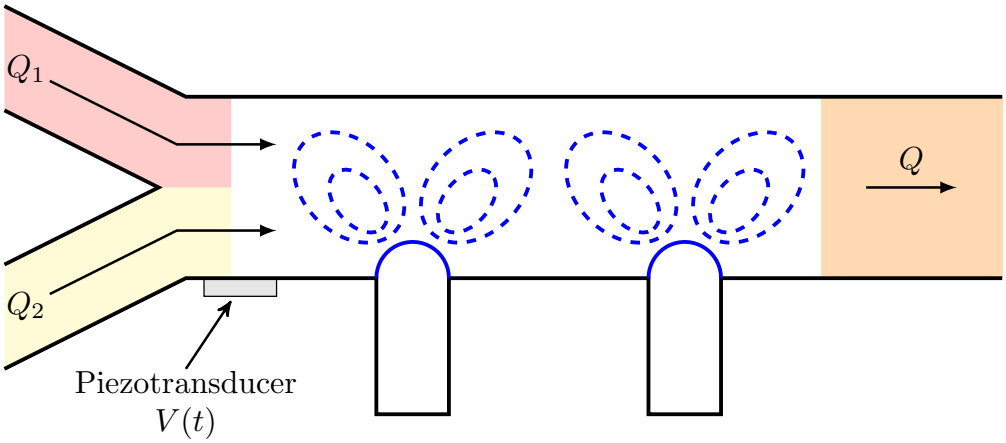

Figure 5.1 A typical bubble-based micromixer design, indicating (i) inlets through which initially unmixed fluid streams are introduced, and (ii) an array of acoustically excited microbubbles located in the main channel. The microbubble streaming may be temporally modulated by exciting the piezoelectric transducer with a time-dependent voltage amplitude $V(t)$. The resulting unsteady flows can achieve rapid mixing with net transport through the channel.

to the inlets and outlets of the microfluidic device. The bubbles are attached to a wall of the micro-channel by means of blind side-channel of width $2a$, which protrudes from the main channel. The geometry of the side-channel establishes a bubble of semi-cylindrical shape (semi-circular cross section). Figure 5.1 shows a cross section of the device geometry. Applied ultrasound at a frequency $f \sim 1 - 100$ kHz establishes oscillations of the interface with an characteristic amplitude ϵa, which, through a rectification of the acoustic energy, drives a secondary *steady* flow (streaming) with a characteristic speed $U_s = 2\pi\epsilon^2 af$. Due to the cylindrical symmetry of the bubble, the streaming is confined to cross-sectional planes perpendicular to the bubble axis (two-dimensional flow) [54, 77, 78, 109, 112] and is characterized by a symmetric pair of steady counter-rotating vortices, as shown in figure 5.1.

5.2.1 Flow field and mixing simulations

We are in general interested in the mixing properties of a transport flow through the channel (pressure-driven Poiseuille flow), augmented by a vortical flow (microbubble streaming). The Reynolds number associated with both the Poiseuille flow and steady streaming is typically small in microfluidics; this allows us to express the flow in general as a superposition of the two flow fields. For convenience, we non-dimensionalize lengths by the bubble radius a and velocities by the

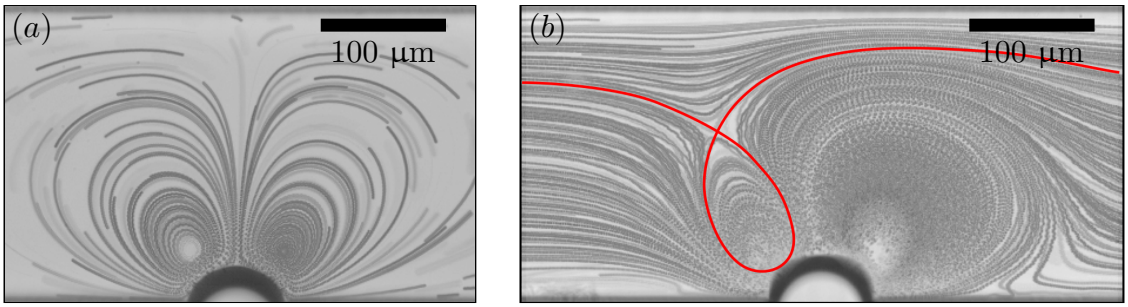

Figure 5.2 Streaklines of (a) bubble streaming only (fountain vortices) and (b) streaming with a net transport through the channel (left to right), showing the separatrix (red curve) between the upstream vortex and the open streamlines.

characterstic streaming speed U_s.

Due to the cylindrical bubble geometry, the streaming is to good approximation two dimensional in x-y planes perpendicular to the bubble axis. This has been shown both by direct experimental measurements [110] as well as by theoretical calculations [77, 112]. In a half-space ($h \equiv H/a \to \infty$), the streaming at any driving frequency is given by Rallabandi et al. [77] using an expansion into Stokes singularities, and is easily modified for a channel of finite height h, yielding a streaming velocity field $\boldsymbol{u}_s(x, y)$ (see chapter 3, [78, 105])[2]. While axial flow components may in general be present in bubble-driven streaming, a systematic axial recirculation of the fluid requires much longer times than the faster vortical motion in the xy plane, which allows us to safely ignore these effects as a first approximation [54, 78], see also chapter 4.

The pressure-driven transport flow through a rectangular channel of a given cross-section in the absence of the bubble is given by analytically by Mortensen et al. [66]. The bubble boundary conditions can be accounted for by a Stokes superposition similar to that used for the streaming (singularity expansion similarly modified to also satisfy boundary conditions at the bubble (no-stress, no-penetration) [105]. The modified transport flow is denoted by a dimensionless velocity field $\boldsymbol{u}_p$, which is defined so as to have unit mean velocity (in units of U_s) over the channel cross-section as $|x| \to \infty$, i.e.

$$\frac{1}{hd}\int_{-d/2}^{d/2}\int_{0}^{h} \boldsymbol{u}_p(x \to \infty, y, z)\,\mathrm{d}y\,\mathrm{d}z \equiv 1.$$

The modeling of the pressure-driven transport flow is described in greater detail in section 6.3.1 of

[2]In this chapter, $\boldsymbol{u}_s$ refers to the steady 2D Lagrangian streaming flow.

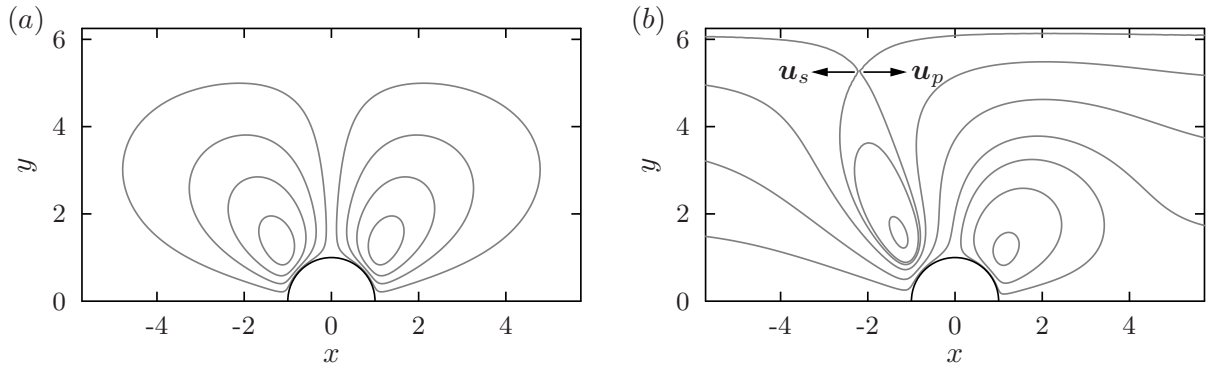

Figure 5.3 Streamline portraits of (a) bubble microstreaming only (fountain orientation), and (b) streaming with Poiseuille flow (flowing left to right) at $s = 0.015$, showing the presence of both upstream and downstream vortices. The hyperbolic stagnation point that forms a part of the upstream vortex is due to the cancellation of the streaming by the Poiseuille flow, indicated by arrows in (b).

chapter 6, where the trajectories of individual particles is more important.

The non-dimensional flow field resulting from the superposition of bubble streaming and transport may be written as

$$\boldsymbol{u}(\boldsymbol{x}) = \boldsymbol{u}_s + s\, u_{\max} \boldsymbol{u}_p.$$

where $u_{\max}$ is the maximum dimensionless streaming speed, which occurs at the bubble surface. The parameter s is therefore the ratio between the mean transport speed and the maximum streaming speed, a quantity that is directly relevant for the experimental characterization of the flow [105, 110, 111].

We restrict our attention to the two-dimensional mixing occurring in the mid-plane of the channel, i.e. the plane perpendicular to the the bubble axis that contains its mid-point ($z = 0$). The two-dimensional streaming flow is governed by a dimensionless steady stream function ψ (characteristic scale $U_s a$), defined by $\psi = \int u_x \, \mathrm{d}y = -\int u_y \, \mathrm{d}x$, which will prove useful in subsequent sections[3]. Of interest to the two-dimensional description is the ratio of the mean mid-plane speed (in the $z = 0$ plane) to the mean bulk speed of the entire channel cross-section, given by

$$\overline{u}_p \equiv \frac{1}{h} \int_0^h \hat{\boldsymbol{x}} \cdot \boldsymbol{u}_p(x \to \infty, y, z = 0) \, \mathrm{d}y.$$

For the channel aspect ratio considered here ($D/H = 0.4$), $\overline{u}_p \approx 1.48$.

[3] ψ in this chapter is the quantity called Ψ in chapter 3.

The mixing under a given flow field $\boldsymbol{u}(\boldsymbol{x},t)$ is quantified by the spatial structure of an temporally evolving scalar field $c(\boldsymbol{x},t)$ that describes the concentrations of the two species. A passively advected scalar field in general satisfies

$$\frac{\partial c}{\partial t} + (\boldsymbol{u}\cdot\boldsymbol{\nabla})c = \frac{1}{Pe}\nabla^2 c, \tag{5.1}$$

subject to some initial and boundary conditions on c. The Péclet number $Pe = U_s a/D_p = 6\pi\eta U_s a a_p/k_B T$ is typically large in experiments ($\sim 10^6$), so that it is appropriate to neglect the effect of diffusion and consider advective mixing (stirring) only. This will provide a lower bound on the mixing quality under the specified flow field, with any effect of diffusion only enhancing the quality of mixing.

The advection equation in general does not admit simple analytical solutions. Numerically, the limit $Pe \to \infty$ is difficult to analyze using grid based techniques due to the generation of arbitrarily fine length scales of the scalar field in the the absence of diffusion, which is precisely the feature of interest in advective stirring and must therefore be resolved accurately. To accurately solve (5.1) in this limit, we use a Lagrangian particle method, where we compute the advection of a large number of passive tracers under the flow, i.e. we solve $\dot{\boldsymbol{x}}(t) = \boldsymbol{u}(\boldsymbol{x}(t))$. Each of these tracers is identified with a value of the scalar field, which is advected with the particle (strictly true in the absence of diffusion). The scalar field is reconstructed at any instant of time by a linear interpolation of the values assigned to the particles onto a Cartesian grid. This technique is especially suited to the class of problems with negligible diffusion and has widely been employed in previous mixing studies [10, 25, 92].

We restrict our attention to an initial distribution of the scalar field characterized by two distinct layers of unmixed fluid separated by a sharp "interface" of contact, located initially at $y = y_0$. The initial distribution of the scalar field is therefore

$$c(\boldsymbol{x}, t=0) = c_0(\boldsymbol{x}) = \mathrm{H}(y_0 - y), \tag{5.2}$$

where $\mathrm{H}(z)$ is the Heaviside function. This is the most practical situation in experiments, where the initally unmixed fluids are introduced from the two different inlets, with y_0 determined by the ratio of flow rates through the two inlets.

For the purpose of modeling, we have assumed the absence of (i) diffusion, (ii) axial velocity components, and (iii) unsteady motion on fast timescales. It is worth remarking that the inclusion of one or more of these effects only *enhances* the mixing properties of the flow [100, 123]. One may therefore consider the results presented here as a theoretical lower bound on the mixing quality that may achieved in practice. In particular, any experimental realization of such a flow field is expected to have improved mixing properties for a given set of conditions – certainly for situations involving highly diffusive species.

5.2.2 Quantification of mixing effectiveness

The quality of mixing at an instant of time is related directly to the spatial distribution of the instantaneous scalar field $c(\boldsymbol{x}, t)$ that is passively advected by the flow. To quantify the quality of mixing, we use the mix-variance of c, which is a multi-scale mixing measure appropriate for two dimensional advection-dominated flows [59, 60, 92]. The mix-variance is denoted by $\Phi^2(c - \overline{c})$ and is defined on the unit square by

$$\Phi^2(c - \overline{c}) = \sum_{\substack{\boldsymbol{k} \\ |\boldsymbol{k}| \neq 0}} \Lambda_{\boldsymbol{k}} |c_{\boldsymbol{k}}|^2, \quad \text{where} \quad \Lambda_{\boldsymbol{k}} = \frac{1}{\sqrt{1 + (2\pi|\boldsymbol{k}|)^2}}. \tag{5.3}$$

The $c_{\boldsymbol{k}}$ are two-dimensional Fourier components of c, given by

$$c_{\boldsymbol{k}}(t) = \int_{\mathrm{ROI}} c(\boldsymbol{x'}, t)\, \mathrm{e}^{-\mathrm{i}2\pi \boldsymbol{k} \cdot \boldsymbol{x'}} \mathrm{d}\boldsymbol{x'}, \tag{5.4}$$

where $\boldsymbol{x'} = (x', y')$, with $x', y' \in [0, 1]$ within the region of interest (ROI). Here, $\overline{c}$ is the mean concentration field within the ROI (identically equal to $c_{\boldsymbol{k}=\boldsymbol{0}}$), and does not contribute to $\Phi^2(c - \overline{c})$. The mix-variance is a particularly useful mixing measure in the limit of small diffusion, since it penalizes the energies contained in shorter wavelengths by the weight factor $\Lambda_{\boldsymbol{k}}$ (lower values of Φ^2 indicate better mixing).

To compute the mix-variance in experiment, we normalize the measured grayscale fluorescent intensity by the intensities of the two liquid streams before they meet. The fluorescence intensities, denoted respectively as $C_{\max}$ and $C_{\min}$ for the bright (containing fluorescent nanoparticles) and dark streams, are the mean fluorescence intensities in representative areas contained within the two

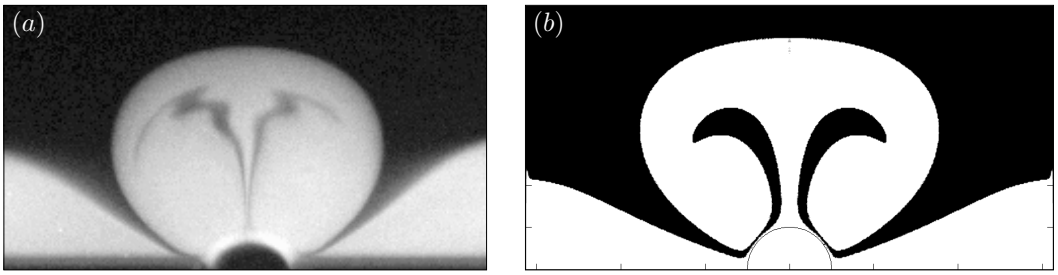

Figure 5.4 Scalar field after 60 ms (one core orbit time), (a) visualized experimentally using fluorescent 100 nm-diameter nanoparticles, and (b) computed numerically (cf. section 5.2.1) due to bubble streaming only (no Poiseuille flow) at 21.9 kHz.

streams before they meet. The normalized signal intensity is then defined as $c \equiv \dfrac{C - C_{\min}}{C_{\max} - C_{\min}}$, where C is the measured signal intensity at any point. Under this normalization, the bright and dark streams are identified in the unmixed state with $c = 1$ and $c = 0$ respectively. In both experiment and simulation, we select a square ROI whose side is equal to the channel height H, located just downstream of the bubble. To compute the mix-norm, we first rescale x and y by the dimensions of the ROI to be consistent with the definition of the mix-norm (5.3). The Fourier coefficients corresponding to each wave vector (computed by FFT) are used to calculate the mixing variance using (5.3).

We will focus on the case where the flow rates of unmixed liquids through the two inlets are equal, so that the mean concentration field is $\overline{c} = 0.5$, with the interface between the two phases occurring at $y = h/2$. It is also useful to rescale Φ^2 computed at any instant of time t by its value for the initial un-mixed configuration ($\Phi_0^2 \approx 0.0355$), to obtain a normalized mixing measure $\phi^2 = \Phi^2/\Phi_0^2$, which varies between 0 (fully mixed) and 1 (initial configuration).

5.3 Results and Discussion

5.3.1 Steady vortical mixing

Figures 5.2 and 5.3 show that the flow field in general consists of both upstream and downstream vortices. In order to utilize these regions effectively for mixing, it is useful to first analyze the mixing properties of a set of closed streamlines. As a representative prototype, we simply consider the two-dimensional steady streaming (fixed driving frequency and amplitude), in the absence of

net transport ($s = 0$). This will allow us to identify the time scales over which stirring by a steady 2D vortex (closed streamlines) is an effective mixing strategy, which will form the basis of understanding of the mixing in the more complex flow ($s > 0$) discussed in detail in the subsequent sections.

Due to the symmetry of problem for $s = 0$, we restrict our attention to $x > 0$, where the flow is characterized by a single system of closed streamlines centered around a vortex center, with the flow driven radially outward near $x = 0$ and radially inward near the wall at $y = 0$. The flow is described by the stream function $\psi \in [\psi_m, 0]$, where $\psi = \psi_m < 0$ is its value at the vortex center, and $\psi = 0$ corresponds to the largest streamline, coincident with the boundaries of the domain. In the absence of diffusion, the scalar field is only redistributed *along* each streamline by advection, with no transfer of material across streamlines. The concentration distribution along a streamline ψ is time periodic over the orbit time of a fluid element along that streamline $T(\psi)$, i.e.

$$c(\boldsymbol{x}, t) = c(\boldsymbol{x}, t + T(\psi)), \quad \text{on} \quad \psi = \psi(\boldsymbol{x}), \tag{5.5}$$

where $T(\psi) = \oint_\psi \mathrm{d}s/|\boldsymbol{u}|$ and $\mathrm{d}s$ is an arc length element along a streamline.

For the initial distribution c_0 given by (5.2), one may identify a streamline $\psi = \psi_c$ tangent to the interface between the two fluids, located initially at $y = y_0$. The volume enclosed by this streamline ($\psi_c < \psi < \psi_c$) therefore remains unmixed, with spatial redistribution of the scalar field restricted to $\psi_c < \psi < 0$. The concentration field along $\psi = \psi_c$ is uniform except at the single point at which it is tangent to the interface. This tangent point on the interface orbits the vortex center over a time $T_c \equiv T(\psi_c)$, stretching the points on the interface in its neighborhood with it. On the other hand, there is relatively little change in the concentration field along large streamlines ($\psi \sim 0$) over this time scale, due to slower mean flow. This results in the generation of a pair of striations over a characteristic timescale given by T_c.

At long times ($t \gg T_c$) the vortex stirring results in a well-defined unmixed "core", delineated by ψ_c, surrounded by alternating bands of bright and dark fluid, which in general become thinner with time. The spatial distribution of c at some t is non-trivial, but the characteristic striation thickness typically increases away from the bubble (and towards the walls) due to the decay of the flow and its gradients away from the bubble.

The mixing properties of such a steady vortical flow may be described quantitatively by means of a simple model that considers thin striations distributed around an unmixed core. For the remainder of this subsection, we will take all length scales to be scaled by the dimensions of the ROI, so that (5.3) may be directly applied to compute Φ^2. We assume that the core is defined in x' and y' directions respectively by dimensionless lengths x'_0 and y'_0, and that striations are similarly characterized by dimensionless striation thicknesses δ'_x and δ'_y respectively. In general, for steady flow x'_0 and y'_0 are constants dependent on the initial conditions only, whereas δ'_x and δ'_y are in general time-dependent. In units of the dimensions of the ROI (and dropping primes for convenience), we model the concentration field as

$$c(\boldsymbol{x}) = \sum_{j=0}^{m} (-1)^j c^j(\boldsymbol{x}), \tag{5.6}$$

where

$$c^j(\boldsymbol{x}) = \begin{cases} 1, & x < x_0 + j\delta_x \quad \text{and} \quad y < y_0 + j\delta_y \\ 0, & \text{otherwise,} \end{cases} \tag{5.7}$$

and m represents the total number of striations within the ROI. The scalar field due to (5.6) is given in figure 5.5(a), and showing characteristic core and striation length scales.

The Fourier component $c_{\boldsymbol{k}}$, corresponding to $\boldsymbol{k} = (k_x, k_y)$ is computed using (5.6) and (5.7) and has the analytical form

$$c_{\boldsymbol{k}} = -\frac{1}{4\pi^2 k_x k_y}\Big(S_m(\boldsymbol{k}\cdot\boldsymbol{x}_0, \boldsymbol{k}\cdot\boldsymbol{\delta}) + S_m(0,0) - S_m(k_x x_0, k_x\delta_x) - S_m(k_y y_0, k_y\delta_y)\Big), \tag{5.8}$$

where $\boldsymbol{x}_0 \equiv (x_0, y_0)$, $\boldsymbol{\delta} \equiv (\delta_x, \delta_y)$, and

$$S_m(p,q) \equiv \sum_{j=0}^{m} (-1)^j \mathrm{e}^{-2\pi\mathrm{i}(p+jq)} = \mathrm{e}^{-2\pi\mathrm{i}p}\frac{1 + (-1)^m \mathrm{e}^{-2\pi\mathrm{i}(m+1)q}}{1 + \mathrm{e}^{-2\pi\mathrm{i}q}} \tag{5.9}$$

for some scalars p and q. The expression for $c_{\boldsymbol{k}}$ for $k_i = 0$ (where $k_i \in \{k_x, k_y\}$) is given by the L'Hôspital limit of (5.8) as $k_i \to 0$. The mix-variance of the model concentration field is computed using (5.3) and (5.8), with the approximation $\Lambda_{\boldsymbol{k}} \approx 1/2\pi|\boldsymbol{k}|$, since the computation of Φ^2 involves only $|\boldsymbol{k}| \geq 1$.

At long times ($t \gg T_c$), the striations are thin and large in number, populating the entire region outside the unmixed core, i.e. $|\boldsymbol{\delta}| \ll 1$ and $m \approx (1-x_0)/\delta_x \approx (1-y_0)/\delta_y \gg 1$. While the mix-variance in principle involves features over the entire spectrum of length scales, the $c_{\boldsymbol{k}}$ given by (5.8) is dominated by two groups of wave-vectors $\boldsymbol{k}$: (i) those for which $|\boldsymbol{k}| = O(1)$, characterizing large scale features such as the unmixed core, and (ii) those for which $|2\boldsymbol{k}\cdot\boldsymbol{\delta}| = O(1)$, corresponding to the striation thickness.

For $|\boldsymbol{k}| = O(1)$, $c_{\boldsymbol{k}}$ may be approximated by an expansion of (5.9) and (5.8) in the limit $\boldsymbol{k}\cdot\boldsymbol{\delta} \ll 1$. To leading order in $|\boldsymbol{k}\cdot\boldsymbol{\delta}|$, we have

$$c_{\boldsymbol{k}} \approx -\frac{\mathrm{e}^{-\pi \mathrm{i}\,\boldsymbol{k}\cdot\boldsymbol{\delta}}}{2\pi^2 k_x k_y}\,\sin\pi k_x x_0\,\sin\pi k_y y_0 \quad \text{for} \quad |\boldsymbol{k}| = O(1). \tag{5.10}$$

Considering only the lowest modes, i.e. $\boldsymbol{k}$ whose components $k_i \in \{-1,0,1\}$, the contribution of (5.10) to the mix-norm according to (5.3) is

$$\Phi_c^2 = \frac{1}{4\pi^3}\left(y_0^2\sin^2\pi x_0 + x_0^2\sin^2\pi y_0 + \frac{\sqrt{2}}{\pi^2}\sin^2\pi x_0\sin^2\pi y_0\right). \tag{5.11}$$

Note that (5.11) involves only the core size and is independent of the striation thickness, and is therefore constant in time.

We now similarly compute the contribution of higher modes – those that characterize the striation structure – to the mix-variance, corresponding to $|\boldsymbol{k}\cdot\boldsymbol{\delta}| \approx 1/2$. To compute Φ^2 due to these modes, we neglect $\boldsymbol{k}$ for which *both* components are $O(|\boldsymbol{\delta}|^{-1}|)$, and consider only those cases for which which the component with smaller magnitude (denoted by $k_{\min}$) is $O(1)$, which sets the size of the larger component (denoted by $k_{\max}$). This is a reasonable first approximation, since the mix-variance is dominated by the largest length scales, cf. (5.3), so that the contribution of modes where $k_x \sim k_y \sim O(|\boldsymbol{\delta}|^{-1}|)$ is subdominant to those modes where only either one of k_x or k_y is $O(|\boldsymbol{\delta}|^{-1}|)$.

In the limit $\boldsymbol{k}\cdot\boldsymbol{\delta}\to\pm 1/2$, we then have

$$c_{\boldsymbol{k}}\approx\begin{cases}\dfrac{(-1)^m}{4\pi^2k_xk_y}\left(\dfrac{\mathrm{e}^{-2\pi\mathrm{i}k_x(1+\delta_x)}-\mathrm{e}^{-2\pi\mathrm{i}k_xx_0}}{1-\mathrm{e}^{-2\pi\mathrm{i}k_x\delta_x}}+m+1\right), & k_x=O(1), \quad (5.12a)\\ \dfrac{(-1)^m}{4\pi^2k_xk_y}\left(\dfrac{\mathrm{e}^{-2\pi\mathrm{i}k_y(1+\delta_y)}-\mathrm{e}^{-2\pi\mathrm{i}k_yy_0}}{1-\mathrm{e}^{-2\pi\mathrm{i}k_y\delta_y}}+m+1\right), & k_y=O(1) \quad (5.12b)\end{cases}$$

We again restrict the computation of Φ^2 to situations where $k_{\min}\in\{-1,0,1\}$. Let us first consider the case where both components are non-negative ($k_i\geq 0$), and $k_{\min}=k_x=O(1)$. The components k_y relevant to (5.12a) is then given by solving (i) $k_y\delta_y=1/2$ and (ii) $\boldsymbol{k}\cdot\boldsymbol{\delta}=1/2$, which admit in general real valued solutions $k_y^{(1)}=1/(2\delta_y)$ and $k_y^{(2)}=k_y^{(1)}-k_x\delta_x/\delta_y$ respectively. Since the computation of Φ^2 involves only integer components of $\boldsymbol{k}$, we may replace k_y in (5.12a) by the two nearest integers to $k_y^{(j)}$, i.e. $\lfloor k_y^{(j)}\rfloor$ and $\lceil k_y^{(j)}\rceil$ (where $j\in\{1,2\}$). The equation (5.12a) may be applied to all distinct wave vectors $\boldsymbol{k}=(k_x,k_y)$ obtained by this procedure. For $k_x=0$, we have $k_y^{(1)}=k_y^{(2)}$, which results in two distinct wave-vectors $(0,\lfloor k_y^{(1)}\rfloor)$ and $(0,\lceil k_y^{(1)}\rceil)$. If $k_x=1$ and $\delta_x/\delta_y=O(1)$, we nominally have $\lceil k_y^{(2)}\rceil=\lfloor k_y^{(1)}\rfloor$, so that procedure results in *three* distinct wave-vectors $(1,\lfloor k_y^{(2)}\rfloor)$, $(1,\lfloor k_y^{(1)}\rfloor)$ and $(1,\lceil k_y^{(1)}\rceil)$. By the symmetry of (5.12), these arguments apply directly to cases with negative k_i and those where $k_{\min}=k_y=O(1)$.

To leading order in $|\boldsymbol{\delta}|$, the mix-norm due to (5.12) is

$$\begin{aligned}\Phi_s^2=&\frac{1}{\pi^3}\Bigg\{\delta_x(1-x_0)^2\left((1+y_0)^2+\frac{3}{\pi^2}\left(1+\frac{\sin 2\pi y_0}{2\pi(1-y_0)}\right)^2+\frac{3\sin^4\pi y_0}{\pi^4(1-y_0)^2}\right)\\&+\delta_y(1-y_0)^2\left((1+x_0)^2+\frac{3}{\pi^2}\left(1+\frac{\sin 2\pi x_0}{2\pi(1-x_0)}\right)^2+\frac{3\sin^4\pi x_0}{\pi^4(1-x_0)^2}\right)\Bigg\}. \quad (5.13)\end{aligned}$$

Equation (5.13) describes the contribution of the striations to the mix-norm, and is proportional to the striation thicknesses δ_x and δ_y in the two directions. Since a new pair of striations is generated for each orbit of the fluid around the core, the total number of striations in the flow is at any time t is given approximately by $2\times t/T_c$. Due to the spatial confinement, it is appropriate to assume that the characteristic striation thickness is proportional to the reciprocal of the number of striations. For simplicity, we assume symmetry between x and y, i.e. $x_0=y_0$, and $\delta_x=\delta_y=\alpha T_c/(2t)$, where

α is an $O(1)$ parameter that depends on the flow field. We then have

$$\Phi_c^2 = \frac{1}{4\pi^3}\left(2y_0^2\sin^2\pi y_0 + \frac{\sqrt{2}}{\pi^2}\sin^4\pi y_0\right), \quad \text{and} \tag{5.14}$$

$$\Phi_s^2 = \frac{T_c}{t}\Gamma_s^2 \tag{5.15}$$

where

$$\Gamma_s^2 \equiv \frac{\alpha}{\pi^3}\left(\left(1-y_0^2\right)^2 + \frac{3}{\pi^4}\sin^4\pi y_0 + \frac{3}{\pi^2}\left(1-y_0+\frac{\sin 2\pi y_0}{2\pi}\right)^2\right) \tag{5.16}$$

The mix-variance due to the entire spectrum of wave vectors, valid for $t \gg T_c$, is simply the superposition of the two contributions

$$\Phi^2_{t\gg T_c} = \Phi_c^2 + \Phi_s^2 \tag{5.17}$$

The model of the advection field and the resulting expressions for Φ^2 are not strictly applicable for times shorter than a core orbit time ($t < T_c$), for which no unmixed core has been yet established. The behavior of the mix-norm in the short time limit $t \ll T_c$ may be approximated in general using an expansion about its initial value Φ_0^2, i.e.

$$\Phi^2_{t\ll T_c} = \Phi_0^2\left(1-\beta_c\frac{t}{T_c}\right) + O(t^2), \tag{5.18}$$

where β_c depends on the details of the advection field. The time t^* at which the long time algebraic decay of Φ^2 becomes dominant may be estimated by the point at which the line $\Phi^2_{t\ll T_c}$ is tangent to the curve $\Phi^2_{t\gg T_c}$, which yields

$$\frac{t^*}{T_c} = \frac{2\gamma_s^2}{1-\phi_c^2}, \quad \text{and} \quad \beta_c = \frac{(1-\phi_c^2)^2}{4\gamma_s^2}, \tag{5.19}$$

where $\gamma_s^2 \equiv \Gamma_s^2/\Phi_0^2$ and $\phi_c^2 \equiv \Phi_c^2/\Phi_0^2$. It is useful to then rewrite the mixing behavior as

$$\phi^2(t) \equiv \frac{\Phi^2(t)}{\Phi_0^2} \approx \begin{cases} 1 - \dfrac{1-\phi_c^2}{2}\dfrac{t}{t^*}, & t \le t^* \\ \phi_c^2 + \dfrac{1-\phi_c^2}{2}\dfrac{t^*}{t}, & t \ge t^* \end{cases} \tag{5.20}$$

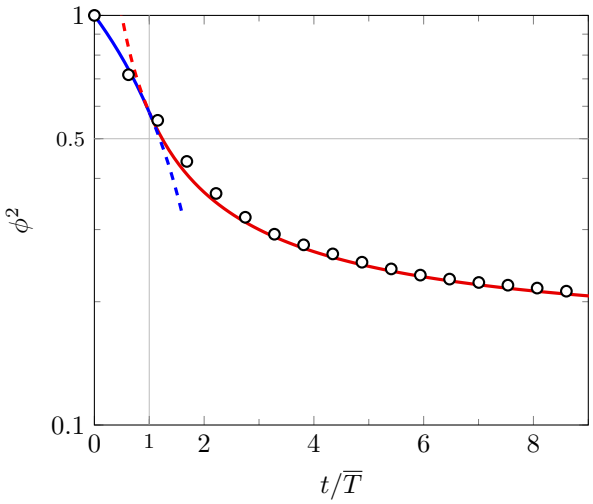

Figure 5.5 Decay of the normalized mix-variance ϕ^2 as a function of dimensionless time $t/\overline{T}$ due to a steady vortex, computed by simulations (markers) and predicted by the analytical model (lines). The blue and red lines indicate respectively the short and long time behaviors, showing a transition around $t/\overline{T} = 1$ corresponding to $\phi^2 \gtrsim 0.5$, according to (5.19).

The steady vortex mixes efficiently for times $t \leq t^*$, setting the maximum time for which the steady vortex is effective. In order to optimally utilize the vortex, one must therefore stir for a time $t \approx t^*$, corresponding to a mixing given by $\phi^2(t^*) = (1 - \phi_c^2)/2$, a quantity which varies between 1/2 (best case; $\phi_c \to 0$) and 1 (no mixing; $\phi_c \to 1$). Note that (5.20) is a general approximate expression that arises simply from a matching between a short time linear behavior and a long time algebraic t^{-1} behavior of Φ^2, and is independent of the precise details of the flow field.

It is useful to briefly also consider relevant stirring timescales, in particular for initial conditions involving an arbitrary distribution of striations throughout the volume enclosed by the vortex, where it is not possible to identify an unmixed core. The smallest characteristic time over which new striations are generated by a vortex is nominally given by the orbit time of closed streamlines that are arbitrarily close to the vortex center (vanishing enclosed areas). This does not however involve any large scale turnover of the volume of fluid enclosed by the vortex, and it therefore ultimately not a useful timescale to characterize the generation of new striations. A more relevant turnover time scale for a given vortex may be defined formally as

$$\overline{T} = \frac{a}{U_s} \frac{\int \oint_\psi \mathrm{d}l \, \mathrm{d}n}{\int |\boldsymbol{u}| \mathrm{d}n}, \tag{5.21}$$

where l and n are respectively coordinates tangential and normal to streamlines, and the limits of integration on n are given by the spatial extent of the vortex. Note that $\overline{T}$ is identically the ratio between the enclosed area and total areal flow rate in the vortex, and sets the characteristic time over which stirring occurs. For much shorter times, only a small fraction of the fluid in the vortex is stirred, while longer times result only in a small improvement in the mixing due to the algebraic t^{-1} refinement of the scalar field. We may therefore infer that $\overline{T} \sim t^*$ in the more general case of steady vortical mixing not involving unmixed regions of the flow.

An algebraic stretching of fluid elements (indicated by an algebraic decay of Φ^2) is typically considered to be "poorly mixing"[102]. Rather, *exponential* mixing (an exponential stretching and folding of fluid elements) is desired in most practical mixing applications, which is characterized by an exponential decay of Φ^2 at long times [42, 59, 60, 64].

Equation (5.20) shows that while mixing due to steady vortical stirring in 2D is promising at short times, its utility at long times is in general limited by its algebraic t^{-1} mixing properties, reflected in asymptotic behavior of Φ^2. It is well known as a consequence the Poincaré–Bendixson theorem that a two-dimensional steady flow cannot result in chaotic motion of fluid elements [117], and is therefore limited in its asymptotic(long-time) mixing properties. We have formally shown here that the long time mixing behavior of a steady 2D vortex becomes dominant for $t \gtrsim t^* \approx \overline{T}$, which is nominally the time beyond which the steady flow must be disrupted for any possible improvement in the mixing quality. It is important to remark that while we have considered the streaming in the absence of transport, such an analysis remains applicable to any vortical regions that may appear even in the presence of a finite transport flow.

5.3.2 Steady transport with streaming

We now consider the practically relevant situation, namely one with finite throughput, where the secondary streaming is superposed onto a primary transport flow through the device. Far away from the bubble, the transport is dominant (velocity scale $\overline{u}_p$) and the flow is approximately parallel to the channel axis, whereas the streaming (characteristic speed U_s) is dominant close to the bubble. Since the secondary flow is actuated locally, it becomes comparable to the transport flow speed $\overline{u}_p$ at a certain distance from the bubble. If the streaming is sufficiently strong, this occurs close

to the opposite wall $y = h$, resulting in a flow with both upstream and a downstream vortices, see figure 5.3(b). In particular, upstream of the bubble ($x < 0$), the streaming and transport flow fields compensate each other, resulting in a hyperbolic stagnation point in the flow, which lies on a separating streamline that distinguishes the upstream vortex from open streamlines in the flow.

It is generally desirable to drive the secondary flows as strongly as possible, which not only ensures greater flow speeds, but also that a greater fraction of the channel is occupied by the upstream and downstream vortices. The largest linear dimensions of either the upstream or the downstream vortex is on the order of the channel height H. Since these vortices are closed structures enclosing a finite volume, their mixing properties are qualitatively similar to the vortex mixing in the absence of transport, discussed in section 5.3.1. In particular, they behave as efficient mixers at short times, and are limited at long times by their algebraic mixing behavior. For strong streaming (small s), most of the flow in open streamlines is squeezed through a narrow gap of width $d_{gap} \approx sH$ between the bubble surface and the upstream vortex [105, 110, 111]. While advective mixing due to open streamlines is typically small compared over time scales relevant to vortical stirring, the gap flow may play an important role in diffusive mixing, as we will show in later sections.

Purely advective open flow mixing however, under the superposition of steady transport and vortical flows, is generally poor. Vortical stirring is only effective at short times $t \lesssim \overline{T}$, and any mixed fluid in these regions is never transported downstream due to the flow topology. Regions of the flow with open streamlines on the other hand are similar to flows with weakly excited secondary flows and are only effective over long transport times and channel lengths. It is therefore critical that the flow be modulated in order to effectively utilize both closed and open regions of the flow effectively.

5.3.3 Flow modulation by duty cycling

The limitations on fluid mixing by the use of steady flows can be overcome by the deliberate introduction of unsteadiness. A practical flow modulation strategy at constant throughput is through a duty cycling of the streaming, keeping the transport flow steady. Experimentally, this may be achieved simply by alternately turning on and off the ultrasound for time intervals τ_{on} and τ_{off} respectively. If the frequency of the modulation is much longer than that of the ultrasound

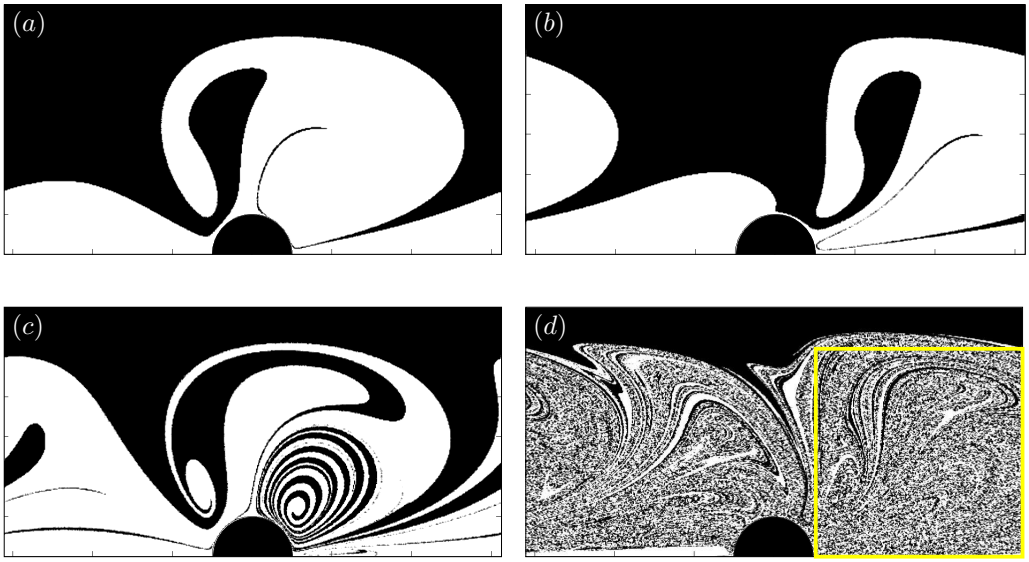

Figure 5.6 Snapshots of the scalar field mixing due to a duty cycle with $\tau_{\text{on}} = \tau_{\text{off}} = \overline{\tau}_p$, at different instants of time: (a) at the end of the first "on" half-cycle $t = \tau_{\text{on}}$, (b) at the end of the first cycle $t = \tau_{\text{cycle}}$, (c) at the end of the second "on" half-cycle, $t = \tau_{\text{cycle}} + \tau_{\text{on}}$, and (d) after 8 cycles, $t = 8\tau_{\text{cycle}}$. The region of interest (ROI) used to compute Φ^2 is indicated as a yellow square in (d).

$(\tau_{\text{on}}, \tau_{\text{off}} \gg 1/f)$, transients during the on/off process may be neglected. The flow may therefore be modeled as being time-periodic with period $\tau_{\text{cycle}} = \tau_{\text{on}} + \tau_{\text{off}}$, with a combination of the Poiseuille flow and the streaming in the "on" part of the cycle $(0 < t < \tau_{\text{on}})$, and with Poiseuille flow during the "off" phase $(\tau_{\text{on}} < t < \tau_{\text{cycle}})$. For mixing simulations, we use the time-periodic flow field $\boldsymbol{u}$ given by

$$\boldsymbol{u} = \begin{cases} s\, u_{\max}\, \boldsymbol{u}_p + \boldsymbol{u}_s, & 0 < t < \tau_{\text{on}}, \\ s\, u_{\max}\, \boldsymbol{u}_p, & \tau_{\text{on}} < t < \tau_{\text{cycle}}, \end{cases} \tag{5.22}$$

where it is understood that t is modulo τ_{cycle}.

Mixing during the "on" phase of the cycle is similar to the situation in section 5.3.2, occurring primarily in the closed upstream and downstream vortices of the flow. In addition, some advective structures are transported by open streamlines through the thin gap between the bubble and the upstream vortex. During the "off" phase, these mixed regions of fluid are transported downstream by the Poiseuille flow, presenting a rearranged advection field to the next "on" phase of the cycle. During the "off" part of the cycle, new relatively unmixed fluid therefore enters the region that, during the "on" part of the cycle, is taken up by the streaming vortices, which quickly stretch the fluid into thin bands. This rearrangement of the advection field introduces three important effects that make it

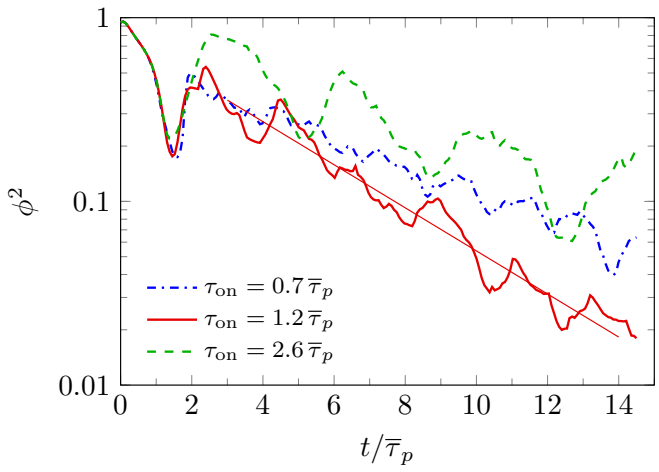

Figure 5.7 Normalized mix-variance as a function of time for three different duty cycles with $\tau_{\text{off}} = \overline{\tau}_p$ and varying τ_{on}, computed numerically for a periodic array of bubbles arranged in the channel as indicated in figure 5.1. The thin straight line indicates an exponential fit to the thick red curve.

particularly advantageous over steady vortical mixing. First, it disrupts any unmixed regions that may present, so that at long times (several cycles), effectively the entire volume of the channel is subjected to stretching and folding by the flow. Second, it shifts the locations of striations relative to the vortices, which enhance the mixing properties of the flow beyond the algebraic t^{-1} mixing that is achieved by steady vortices alone. And finally, the duty cycling disrupts the material separatrix between open and closed streamlines that exist during the "on" phase, allowing a net transport of the stirred fluid through the device, an important consideration for microfluidics applications.

In a periodic bubble array, a given volume of fluid is deformed repeatedly during each cycle. Figure 5.7 shows that the mix-variance indeed decays *exponentially* with time in a simulation that uses a periodic bubble array, with the rate of decay depending on the particular duty cycle chosen. In general, on time scales greater than the cycle time, the mix-variance oscillates about a mean exponential trend of the form

$$\phi^2_{\text{duty}}(t) \equiv \frac{\Phi^2_{\text{duty}}(t)}{\Phi^2_0} = C\,\mathrm{e}^{-\sigma t/\tau_{\text{cycle}}}, \quad \text{for} \quad t \gg \tau_{\text{cycle}}. \tag{5.23}$$

Here $C(\tau_{\text{on}}, \tau_{\text{off}})$ and $\sigma(\tau_{\text{on}}, \tau_{\text{off}})$ are respectively an $O(1)$ prefactor and an exponential rate constant that depend on the duty cycle, and are obtained by a least squares fit to the result of the simulation. Due to the exponential decay behavior of ϕ^2, it is worth identifying optimum duty cycling protocols.

It is useful to separately consider at least two separate kinds of optimum duty cycles.

The first involves identifying the duty cycle that maximizes the the mixing incurred *per cycle*, which is equivalent to maximizing σ. This in effect minimizes the number of cycles – and therefore the number of bubbles – required to achieve a target mixing quality, irrespective of the absolute cycle time required. The second kind of the optimization attempts to achieve the fastest decay of Φ^2 per unit of time, which involves a maximization of the quantity $\sigma/\tau_{\text{cycle}}$ without restricting the number of cycles (equivalently the number of bubbles in the array) required to achieve a targeted quality of mixing. Figure 5.8 shows that both of these optimization criteria result in different optimum duty cycles.

In order to understand these optimum duty cycles and the decay of Φ^2 that are achieved in either case, it is useful to interpret the action of the flow on a material fluid volume as a 2D mapping; each mapping results in some decay of the mix-variance Φ^2, which occurs over the time required to physically realize the map. The duty cycling allows the mapping to be repeatedly applied to the material volume, as it is transported past the bubble array. As a first approximation, it is reasonable to assume that the stirring is dominated by the upstream and downstream vortices during the "on" cycle, with relatively little mixing occurring within open regions of the flow. The mixing due to these steady vortices has already been discussed in Section 5.3.1, while the "off" cycle (open streamlines only) may be interpreted as involving primarily a translation of the mixed fluid (neglecting any effects of shear).

Under this simplistic picture of the deformation field, the role of the "off" cycle is simply to transport fluid from one vortex to another, in particular between the upstream and downstream vortices driven by a bubble. This allows a given material volume of the fluid to be nominally stirred twice per bubble – once by each vortex – improving the mixing quality over the case of steady flow. Maximum mixing efficiency may be expected when τ_{off} is chosen in order to allow optimum transport of fluid between the two vortices. The geometry of the flow is typically insensitive for a wide range of driving frequencies, as shown both by theory and experiment [77, 112]. In particular, the distance between vortex centers d_{vc} is reliably obtained from the asymptotic theory as $d_{vc} \approx 2.5a$. The mean

time for fluid to be transported between these vortices by the Poiseuille flow is therefore

$$\overline{\tau}_p = \frac{d_{vc}}{\overline{U}_p}, \tag{5.24}$$

where $\overline{U}_p \equiv U_s \times s u_{\max} \overline{u}_p$ is the mean (dimensional) Poiseuille flow speed in the $z = 0$ plane. The τ_{off} that allows optimal transport of fluid between vortices during the "off" part of the cycle, so that it may be taken up effectively stirred during the "on" part of the cycle is therefore $\tau_{\text{off}} \approx \overline{\tau}_p$. If τ_{off} is much smaller, the liquid distribution changes little between driving cycles. On the other hand, if τ_{off} is much larger, unmixed fluid flows past one (or both) of the vortices without being mixed.

At sufficiently long times, the duty cycling establishes a distribution of advective structures throughout the volume occupied by vortical regions of the flow. The τ_{on} that best utilizes the "on" part of the cycle is therefore on the order of the larger of the mean turnover times of the upstream and downstream vortices computed using (5.21). For the typical "fountain" orientation of streaming vortices, this optimum "on" time is set by the turnover time of the upstream vortex, denoted by $\overline{T}_{us}$. For $\tau_{\text{on}} < \overline{T}_{us}$, one or both of the vortices are not optimally used for mixing. On the other hand, $\tau_{\text{on}} > \overline{T}_{us}$ allows a greater volume of relatively unmixed fluid to be transported past the vortices by open streamlines, while achieving only a slight improvement in vortical stirring (due to the algebraic decay of Φ^2) resulting in poorer overall mixing.

The total flow rate in the upstream vortex is obtained directly from the range of stream function values spanned by it, and its enclosed area estimated by $a \times (H - a)$, which may be used to approximate $\overline{T}_{us}$ defined in (5.21). The optimum "on" time for small s may be written as

$$\overline{T}_{us} \approx \frac{a(h-1)}{U_s |\psi_m - s u_{\max} \overline{u}_p h|}, \tag{5.25}$$

where ψ_m is the value of the stream function at the upstream vortex center. For the parameters used here, we find that $\overline{T}_{us}/\overline{\tau}_p \equiv \mu \approx 1.87$. The duty cycle $\tau_{\text{on}} = \overline{T}_{\text{us}}$ and $\tau_{\text{off}} = \overline{\tau}_p$ results in the optimal use of vortices as well as the transport of fluid between them. It is worth emphasizing that this does not guarantee the fastest absolute decay of Φ^2 in time, but rather, the best mixing that may be achieved *per cycle*, i.e. it maximizes σ in (5.23). To estimate the maximum σ, we recall our results on steady vortical mixing (5.20), which predicts a reduction of Φ^2 by a factor of $(1 - \phi_c^2)/2$,

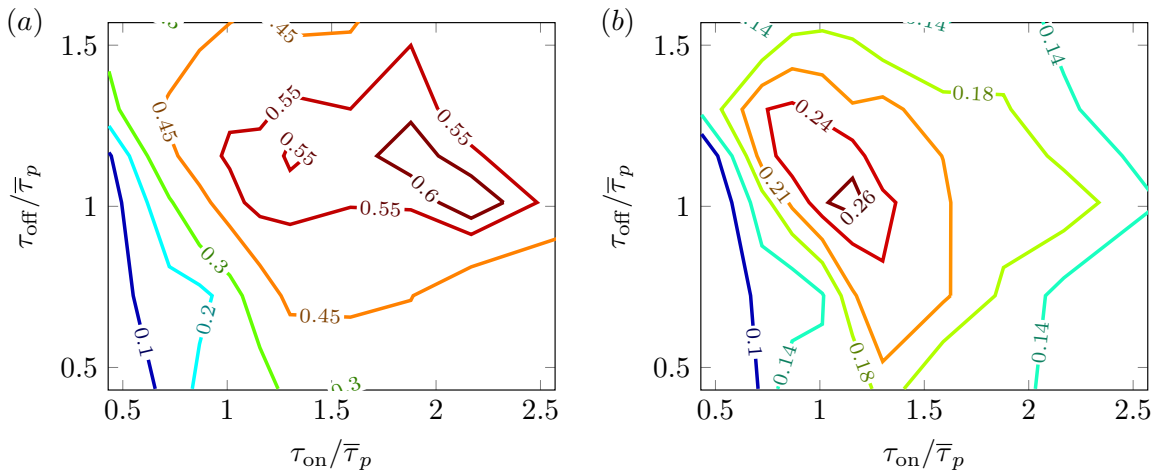

Figure 5.8 Contours of the decay exponents of Φ^2 (*a*) σ, and (*b*) λ, as functions of τ_{on} and τ_{off}. Maximum values of σ and λ correspond, respectively, to duty cycling protocols that achieve optimum mixing per cycle and per unit time.

occurring over the optimal stirring time $\overline{T}$. If we assume that no further mixing takes place during the "off" part of the cycle, then this factor translates to a decay exponent $\sigma = \log 2/(1-\phi_c^2)$. The flow modulation ensures that no unmixed core persists over long times ($\phi_c \to 0$), which predicts a maximum decay exponent $\sigma_{\max} = \log 2 \approx 0.69$, in close agreement with the maximum value of $\sigma \approx 0.65$ obtained from simulations, cf. figure 5.8. Note that the value $\sigma_{\max} = \log 2$ is the same decay as may be expected from the repeated application of a standard Smale horseshoe map [26, 97, 102], which involves a halving of length scales of fluid structures at every iteration. Here, this behavior arises from general matching conditions between a short time linear behavior and long time t^{-1} decay of Φ^2, independent of the details of the flow field.

Having understood the optimum duty cycle, we now turn to the second optimum of interest – one that results in the fastest absolute decay of Φ^2 per unit of time, for which it is now useful to rewrite (5.23) as

$$\phi^2_{\text{duty}}(t) = C\mathrm{e}^{-\lambda t/\overline{\tau}_p}, \quad \text{where} \quad \lambda = \frac{\sigma\overline{\tau}_p}{\tau_{\text{cycle}}}. \tag{5.26}$$

The duty cycle $(\tau_{\text{on}}, \tau_{\text{off}})$ that maximizes λ exists in particular due to balance between a shorter mixing times (compared with $\tau_{\text{on}} = \overline{T}_{us}$, $\tau_{\text{off}} = \overline{\tau}_p$), at the cost of lower efficiency per cycle, resulting favorably in a mixing protocol that is ultimately faster in absolute time. We keep τ_{off} fixed at $\overline{\tau}_p$, which remains the shortest "off" time that allows fluid to be transported between vortices, but now consider a τ_{on} that is some fraction fraction φ of $\overline{T}_{us}$. In general, for $\tau_{\text{off}} = \overline{\tau}_p$, we may write the

decay exponent per cycle as $\sigma(\varphi)$, which varies quadratically about its maximum value $\sigma_{\max} = \sigma(1)$. If we additionally use the relation $\sigma(0) \approx 0$ (for $\tau_{\text{on}} = 0$), we then have

$$\sigma(\varphi) \approx \sigma_{\max}\varphi(2-\varphi), \quad \text{for} \quad \tau_{\text{off}} = \overline{\tau}_p.$$

Using $\tau_{\text{cycle}} = \overline{\tau}_p + \varphi\overline{T}_{us} = \overline{\tau}_p(1+\mu\varphi)$, one finds

$$\lambda(\varphi) \approx \sigma_{\max}\frac{\varphi(2-\varphi)}{1+\mu\varphi} \quad \text{for} \quad \tau_{\text{off}} = \overline{\tau}_p, \tag{5.27}$$

which is maximized when $\varphi = (\sqrt{1+2\mu}-1)/\mu$. For the present case ($\mu = 1.87$), λ is maximized at $\varphi \approx 0.63$, corresponding to $\tau_{\text{on}}/\overline{\tau}_p = \varphi\mu \approx 1.18$ and a maximum decay rate $\lambda_{\max} = \log 2 \times \varphi(2-\varphi)/(1+\mu\varphi) \approx 0.27$. The theoretical estimates are in good agreement with the results of the simulation, as indicated in figure 5.8, and predict both the optimum cycle as well as the values of the optimum decay exponents. For typical experimental driving conditions (21.9 kHz, $\epsilon \approx 0.1$, $s \approx 0.015$), the mean transport time $\overline{\tau}_p \approx 60$ ms, setting τ_{off} for optimum mixing, consistent with experimental results [109, 112].

5.3.4 Diffusive effects

Ultimately, the advective structures generated by flow modulation are mixed at the molecular scale by diffusion. If we consider that at some given time instant t, the characteristic length scale of advective structures in bulk of the channel is l_s, the time required to homogenize the mixture is of the order $\tau_D \sim l_s^2/D_p$. Further refinement of the the advection field is only necessary if the effect of diffusion over the cycle time τ_{cycle} is negligible. Since the cycle time is essentially limited by the flow rate through the system (irrespective of the strength of the vortices), a practical estimate for the typical cycle time in such systems is given by $\tau_{\text{cycle}} \sim H/\overline{U}_p$. For a practical micromixing design, the advective mixing may be deemed to be sufficient if the diffusive time scale at the current striation thickness is much smaller than the cycle time $\tau_D \ll \tau_{\text{cycle}}$. This translates to a condition on the striation thickness in the bulk of the channel

$$l_s \ll l_s^{(1)} \equiv \sqrt{D_p\tau_{\text{cycle}}} \approx \sqrt{\frac{D_p H}{\overline{U}_p}}. \tag{5.28}$$

A second important diffusive mechanism is provided by the squeezing of much of the flow through the narrow gap (of thickness $d_{gap} \approx sH$) between the bubble and the upstream vortex as it is transported past the bubble [110, 111]. An advective structure of characteristic thickness l_s in the bulk of the channel is therefore squeezed to a structure of thickness $s \times l_s$ as it stretched through the gap. The time required to homogenize the fluid in the gap is therefore $\tau_D \sim s^2 l_s^2 / D_p$. On the other hand, the residence time of a fluid element within the gap is is $\tau_{gap} \sim a/U_s$. If complete (diffusive) mixing is to occur within the gap, it is necessary that $\tau_D \ll \tau_{gap}$. This results in a second criterion,

$$l_s \ll l_s^{(2)} \equiv \frac{1}{s}\sqrt{\frac{D_p a}{U_s}} = \sqrt{\frac{a}{sH}}\, l_s^{(1)}. \tag{5.29}$$

Ultimately, the larger of $l_s^{(1)}$ and $l_s^{(2)}$ sets the relevant condition for complete diffusive mixing of the flow in the device, allowing the design of a micromixer at the desired throughput. For typical experimental conditions ($s \sim 0.015\,, H/a = 6.25$), we find that $\sqrt{a/(sH)} \approx 3.3$, suggesting that diffusion in the gap is able to homogenize the mixture at larger bulk length scales l_s of the advection field (and therefore earlier mixing times) as compared with diffusive processes in the bulk of the channel. If the exponential decay of Φ^2 is interpreted as an exponential decay of the dominant length scale of the advection field c, one may write $l_s \sim l_0 \exp\{-\sigma t/\tau_{\text{cycle}}\}$. Assuming that the initially dominant length scale is comparable to the channel height ($l_0 \sim H$), the required residence time in the mixer is

$$\frac{t_{\text{res}}}{\tau_{\text{cycle}}} \sim \frac{1}{\sigma}\log\left(sH\sqrt{\frac{U_s}{aD_p}}\right) = \frac{1}{2\sigma}\log\left(\left(\frac{sH}{a}\right)^2 Pe\right).$$

Diffusion has been accounted for here in a somewhat simplistic way, assuming that it occurs independently from the advection. In reality, diffusive processes may be enhanced by local flow gradients [3, 34, 104]. It is then to be expected that the typical residence time required in practice is even smaller than the t_{res} estimated here.

5.4 Conclusions

In this chapter, we have investigated 2D advective mixing strategies using a microbubble array under the continuous throughput of the species to be mixed. We argue that the use of steady locally actuated vortical flows to enhance the mixing properties of an otherwise unidirectional pressure-driven flow through the channel is limited. This is primarily due to the presence of recirculation regions of the flow, which (i) inhibit the transport of fluid, and (ii) produce only slow, algebraic mixing at long times.

Both of these limitations are overcome by the deliberate introduction of flow unsteadiness, which is achieved here by a duty cycling of streaming, easily realized in experiments by a modulation of the driving voltage of the applied ultrasound. Under such a flow modulation, the quality of mixing — quantified by the mixing variance — decays exponentially with time (or equivalently the number of cycles), with the decay exponent being dependent on the duty cycle chosen. We then show that the optimum duty cycle is one which (i) optimally uses the vortical regions of the flow for stirring during the "on" part of the cycle and (ii) transports the stirred fluid between vortices during the "off" part of the cycle. The optimum duty cycle as well as the maximum decay rate of the mix-variance that is achieved by such a flow modulation is understood by a simple model of steady mixing in a vortex. This constitutes the first systematic study of flow modulation protocols for optimum micromixing under continuous transport of fluid through the microchannel, a practical constraint in most micromixing applications.

The mixture is ultimately homogenized by diffusion, which sets the characteristic striation length scale that must be achieved by the flow modulation. For a given duty cycle, this may be translated into a characteristic residence time of fluid elements in the device. For typical experimental parameters this diffusive process is expected to occur as most of the flow is stretched through a narrow bundle of streamlines near the bubble surface, where the flow is fastest.

In practice, the diffusion of the scalar field occurs simultaneously with advection, and is general enhanced by the gradients of the flow (through mechanisms such as Taylor dispersion) [3, 34, 104]. In addition, we have ignored here 3D flow effects (cf. chapter 4), which are likely to enhance the axial transport of material on both short ($\sim$ 1 ms) and long ($\sim$ 1000 ms) time scales. It is also expected that the oscillatory component of the flow (neglected here) contributes to its mixing

properties, although its precise role is unclear [116]. Despite the simplifying assumptions of the present chapter, it provides a first look into systematically understanding and quantifying open flow mixing, guiding the design of practical micromixing devices.

Chapter 6

Particle manipulation and control

In this chapter, we analyze the transport of finite-sized particles in microbubble streaming flows. We focus on the situation where the streaming is combined with a Poiseuille flow, bearing in mind the use of microbubble streaming for the design of continuous-size sorting applications. We first model the motion of particles as passive tracers advected by the steady flow due to the superposition of steady streaming and Poiseuille flows, but take into account short range contact forces between the surface of the bubble and the particles. The model predicts a size-dependent drift of particles across fluid streamlines occurring close to the bubble, which is used to understand the sorting of particles. We then show that axial flow effects are important in quantitatively translating these drifts to the size-dependent sorting of microparticles observed in experiments.

6.1 Introduction

Microfluidics often involves the control and manipulation of the motion of microparticles, which may be introduced into microfluidic flows for a variety of reasons. The most common situation in which the motion of rigid particles in the flow is important is in the experimental measurement and characterization of the flow itself (tracer particles). Other applications that involve the flow of micron-sized objects includes the trapping and sorting of microparticles based on their physical properties (e.g. size, deformability, electrical conductivity etc.), and the lysis of vesicles [55], where precise control of position and force actuation may be required.

We focus here on understanding the application of acoustically excited microbubbles in *continuous* size-size sorting microfluidic devices. We do so by considering a superposition of bubble microstreaming, for which we have already developed analytical formalisms in chapters 3 and 4, and a Poiseuille flow through the channel, which we describe in detail in the present chapter. The sensi-

tivity of the sorter to different particle sizes can be precisely tuned by varying the relative strength between streaming and Poiseuille flow. The continuous nature of the sorter allows particles to be sorted at much high throughputs compared with conventional methods.

In order to quantitatively describe the sorting process, we first develop a modification of the Poiseuille flow in a channel to account for the presence of the bubble, satisfying appropriate boundary conditions at the interface. Exploiting the low Reynolds number of the steady flow (both streaming and Poiseuille flows), we construct a family of flow superpositions governed by a single dimensionless parameter s, a measure of the strength of the Poiseuille flow relative to the streaming (cf. chapter 5). We show that over a wide range of flow superpositions, the theoretically determined flows agree well with the trajectories of fluid measured in experiments.

Any sorting device utilizing steady flows must involve a deviation between of particle trajectories from nominal fluid trajectories. In our current application of interest, this deviation is dependent on the size of the particle. We explore different sorting mechanisms that may be responsible for the experimentally observed size-dependent sorting. We first advance a simple geometric argument involving hard-core interactions between the particle and the bubble surface, which causes the particle to drift across streamlines based on its size. We then argue that three-dimensional flow effects play a crucial role in quantitatively translating these drifts to the size-sorting of spherical microparticles observed in experiments.

6.2 Setup for sorting

Figure 6.1 shows a typical setup used for size-dependent particle sorting, showing the locations of inlets and outlets of the channel and the sessile microbubble. Fluid containing particles of two different sizes is introduced into a microchannel through the inlet I_1, while fluid devoid of particles is introduced through I_2. The bubble radius is $\sim 50\,\mu m$, and the distance of the bubble center to the opposite wall is typically $100\,\mu m$ – $250\,\mu m$. The particles themselves are typically $\leq 10\,\mu m$ in diameter, smaller than the bubble size or channel dimensions.

With the streaming turned off, the flow through the channel is divided into two halves by a stagnation streamline (indicated as a light blue line in figure 6.1), which separates the lower ($I_1 \rightarrow O_1$) and upper ($I_2 \rightarrow O_2$) streams of the fluid flow. An interesting modification of the flow however

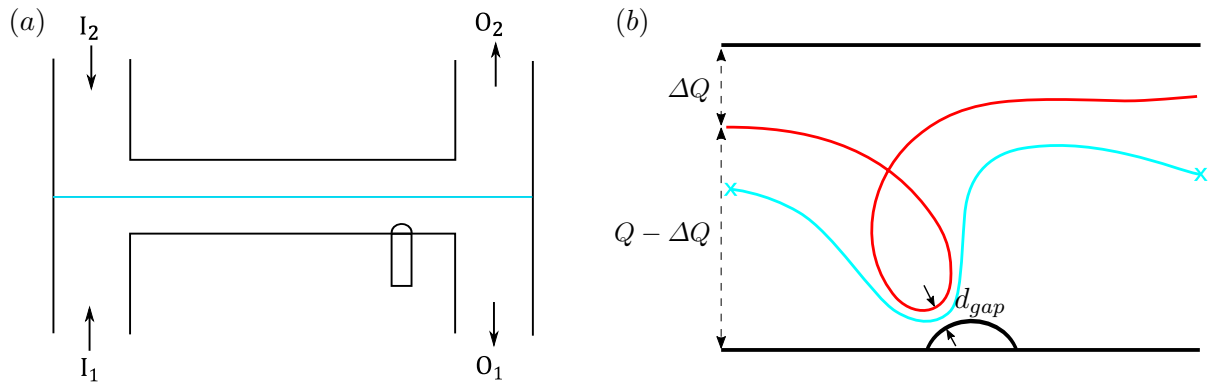

Figure 6.1 (a) Schematic of the device for microparticle sorting, showing inlets and outlets and a microbubble located in the main channel. Solution containing microparticles is infused through I_1 while glycerol-water solution enters through I_2. The outlets O_2 and O_2 are left open to the atmosphere. The light blue line represents the stagnation streamline that divides the upper and lower halves of the flow (we assume that the flow rates through the two inlets are equal), and is approximately parallel to the axis of the channel in the absence of streaming, as indicated in (a). (b) shows that the stagnation streamline (light blue) becomes deformed in the presence of streaming, but continues to divide the flow into two halves. The red streamline represents the separatrix that (i) delineates the upstream vortex and (ii) defines the region of the flow that is focused through the gap, cf. figure 5.2.

occurs when the bubble is excited sufficiently strongly, greatly altering the shape of this streamline close to the bubble. Figure 6.1(b) shows a representative resultant flow field (Poiseuille flow from left to right). Note that there are now both open streamlines and closed vortical regions in the vicinity of the bubble, and that a large portion of the flow is focused into a narrow bundle of streamlines near the bubble surface.

The overall shape of the flow field is governed by the relative strengths of the Poiseuille and streaming flows, which may be quantified by the following parameter,

$$s = \frac{\overline{U}_p}{U_{max}}. \tag{6.1}$$

Here, $\overline{U}_p = Q/HD$ is the mean Poiseuille velocity, with Q being the flow rate of fluid through the channel, and U_{max} the maximum streaming speed, which occurs at the bubble surface.

As shown in figure 6.1(b), combining streaming and Poiseuille flows divides the flow field into certain distinct regions. There are closed streamline loops upstream and downstream of the bubble. The uppermost point of the upstream loop marks a hyperbolic point with an associated critical

streamline (separatrix). The flow rate ΔQ above this streamline does not pass near the bubble, while all streamlines below it are focused into a narrow bundle between the bubble surface and the upstream loop. The bypass flow ΔQ reduces as s is lowered (stronger streaming).

Since we are considering only the time-averaged steady flow, we can define a mean distance $\overline{d}_{gap}$ between the bubble surface and the separatrix. By continuity,

$$U_{max}\overline{d}_{gap} = \int_0^h U_p dy = \overline{U}_p H \frac{Q - \Delta Q}{Q} \implies \overline{d}_{gap} = sH\left(1 - \frac{\Delta Q}{Q}\right). \tag{6.2}$$

We can also define a distance $\overline{d}_1$ to be the distance between the bubble surface and the stagnation streamline at its closest approach (refer to the blue streamline in figure 6.1*b*).

$$\overline{d}_1 = \frac{sH}{2} \tag{6.3}$$

Note that if $\Delta Q = 0$, $\overline{d}_1 = \overline{d}_{gap}/2$. Note also that the above definition of $\overline{d}_1$ requires $\Delta Q/Q < 1/2$.

6.3 Size-dependent sorting

Since particles are only introduced through inlet I_1, particles remain in the lower half of the channel and exit through outlet O_1 irrespective of their size, if no streaming is present. This is true of fluid elements even in the presence of streaming, since they are unable to cross the stagnation streamline which divides the flow into upper and lower halves.

In experiments, it is however observed that particles of finite size do get sorted if the bubble is excited sufficiently strongly by ultrasound. In particular, particles can be either (i) continuously deflected into the upper half of the channel, or (ii) deflected and trapped in the upstream vortex, from which they are eventually released. Further it is seen that these deflections are stronger for larger particles, leading to a size-dependent sorting of particles. We term (i) as "mode 1 sorting" and (ii) as "mode 2 sorting". This kind of sorting may be explained by a simple geometric mechanism. Since particles cannot penetrate the bubble surface, there is an exclusion volume around the bubble that the particle's center of mass cannot enter, represented as gray shaded regions around the bubble in figure 6.2. A particle whose center nominally follows a fluid streamline passing through

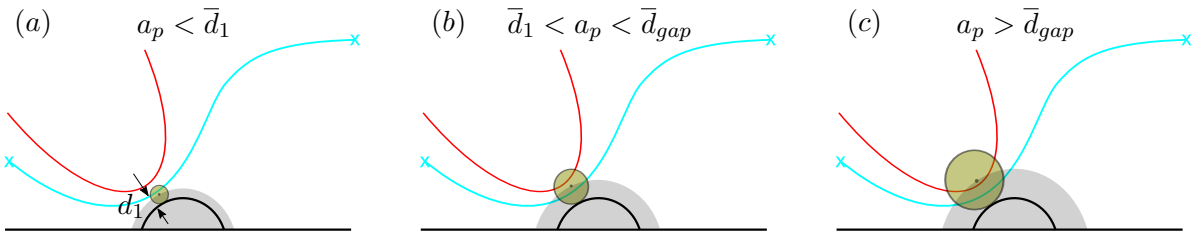

Figure 6.2 Illustration of the geometric sorting mechanism, which assumes a hard-core interaction between the particle and the mean surface of the bubble, showing (a) no sorting for $a_p < \overline{d}_1$ $(s > s_1)$ (b) continuous sorting $\overline{d}_1 < a_p < \overline{d}_{gap}$ $(s_2 < s < s_1)$ and (c) trapping $a_p > \overline{d}_{gap}$ $(s < s_2)$. The minimum distance d_1 between the stagnation streamline and the bubble is indicated in (a). The gray shaded regions represent exclusion volumes around the bubble; since particles cannot penetrate the bubble surface, their centers of mass cannot enter this exclusion volume.

this exclusion volume must therefore, unable to enter this volume, cross streamlines. Downstream of the bubble, the particle therefore only has access to fluid streamlines that avoid the exclusion volume entirely, provided that it does not experience any further deflections past the bubble.

This simple geometric argument can be used to formulate a size-dependent sorting mechanism. For the trapping of the particle (mode 2 sorting), its center of mass must be deflected beyond the separatrix that delineates the upstream vortex. This leads to following simple criterion for Mode 2 sorting:

$$a_p > \overline{d}_{gap}. \tag{6.4}$$

On the other hand, for continuous (mode 1) sorting to take place, the particle radius must be large enough for its center of mass to be pushed beyond the stagnation streamline, but smaller than than $\overline{d}_{gap}$. This occurs when when the following condition is met:

$$\overline{d}_{gap} > a_p > \overline{d}_1. \tag{6.5}$$

The criteria for mode 1 and mode 2 sorting transitions can respectively be recast in terms of critical values of s , $s_1 = 2a_p/H$, and $s_2 = a_p/H \times (1 - \Delta Q/Q)^{-1}$, respectively (see figure 6.2). Experimental results of Thameem et al. [105] show that for small ΔQ, the ratio $s_1/s_2 \approx 2$, which is predicted by the geometric sorting mechanism (since $\overline{d}_{gap}/\overline{d}_1 \approx 2$). The parameter $s = \overline{U}_p/U_{max}$ is therefore a valuable predictor of the sorting. However, the absolute values of $\overline{d}_{gap}$ and $\overline{d}_1$ do not agree with the sorting criteria (6.5) and (6.4). This will be addressed in section 6.3.2.

6.3.1 Theoretical particle trajectories

The sorting mechanism described in the previous section may in principle be extended to other setups involving a greater number of inlets or outlets. In order to have precise control over such setups, it is important to understand particle trajectories in more detail. Here we construct an asymptotically valid flow due to the combination of streaming and Poiseuille flows and verify that the theory accurately predicts experimentally measured trajectories of particles over a range of s values.

The net steady flow may be expressed as a linear superposition of streaming and transport flow fields, owing to typically small Reynolds numbers of the steady flow ($Re_s \lesssim 1$). It is convenient to normalize lengths by a, so that the dimensionless channel height and depth are given respectively by $h \equiv H/a$ and $d \equiv D/a$, and speeds by the streaming speed scale $U_s = \epsilon^2 a\omega$. We use a right handed coordinate system (x, y, z) centered at the mid-point of the bubble axis, so that y spans the height of the channel, and z is directed along the axis of the bubble.

The unidirectional pressure-driven Poiseuille flow through a channel of rectangular cross section in the absence of the bubble is given by [66]. Normalized by its mean speed over the channel cross-section, the velocity profile $u_p(y, z)$ of the fully developed channel flow may be written as

$$u_p(y,z) = \left\{ \sum_{n=1,3,\ldots}^{\infty} \frac{2}{n^4\pi} \left(1 - \frac{2h}{n\pi d} \tanh \frac{n\pi d}{2h}\right) \right\}^{-1} \times \sum_{n=1,3,\ldots}^{\infty} \frac{1}{n^3} \left(1 - \frac{\cosh(n\pi z/h)}{\cosh(n\pi d/(2h))}\right) \sin(n\pi y/h). \tag{6.6}$$

Note that the direction of the Poiseuille flow is purely in the $\hat{\boldsymbol{x}}$ direction.

To make comparisons with experiments, we will only consider the flow profile in the mid-plane $z = 0$ (the experimental data are collected in a region of $\approx 10\mu$m width about $z = 0$). This allows us to define an effective stream function governing the transport flow in the mid-plane, given by

$$\psi_p(x,y) = \int_0^y u_p(y', 0)\, \mathrm{d}y' \,.$$

This solution must however be modified to also satisfy the bubble boundary conditions (no-penetration

and no-stress). If we assume that any modification of the flow resulting from the introduction of the bubble at $r = 1$ is approximately 2D (small axial gradients), the flow in the midplane is given by the modification

$$\psi_p \mapsto \psi_p + \xi_p, \tag{6.7}$$

valid in the limit of small Reynolds number, so that ξ_p satisfies the Stokes equations ($\nabla^4 \xi_p = 0$).

Temporarily ignoring the presence of the opposite wall at $y = h$, ξ_p may be written using an expansion into no-slip Stokes solutions as

$$\xi_p(x, y) = \sum_{n=0}^{\infty} \frac{b_n}{r^n} \left(\cos\left\{ n \left(\theta - \frac{\pi}{2} \right) \right\} + \alpha_n \cos\left\{ (n+2) \left(\theta - \frac{\pi}{2} \right) \right\} \right) \tag{6.8}$$

where $r = \sqrt{x^2 + y^2}$, $\tan\theta = y/x$, and

$$\alpha_n = \begin{cases} 1, & n \text{ even}, \\ \dfrac{n}{n+2}, & n \text{ odd}. \end{cases} \tag{6.9}$$

The coefficients b_n are chosen such that that both no penetration and no-stress conditions are satisfied at the bubble surface, i.e.

$$\frac{1}{r} \frac{\partial \psi_p}{\partial \theta} = \left(\frac{\partial^2}{\partial r^2} - \frac{1}{r} \frac{\partial}{\partial r} - \frac{1}{r^2} \frac{\partial^2}{\partial \theta^2} \right) \psi_p = 0, \quad \text{on} \quad r = 1. \tag{6.10}$$

In general, the coefficients b_n may be obtained analytically for arbitrary n using a Fourier transform in θ of the undisturbed solution at $r = 1$. This is analogous to the expressions (3.21) obtained for the streaming flow in half-space in chapter 3. Here, we determine them numerically by evaluating the boundary conditions on a finite number of points on $r = 1$ (collocation).

The stream function obtained by this procedure satisfies the bubble boundary conditions, but now introduces velocity components of $O(h^{-1})$ at the opposite wall $y = h$. This can be accommodated using a second correction

$$\psi_p \mapsto \psi_p + \chi_p, \tag{6.11}$$

where $\chi_p(x, y)$ is again a solution of the Stokes equations. χ_p is obtained by precisely the same

method (Fourier transform in x) used to extend the half-space streaming solution to a channel of finite height, detailed in section 3.6. Iterative application of $\psi_p \mapsto \psi_p + \xi_p$ and $\psi_p \mapsto \psi_p + \chi_p$ results in a flow that satisfies all boundary conditions (bubble and wall), with excellent convergence being reached within two iterations.

For the streaming, we use the time averaged Lagrangian flow field, which is two-dimensional to first approximation in the xy plane. The stream function ψ_s describing the steady Lagrangian streaming flow in a channel of height h is obtained by a semi-analytic modification of the half-space ($h \to \infty$) solution at any driving frequency, cf. chapter 3, [77, 78].

The net two-dimensional flow satisfying both bubble and wall boundary conditions is given by the superposition

$$\psi = \psi_s + s u_{max} \psi_p, \tag{6.12}$$

where u_{max} is the dimensionless maximum speed of the streaming (in units of U_s). The value of s sets the relative strength between the streaming and transport flows. At a driving frequency of 20 kHz (typical in experiments), $u_{max} \approx 1.5$, predicted by asymptotic theory (cf. chapter 3), and confirmed by experimental measurements.

The motion of particles of finite size is modeled by a passive advection by the flow (constant value of ψ) in regions where the separation between the particle center and the bubble is greater than the particle radius, i.e. $r > 1 + a_p$. If the passive advection of the particle results in a violation of this condition, the particle is displaced in radially outward along constant θ to a radial coordinate $r = 1 + a_p$, and the passive advection is continued. This ensures that the particle and bubble surfaces never penetrate each other, and is consistent with the geometric size-sorting mechanism in 6.2. Particle advection under a given flow field and initial conditions are computed numerically using a fourth order Runge–Kutta scheme.

A comparison of theoretical predictions for particle transport with a set of experimental conditions (frequency, voltage and flow rate) requires both a determination of the theoretical flow field (equivalently a value of theoretical s), as well as the initial particle positions resulting in the experimentally measured trajectories. For a fixed s, one may compute a set of (theoretical) stream function values corresponding to experimentally measured particle positions (x_i, y_i), given by $\psi_i^{expt} \equiv \psi(x_i, y_i)$. For the same s and some initial conditions, theoretical particle trajectories

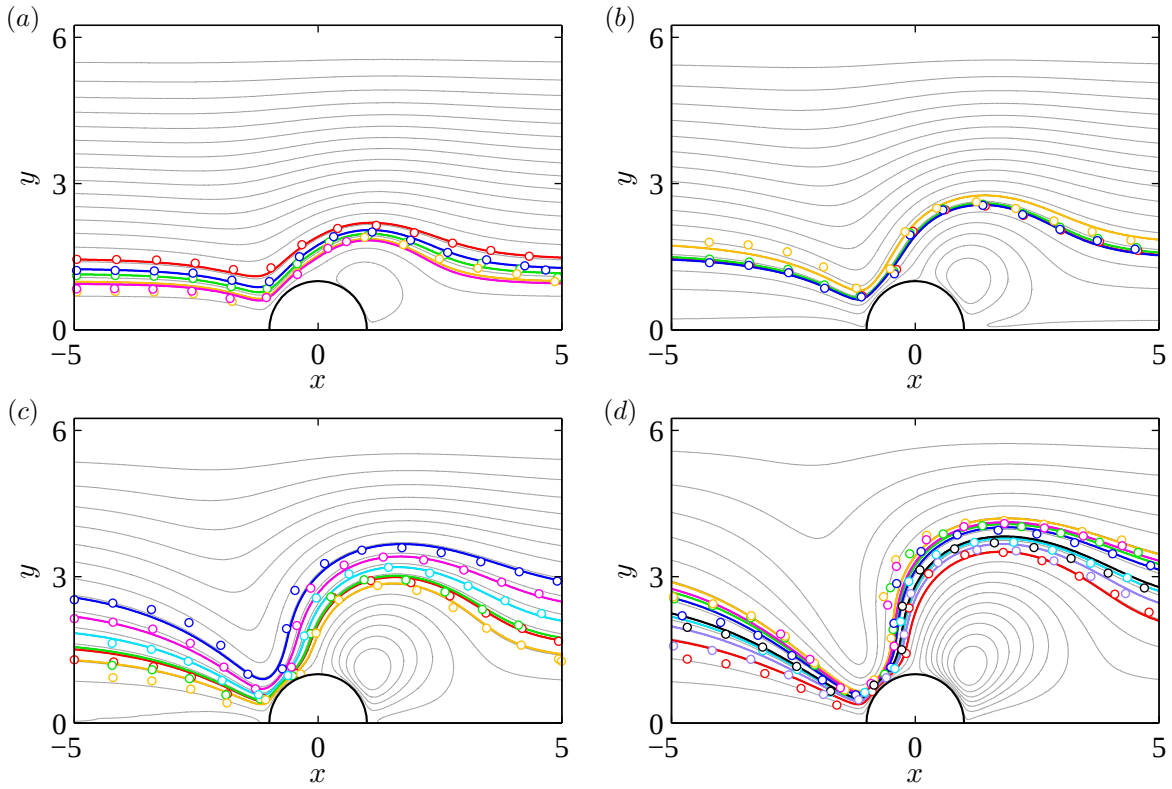

Figure 6.3 Comparison of theoretical trajectories with experimentally measured trajectories of 5 μm particles at $f = 20$ kHz, $\overline{u_p} = 1333$ μm/s, at four different driving voltages. Open circles are experimental points, while solid lines represent theoretical trajectories : (a) $V = 0.4$ V, $s_{th} = 0.1411$, $s_{exp} = 0.1604$; (b) $V = 0.5$ V, $s_{th} = 0.0666$, $s_{exp} = 0.0641$; (c) $V = 0.6$ V, $s_{th} = 0.0382$, $s_{exp} = 0.0375$; (d) $V = 0.7$ V, $s_{th} = 0.0230$, $s_{exp} = 0.0271$.

assume a set of ψ values as they pass through the experimentally measured x_i, denoted by ψ_i^{theory}. The error between the experimental and theoretical trajectories is quantified by the deviation between the two sets of stream function values over all data points i and all particle trajectories. The theoretical value of s (flow field) and initial conditions that provide the best fit between the theory and experiment is obtained by the global minimum over s and initial conditions of the error functional

$$\mathcal{E}(s, IC) = \sum_i \left(\frac{1}{\rho_i} \frac{\psi_i^{theory} - \psi_i^{expt}}{\psi_i^{theory}} \right)^2 , \tag{6.13}$$

where $\rho_i = ||\boldsymbol{x}_{i+1} - \boldsymbol{x}||^{-1}$ is spatial density of experimental data points. The factor $1/\rho_i$ allows a uniform *spatial* weighting of the experimental data, rather than uniform temporal weighting obtained by experimental data collection at a fixed frame rate. The global miminum of $\mathcal{E}$ over s and initial particle positions (IC) corresponds to a best-fit between experiment and theory, resulting

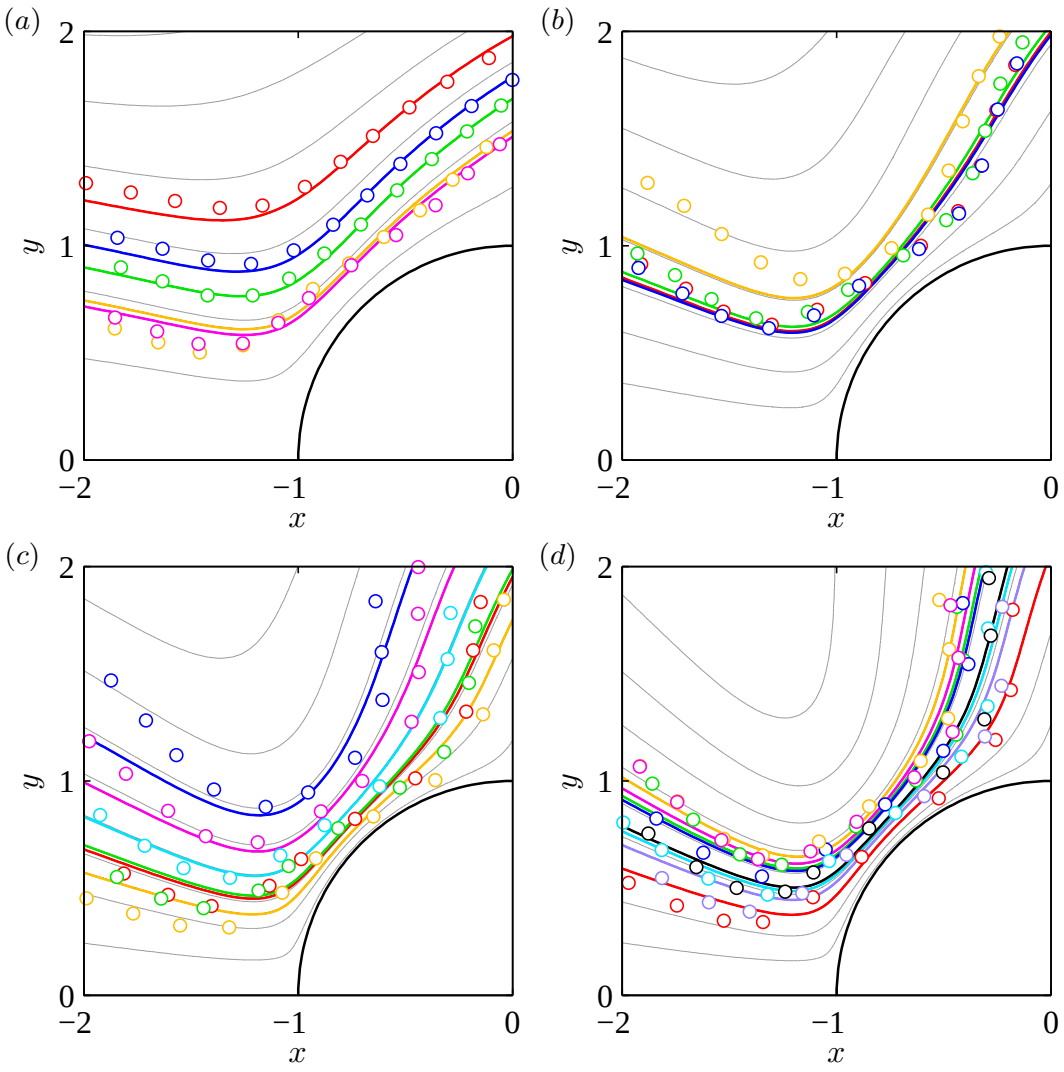

Figure 6.4 Theoretical (lines) and experimental particle trajectories (5 μm diameter, markers) near the bubble at four different driving voltages: (a) $V = 0.4$ V, $s_{th} = 0.1411$, $s_{exp} = 0.1604$; (b) $V = 0.5$ V, $s_{th} = 0.0666$, $s_{exp} = 0.0641$; (c) $V = 0.6$ V, $s_{th} = 0.0382$, $s_{exp} = 0.0375$; (d) $V = 0.7$ V, $s_{th} = 0.0230$, $s_{exp} = 0.0271$.

in a theoretically predicted s value.

6.3.2 3D effects on gap size

In section 6.3, we commented that while the ratio between $\overline{d}_1$ and $\overline{d}_{gap}$ for Mode 1 and Mode 2 sorting transitions agreed with experimental measurements, their absolute values did not. The discrepancy between expected and computed gap sizes is striking. For particles of 10 μm diameter, one would expect the Mode 1 and Mode 2 sorting transitions to occur at gap sizes of roughly 10

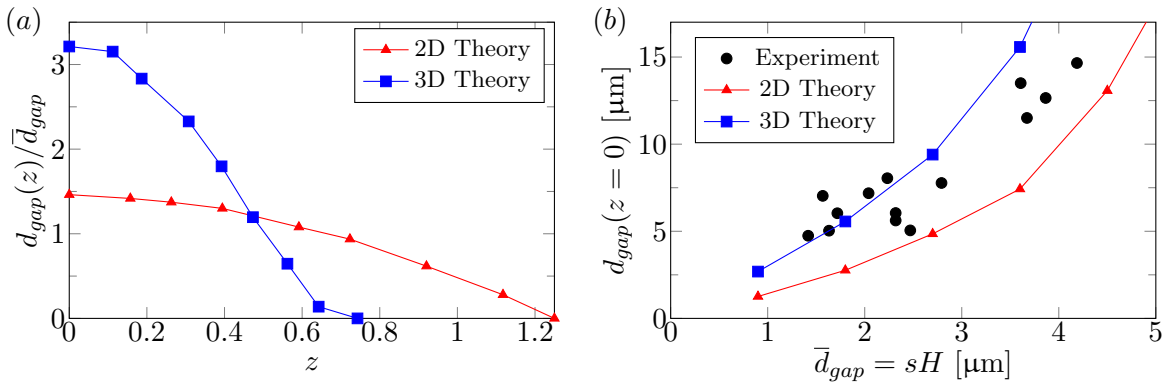

Figure 6.5 (a) Gap width as a function of z at $s = 0.005$, normalized by the mean gap width $\overline{d}_{gap}$, showing that the 3D streaming theory predicts a wider gap compared to 2D theory and that the maximum gap width occurs at $z = 0$. (b) Gap widths in the mid-plane ($z = 0$) plotted against the mean estimated gap width $\overline{d}_{gap} = sH$, showing results from experiments, as well as 2D and 3D theories of the streaming, indicating good agreement between the 3D theory and experimental measurements. Microparticles typically used in sorting experiments have diameters $\leq 10\mu$, which sets the range of the d_{gap} values relevant to sorting experiments.The peak axial velocity component in the 3D theory is ≈ 0.25 the maximum in-plane velocity u_{max} (as measured in [54]) showing that even weak axial effects can enhance the actual width of the gap compared to its mean value $\overline{d}_{gap}$.

μm and 5 μm, respectively, assuming zero ΔQ; see (6.5), (6.4). Instead, the average computed gap width $\overline{d}_{gap}$ turns out to be 2.75 μm (27.5 % of expected value) and 1.54 μm (30.8 % of expected value) respectively. However, direct experimental measurements of gap widths at the mid-plane of the channel show that the mid-plane gap-widths at Mode 1 and Mode 2 sorting transitions are only slightly larger than the expected values of 10 μm and 5 μm.

This discrepancy may be explained by taking into account the 3D character of the flow. The use of Equation 6.2 to calculate gap size implicitly assumes that (i) the streaming speed is planar and uniform across the depth of the channel, and (ii) that the net flow rate through the gap $Q - \Delta Q$ is distributed uniformly through the channel depth. On the other hand, most particles that flow past the bubble do so near $z = 0$, where the Poiseuille flow is fastest. The average gap size $\overline{d}_{gap}$ computed using (6.2) is therefore not representative of the flow experienced by the majority of particles in the channel.

Relaxing the 2D assumption (and thus also the stream function representation of the flow), we consider a broader class of flow superpositions between the streaming and Poiseuille flows of the form

$$\boldsymbol{u} = \boldsymbol{u}_s + s u_{max} \boldsymbol{u}_p, \tag{6.14}$$

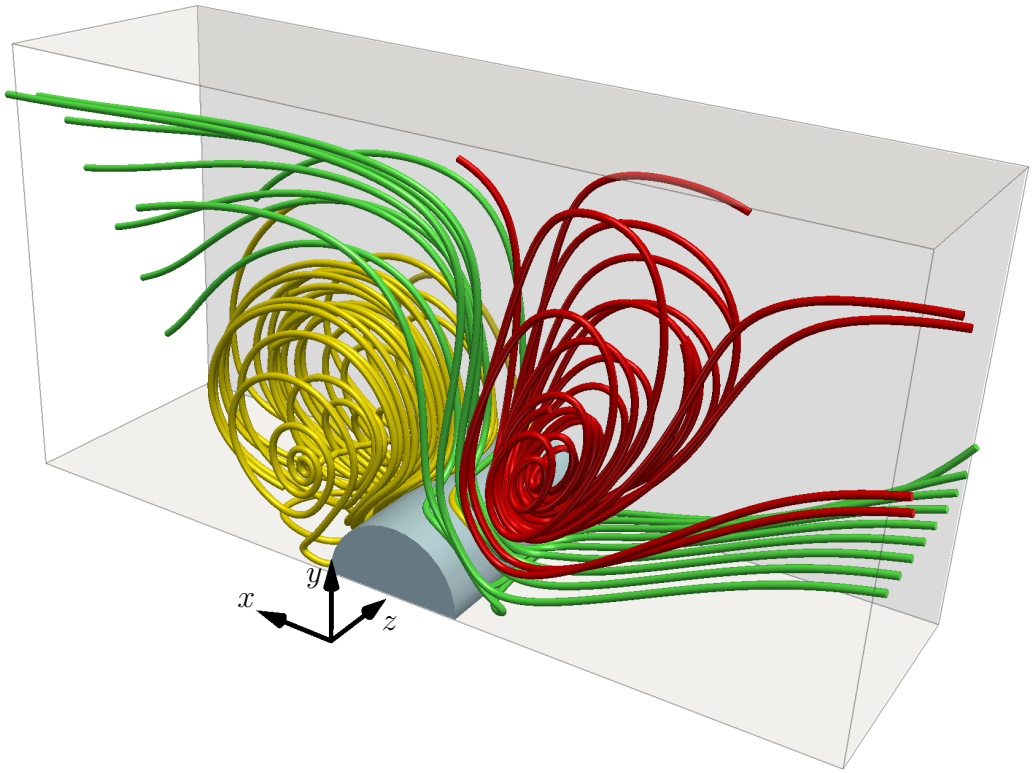

Figure 6.6 Three-dimensional fluid streamlines under the superposition of 3D steady streaming and Poiseuille flow in one half of the channel ($0 \leq z \leq d/2$), showing open streamlines (green), the upstream vortex (red) and the downstream vortex (yellow). The bubble ($r = 1$) is indicated as a light blue cylinder, and walls of the channel ($y = 0$, $y = h$ and $z = d/2$) are indicated as gray planes. The Poiseuille flow is in the positive x-direction. The flow has reflection symmetry about $z = 0$.

where $\boldsymbol{u}$ may now contain non-zero axial gradients and velocity components. This allows us to define more generally a z-dependent gap size $d_{gap}(z)$ as the minimum separation distance between the upstream vortex and semi-cylindrical bubble interface (over θ) as a function of z, so that a more relevant indicator of the sorting is the gap size close to the mid-plane, $z = 0$.

As a first approximation, we take into account the z variation of the Poiseuille flow, but retain the 2D solution for the streaming. This is a relatively simple modification, and produces a quasi-2D flows of the type $\boldsymbol{u} = \{u_x(x, y, z), u_y(x, y, z), 0\}$. While such a superposition predicts that the $d_{gap}(z = 0) > \overline{d}_{gap}$, it still underpredicts the direct experimental measurements of the gap width, as shown in figure 6.5.

We find, however, that even the introduction of weak axial streaming flow components (cf.

chapter 4) improves the agreement between the theory and experimental measurements. Figure 6.6 plots fluid streamlines of the flow resulting from the superposition of 3D streaming and Poiseuille flow, indicating open streamlines, and upstream and downstream vortex structures, which now have 3D character. Here, we use a flow superposition of the 3D streaming and axial Stokes solutions so that the maximum axial components of fluid velocity are $\approx 0.25u_{max}$, consistent with experimental measurements by Marin et al. [54]. While the axial flow strength in the present experiments is unknown, it is evident that the introduction of axial flows in the theory accurately captures experimental measurements of the gap width at the mid-plane, over a wide range of gap widths, as indicated in figure 6.5.

In addition to increasing the maximum gap width at a given value of the mean gap size d_{gap}, the introduction of axial streaming flow effects adds another interesting effect. Due to the direction of the axial streaming velocity components, fluid elements are focused towards the mid-plane ($z = 0$) as they pass by the bubble through the gap, see figure 6.6. This can be understood from the discussion in chapter 4 explaining experimentally measured streaming flow velocities; the fluid flows towards the mid-plane ($z = 0$) near the wall ($y = 0$) and toward the nearest axially confining wall (either top or bottom walls for $z > 0$ and $z < 0$ respectively) near the symmetry plane $x = 0$. The superposition of the 3D streaming with a Poiseuille flow thus causes streamlines to converge towards $z = 0$ as they flow into the gap and diverge away from $z = 0$ as they leave it.

6.4 Conclusions

We have demonstrated here that steady streaming flows driven by acoustically excited microbubbles can be used effectively for the continuous size-sensitive sorting of particles. By superimposing the streaming flow with a pressure-driven Poiseuille flow through the channel carrying microparticles, have designed a continuous size-sensitive sorting device whose throughput is limited only by the flow rate of Poiseuille flow. The experimental particle trajectories were accurately modeled using an asymptotic description of the flow field.

We advanced a simple geometric sorting mechanism that relies on the inability of particles to penetrate the bubble surface, which predicts that particles must be differentially deflected (based on their size) across streamlines as they pass through a narrow gap near the bubble. While this

mechanism only qualitatively explains size-sorting under a 2D model flow, we show ultimately that by accounting for 3D (axial) flow components (driven by the axial confinement of the bubble), the theory quantitatively models the experimentally observed sorting. We have shown that the size-sensitivity of the device (controlled by the gap width) may be tuned by varying the relative strength of the streaming to the Poiseuille flow, achieved simply by adjusting the driving voltage of the ultrasound, without the need to actively manipulate individual particles or modify the device geometry.

We have thus described, using experiment and theory, a simple geometric mechanism of continuous particle sorting in microfluidic flows. Contrary to other sorting devices [53], the sorting occurs over short time scales (1 ms) where the flow is the fastest, without the use of any active feedback. Future work will focus on developing a hydrodynamic basis for the observed sorting, which accounts not only for the geometric arguments employed here, but more generally the effect of long-range hydrodynamic forces on particle migration, advancing the work toward a more general understanding of particle dynamics in microfluidic flows.

Chapter 7

Conclusions

In this dissertation, we have systematically quantified the theoretical and practical aspects of flows driven by acoustically excited microbubbles. Keeping in mind practical microfluidics applications and the ease of manufacture, we have considered bubbles that are (i) semi-cylindrical in shape, and (ii) attached to walls of the microchannel.

7.1 Summary of research

In the first part of this body of work, we focused on developing a rigorous asymptotic theory of the two-dimensional steady flow due to a semi-cylindrical bubble excited by spatially uniform pressure oscillations. Using a perturbation series expansion in amplitude, we resolved both primary and secondary flows fields, using only the driving frequency and the fluid and interfacial properties as inputs. We have therefore, for the first time, provided a self-consistent connection between interface oscillation dynamics and steady streaming flows. The theory makes quantitative predictions over a wide range of frequencies, explaining frequency-dependent streaming phenomena that have been observed previously in experiments but never rationalized theoretically (e.g. [17]). This makes the theory extremely useful to understand practical experiments with bubbles, where the experiment typically only has control of the oscillation frequency and the geometry of the problem.

We then extended the 2D theory to take into account the axial confinement of the bubble, thereby providing a 3D description of the flow. We show that 3D (axial) flow components are excited due to the presence of axially confining no-slip walls, which introduce two sources of axial flows: (i) axial oscillation modes of the bubble, and (ii) no-slip conditions at the axially confining walls. While (i) is specific to bubbles and depends in general on the axial oscillation dynamics, (ii) is more general and may be important in other microfluidic systems where the primary flow is

two-dimensional. Motivated by this idea, we developed a general Hamiltonian formalism for the 3D kinematics of perturbed 2D flows under confinement. The 3D theory has predicted modifications of the 2D flow on both longer and (more unexpectedly) shorter time scales; both of which were observed in experiment. This forms the first quantitative description of 3D streaming flow in any system, advancing important ideas and techniques that are useful in understanding and modeling experimentally observed streaming flows.

Having described in detail the flow fields and kinematics of fluid particles, we analyzed some practical applications of interest. We first tackled the general problem of achieving exponentially fast micromixing of fluid flowing through a microfluidic channel at a constant throughput. As a practically realizable example of such a flow, we focused on the superposition of a channel Poiseuille flow and streaming flow due to microbubble streaming. We showed that a flow modulation via duty-cycling of the streaming vortices achieves exponential mixing, which is optimized by a specific duty cycle and can be understood by considering steady transport properties of (i) the Poiseuille flow, and (ii) the streaming vortices. This forms the first systematic study of optimized protocols for open-flow mixing, providing a basis on which to design practical micromixers.

We finally considered the transport of finite size spherical particles in bubble microstreaming flows, with an emphasis on the design of a continuous size-sensitive microparticle sorting device. We first argued that the superposition of streaming and Poiseuille flow is able to accurately reproduce experimental trajectories of particles including particle drifts across streamlines, by taking into account short range hard-core interactions between the particle and bubble surfaces. We then showed that in order for such a mechanism to be accurately translated into the sorting behavior observed in experiments, 3D (axial) flow components need to be taken into account.

7.2 Ongoing and future work

7.2.1 Inertial forces on particles

Much of microfluidics involves not just the manipulation of the flow, but also the manipulation of particles or other objects within the flow. Relatively little is known about the behavior of microparticles in microfluidic flows in the general case, i.e. that of unsteady spatially non-uniform

flows. Recent efforts have shown that in the case of a steady, unidirectional Poiseuille flow, the effect of finite particle inertia can be accounted for by a regular asymptotic expansion in the particle Reynolds number [31]. This is in contrast with earlier studies, which have relied on Saffman-like terms, arising from a singular perturbation expansion in Reynolds number [7]. Both these effects have very different origins, and scale differently with Reynolds number [29, 91].

The issue is further complicated by the presence of boundaries [28, 31] and the introduction of unsteadiness [19, 48] or spatially non-uniform flows, for which no systematic theory exists. It is somewhat surprising that this is the case, since many microfluidic applications rely on vortical or unsteady flow actuation elements, in addition to a pressure driven flow, in order to manipulate microparticles. This argues for the development of a more generally applicable theory of particle dynamics which accounts for (i) the walls of the channel, (ii) unsteadiness and spatial inhomogeneity, and (iii) inertial effects.

Even if it is possible to develop such a general theory of hydrodynamic forces on particles, computing particle dynamics within the framework may be computationally challenging for practically relevant flows. A relatively simple theory of particle dynamics (zero Reynolds number, unbounded fluid) is provided by Maxey and Riley [61], which describes the motion of a particle by means of a highly non-linear ordinary differential equation for its position. While the Maxey–Riley equation does not admit analytical solutions (even for relatively simple flows), we expect that approximate solutions may be obtained for the Lagrangian motion of particles in small-amplitude oscillatory flows. In particular, due to the separation of time scales between oscillatory and steady flow components, it is expected that Lagrangian particle motion on oscillatory time scales will become rectified into a steady (time-averaged) motion on longer time-scales. We anticipate that this time scale separation will allow for the development of a field theory of particle motion in streaming flows (analogous to descriptions of Lagrangian *fluid* motion in such flows), significantly reducing computational effort.

The direction for immediate research on particle dynamics is therefore to (i) develop a general theory of particle dynamics relevant to microfluidics, and (ii) asymptotically analyze such a theory for streaming flows in the limit of small amplitude. It is hoped that these descriptions can be extended to deformable and non-spherical particles, bearing in mind practical applications such as the manipulation of biological and other soft materials in microfluidics.

7.2.2 Diffusive transport of particles

Another problem of interest is the effect of diffusion on the transport of non-inertial particles in streaming flows. It is well known that flow gradients enhance the dispersion of a species beyond classical diffusion (diffusion without advection) [3, 104]. Ismagilov et al. [34] showed that for a pressure-driven flow in a microchannel, material near the center of the channel obeys the classical diffusion behavior, whereas material near the walls of the channel diffuse much faster, due to flow gradients. We propose a generalization of this idea to arbitrary flow fields in the limit of small (but finite) diffusivity, by following material elements along streamlines. The results may explain the apparent deviation of experimental trajectories of 100 nm-diameter nanoparticles from streamlines, particles too small to be affected by inertial forces.

In addition, such an analysis may provide a general framework under which to study micromixing in flows with finite diffusivity. For example, in chapter 5, diffusion was neglected entirely during the advection process. The precise way in which diffusion is enhanced in unsteady flows is relatively unclear, although recent work by Meunier and Villermaux [64] has advanced a numerical technique that allows such effects to be computed under specific initial distributions of the scalar field. This is a question of great relevance in practical micromixing applications, where it is important to have both chaotic advection (e.g. by flow modulation) for rapid stretching and folding of fluid elements, as well as shear-enhanced diffusion (for homogenization of the mixture). A deeper understanding of these phenomena will lead to the more systematic design of micromixers from first principles.

7.3 Closing remarks

Fundamental studies of bubble dynamics and microstreaming are crucial in systematically understanding and utilizing microbubble acoustics in microfluidic applications. In this work, we have, for the first time, developed a rigorous quantitative theory that connects the resonance properties of acoustically excited microbubbles and experimentally observed steady flows. We have also completed the first description of three-dimensional microstreaming in any system, developing ideas that are applicable not only to microstreaming, but also more broadly to practically relevant situations in microfluidics.

The versatility and generality of the asymptotic theory has made it immediately useful in the design and analysis of practical microfluidics applications relying on microbubble streaming. We have developed the first systematic study of optimum protocols for open-flow mixing, as well as studied size-sensitive microparticle sorting using bubble microstreaming. We expect that this work will, through both its fundamental and practical aspects, benefit researchers from communities including fluid mechanics, bioengineering and biophysics.

In the pursuit of accurately quantifying practical applications of streaming flows, this work on bubble microstreaming has provided both the context and the motivation to understand more general problems in fluid mechanics, such as the behavior of particles in flows and the optimization of micromixing in practically realizable systems.

Appendix A

Lagrangian boundary conditions at the bubble

Here we derive effective boundary conditions that must be satisfied by the oscillatory and steady flow components at the mean bubble surface. We assume that the bubble interface executes time periodic motion of the form

$$R(\theta, t) = 1 - \mathrm{i}\epsilon\zeta(\theta)\mathrm{e}^{\mathrm{i}t} \tag{A.1}$$

where $\zeta(\theta)$ is an arbitrary complex valued functions. We show here that for an arbitrary interface deformation $\zeta(\theta)$ in (2.47), the Lagrangian steady flow satisfies homogeneous boundary conditions on normal velocity and tangential stress at $r = 1$.

We first give the general form of the boundary conditions on the moving interface. The kinematic boundary condition, after defining $F(r, \theta, t) \equiv r - R(\theta, t)$, becomes

$$\frac{\mathrm{D}F}{\mathrm{D}t} = 0 \quad \text{on} \quad r = R(\theta, t),$$

where

$$\frac{\mathrm{D}}{\mathrm{D}t} \equiv \frac{\partial}{\partial t} + (\boldsymbol{u} \cdot \nabla)$$

is the material derivative. Expanding the velocity field as $u = u_0 + \epsilon u_1 + O(\epsilon^2)$, and using an expansion about the mean bubble interface $r = 1$, this yields for the kinematic condition.

$$0 = \epsilon \left(u_0 - \zeta e^{\mathrm{i}t}\right) + \epsilon^2 \left(u_1 - \left(\mathrm{i}\zeta \mathrm{e}^{\mathrm{i}t}\right) \frac{\partial u_0}{\partial r} + \left(\mathrm{i}\zeta' \mathrm{e}^{\mathrm{i}t}\right) \frac{v_0}{r}\right) + O(\epsilon^3) \quad \text{on} \quad r = 1, \tag{A.2}$$

where u and v represent radial and tangential velocity components respectively.

Likewise, the tangential stress vanishes on $F = 0$, and is written for an Newtonian fluid as

$$\hat{\boldsymbol{n}} \cdot \boldsymbol{S} \cdot \hat{\boldsymbol{t}} = 0 \quad \text{on} \quad r = R(\theta, t),$$

where $\boldsymbol{S}$ is the symmetric part of $\boldsymbol{\nabla u}$, and $\hat{\boldsymbol{n}}$ and $\hat{\boldsymbol{t}}$ are unit normal and tangent vectors to the interface, defined as

$$\hat{\boldsymbol{n}} \equiv \frac{\nabla F}{|\nabla F|} \quad \text{on} \quad F = 0, \quad \text{and} \quad \hat{\boldsymbol{t}} \equiv \hat{\boldsymbol{z}} \times \hat{\boldsymbol{n}}.$$

Again expanding around $r = 1$ to $O(\epsilon^2)$, we obtain for the unit normal and tangent

$$\hat{\boldsymbol{n}} = \hat{\boldsymbol{e}}_{\boldsymbol{r}} + \mathrm{i}\epsilon\, \zeta' \mathrm{e}^{\mathrm{i}t} \hat{\boldsymbol{e}}_{\boldsymbol{\theta}} + O(\epsilon^2)\,, \quad \hat{\boldsymbol{t}} = \hat{\boldsymbol{e}}_{\boldsymbol{\theta}} - \mathrm{i}\epsilon\, \zeta' \mathrm{e}^{\mathrm{i}t} \hat{\boldsymbol{e}}_{\boldsymbol{r}} + O(\epsilon^2). \qquad (A.3a, b).$$

Using the expansion for the velocity field, one finds the stress condition

$$0 = \epsilon\, S_{0\,r\theta} + \epsilon^2 \left(S_{1\,r\theta} - \left(\mathrm{i}\zeta e^{\mathrm{i}t}\right) \frac{\partial S_{0\,r\theta}}{\partial r} - \frac{\mathrm{i}\zeta' e^{\mathrm{i}t}}{r} \left(S_{0\,rr} - S_{0\,\theta\theta} \right) \right) + O(\epsilon^3) \quad \text{on} \quad r = 1\,. \qquad (A.4)$$

Rewriting (A.2) and (A.4) in terms of the stream function ψ, the $O(\epsilon)$ terms reproduce the oscillatory boundary conditions (3.3), which we rewrite here

$$\left.\begin{aligned} &\frac{1}{r}\frac{\partial \psi_0}{\partial \theta} = \zeta \mathrm{e}^{\mathrm{i}t} \\ &\left(\frac{\partial^2}{\partial r^2} - \frac{1}{r}\frac{\partial}{\partial r} - \frac{1}{r^2}\frac{\partial^2}{\partial \theta^2} \right) \psi_0 = 0 \end{aligned}\right\} \quad \text{on} \quad r = 1. \qquad (A.5)$$

We now derive kinematic and stress boundary conditions on the streaming, obtained respectively from a time average over the $O(\epsilon^2)$ terms in (A.2) and (A.4). For the kinematic condition, we find

$$\begin{aligned} \frac{1}{r}\frac{\partial \langle \psi_1 \rangle}{\partial \theta} &= -\left\langle \int \frac{1}{r}\frac{\partial \psi_0}{\partial \theta} \mathrm{d}t \cdot \frac{\partial}{\partial r}\left(\frac{1}{r}\frac{\partial \psi_0}{\partial \theta} \right) \right\rangle - \left\langle \int \frac{1}{r}\frac{\partial^2 \psi_0}{\partial \theta^2} \mathrm{d}t \cdot \frac{1}{r}\frac{\partial \psi_0}{\partial r} \right\rangle \quad \text{on} \quad r = 1 \\ &= -\frac{1}{r}\frac{\partial}{\partial \theta} \left\langle \frac{\partial \psi_0}{\partial r} \int \frac{1}{r}\frac{\partial \psi_0}{\partial \theta} \mathrm{d}t \right\rangle + \frac{1}{r} \left\langle \frac{1}{r}\frac{\partial \psi_0}{\partial \theta} \int \frac{1}{r}\frac{\partial \psi_0}{\partial \theta} \mathrm{d}t \right\rangle \quad \text{on} \quad r = 1 \\ &= -\frac{1}{r}\frac{\partial}{\partial \theta} \left\langle \frac{\partial \psi_0}{\partial r} \int \frac{1}{r}\frac{\partial \psi_0}{\partial \theta} \mathrm{d}t \right\rangle \quad \text{on} \quad r = 1, \end{aligned} \qquad (A.6)$$

where we have used (A.5) and the identity $\left\langle A \int A \mathrm{d}t \right\rangle = 0$ for any A of the form $A(\boldsymbol{x}, t) = B(\boldsymbol{x})\mathrm{e}^{\mathrm{i}t}$. From the definition of the Stokes drift ψ_d (3.6), it is clear that it exactly compensates (A.6) at the mean position of the interface, i.e.

$$\frac{1}{r}\frac{\partial \langle \psi_1 \rangle}{\partial \theta} = -\frac{1}{r}\frac{\partial \psi_d}{\partial \theta} \quad \text{on} \quad r = 1.$$

For the stress boundary condition, the time average of the $O(\epsilon^2$ terms (A.4) directly yields

$$\left(\frac{\partial^2}{\partial r^2}-\frac{1}{r}\frac{\partial}{\partial r}-\frac{1}{r^2}\frac{\partial^2}{\partial\theta^2}\right)\langle\psi_1\rangle=\frac{1}{r}\left\langle\frac{4}{r}\frac{\partial}{\partial r}\left(\frac{1}{r}\frac{\partial\psi_0}{\partial\theta}\right)\int\frac{\partial^2\psi_0}{\partial\theta^2}\mathrm{d}t\right.$$
$$\left.-\frac{\partial}{\partial r}\left(\frac{\partial^2\psi_0}{\partial r^2}-\frac{1}{r}\frac{\partial\psi_0}{\partial r}-\frac{1}{r^2}\frac{\partial^2\psi_0}{\partial\theta^2}\right)\int\frac{\partial\psi_0}{\partial\theta}\mathrm{d}t\right\rangle\quad\text{on}\quad r=1. \tag{A.7}$$

It is also relatively straightforward to show using the definition of the Stokes drift and (A.5) that

$$\left(\frac{\partial^2}{\partial r^2}-\frac{1}{r}\frac{\partial}{\partial r}-\frac{1}{r^2}\frac{\partial^2}{\partial\theta^2}\right)\psi_d=\frac{1}{r}\left\langle-\frac{4}{r^2}\frac{\partial^2\psi_0}{\partial r\partial\theta}\int\frac{\partial^2\psi_0}{\partial\theta^2}\mathrm{d}t\right.$$
$$\left.+\left(\frac{\partial^3\psi_0}{\partial r^3}-\frac{3}{r^3}\frac{\partial^2\psi_0}{\partial\theta^2}-\frac{1}{r^2}\frac{\partial^3\psi_0}{\partial r\partial^2\theta}\right)\int\frac{\partial\psi_0}{\partial\theta}\mathrm{d}t\right\rangle\quad\text{on}\quad r=1. \tag{A.8}$$

Combining (A.7) and (A.8), one finds after some algebra that

$$\left(\frac{\partial^2}{\partial r^2}-\frac{1}{r}\frac{\partial}{\partial r}-\frac{1}{r^2}\frac{\partial^2}{\partial\theta^2}\right)(\langle\psi_1\rangle+\psi_d)=-\frac{4}{r^4}\left\langle\frac{\partial\psi}{\partial\theta}\oint\frac{\partial^2\psi}{\partial\theta^2}\,\mathrm{d}t+\frac{\partial^2\psi}{\partial\theta^2}\oint\frac{\partial\psi}{\partial\theta}\,\mathrm{d}t\right\rangle\quad\text{on}\quad r=1, \tag{A.9}$$

which vanishes identically due to the identity $\left\langle A\int B\mathrm{d}t+B\int A\mathrm{d}t\right\rangle=0$, valid for any oscillatory functions A and B. This establishes the homogeneous Lagrangian boundary conditions (3.7), namely.

$$\left.\begin{aligned}&\frac{1}{r}\frac{\partial\Psi}{\partial\theta}=0\\&\left(\frac{\partial^2}{\partial r^2}-\frac{1}{r}\frac{\partial}{\partial r}-\frac{1}{r^2}\frac{\partial^2}{\partial\theta^2}\right)\Psi=0\end{aligned}\right\}\quad\text{on}\quad r=1, \tag{A.10}$$

for streaming flows in the plane driven by a circular object for any arbitrary deformation of its interface. The analysis presented here is more general than that of analysis of [47]. We conjecture that similar homogeneous Lagrangian boundary conditions (vanishing normal velocity and tangential stress) hold for streaming driven by arbitrary 3D deformations of a cylindrical interface.

Appendix B

Surface mode contributions to the steady streaming

Here we derive expressions for (i) the particular solution to the Eulerian mean flow and (ii) the Stokes drift due to surface mode oscillations of the bubble. We focus our attention on the region of the flow that excludes the wall boundary layer solution, but include the bubble boundary layer as well as the volume outside of both these layers. We show that in general, the Eulerian particular solution and Stokes drift compensate exactly to leading order in the boundary layer thickness δ, making it necessary to retain bubble boundary terms of $O(\delta^2)$ in order to accurately assess the Lagrangian boundary flow. The analysis of the present chapter results in (3.16), which is then used to compute the steady streaming solutions in chapter 3.

B.1 Eulerian steady solution

Recall that the Eulerian steady streamfunction satisfies the following equation

$$\nabla^4 \langle \psi_1 \rangle = -\frac{2}{\delta^2} \left\langle \frac{1}{r} \frac{\partial(\psi_0, \nabla^2 \psi_0)}{\partial(r, \theta)} \right\rangle . \tag{B.1}$$

The right hand side of this equation, call if f, is confined to boundary layers due to the boundary layer character of $\nabla^2 \psi_0$. In general, $\langle \psi_1 \rangle$ may be written as a linear superposition of a particular solution $\langle \psi_p \rangle$ (satisfying (B.1)) and a homogeneous solution ψ_{hom} (satisfying $\nabla^4 \psi_{hom} = 0$); we focus here on the particular solution $\langle \psi_p \rangle$.

The oscillatory stream function ψ_0 itself may be written in as a linear combination of some modes $\psi_0^m(r, \theta)$ (see equations 3.10, 2.28), so that f, being quadratic in ψ_0, in general involves a linear superposition of products of modes, say ψ_0^m and ψ_0^n, and their spatial derivatives. It is then

appropriate to define a stream function ${}_m\langle\psi_p\rangle_n$ as the particular solution of

$$\nabla^4 {}_m\langle\psi_p\rangle_n = -\frac{2}{\delta^2}\left\langle \frac{1}{r}\frac{\partial(\psi_0^m, \nabla^2\psi_0^n)}{\partial(r,\theta)}\right\rangle. \tag{B.2}$$

Note the asymmetry between m and n in the above definition. The right hand side of (B.2), call it ${}_m f_n$, is evaluated using ψ_0 given by (3.10), and the time average evaluated using the identity

$$\left\langle \mathrm{Re}(P\mathrm{e}^{it})\mathrm{Re}(Q\mathrm{e}^{it})\right\rangle = \frac{1}{2}\mathrm{Re}(P^*Q) = \frac{1}{2}\mathrm{Re}(PQ^*),$$

where the asterisk represents a complex conjugate.

We exploit the boundary layer character of ${}_m f_n$ for $\delta \ll 1$, and write it in terms of an expansion into a bubble boundary layer coordinate $\eta \equiv (r-1)/\delta$, which simplifies the analysis considerably. It is relatively straightforward to show that such an expansion yields

$$\begin{aligned} {}_m f_n =& \overline{a}_m\overline{a}_n \mathrm{e}^{\mathrm{i}\phi_{n,m}}\frac{(2n+1)\mathrm{e}^{-(1+\mathrm{i})\eta}}{\delta^4}\Big[2\delta(1+\mathrm{i})\cos 2m\theta \sin 2n\theta \\ &- \delta^2\left\{3+(1+\mathrm{i})(4m+3)\eta\right\}\cos 2m\theta\sin 2n\theta - 4n\delta^2\cos 2n\theta\sin 2m\theta\Big] + O(\delta^3) \end{aligned} \tag{B.3}$$

where $\phi_{n,m} \equiv \phi_n - \phi_m$ is the phase difference between modes n and m. In order to solve (B.2), it is convenient to rewrite

$${}_m f_n = {}_m f_n^+ \sin 2(m+n)\theta + {}_m f_n^- \sin 2(m-n)\theta,$$

where

$${}_m f_n^+ = \overline{a}_m\overline{a}_n \mathrm{e}^{\mathrm{i}\phi_{n,m}}\frac{(2n+1)\mathrm{e}^{-(1+\mathrm{i})\eta}}{\delta^4}\left[(1+\mathrm{i})\delta - 2n\delta^2 - \frac{\delta^2}{2}\left\{3+(1+\mathrm{i})(4m+3)\eta\right\}\right] \tag{B.4}$$

$${}_m f_n^- = \overline{a}_m\overline{a}_n \mathrm{e}^{\mathrm{i}\phi_{n,m}}\frac{(2n+1)\mathrm{e}^{-(1+\mathrm{i})\eta}}{\delta^4}\left[-(1+\mathrm{i})\delta - 2n\delta^2 + \frac{\delta^2}{2}\left\{3+(1+\mathrm{i})(4m+3)\eta\right\}\right] \tag{B.5}$$

It is straightforward to see that the particular solution of (B.1) whose right hand side has the form $f(r)\sin k\theta$ is of the form $g(r)\sin k\theta$. The particular solution to (B.2) may therefore be

expressed as

$$ {}_m\langle\psi_p\rangle_n = {}_m\langle\psi_p\rangle_n^+ \sin 2(m+n)\theta + {}_m\langle\psi_p\rangle_n^- \sin 2(m-n)\theta, $$

where ${}_m\langle\psi_p\rangle_n^+(\eta)$ and ${}_m\langle\psi_p\rangle_n^-(\eta)$ are radial functions of solutions corresponding to the forcing terms ${}_m f_n^+ \sin 2(m+n)\theta$ and ${}_m f_n^- \sin 2(m-n)\theta$ respectively.

The functions ${}_m\langle\psi_p\rangle_n^+(\eta)$ and ${}_m\langle\psi_p\rangle_n^-(\eta)$ are obtained by expanding the biharmonic operator (the left hand side of (B.2)) within the bubble boundary layer coordinate, which has the form

$$ \nabla^4 = \frac{1}{\delta^4}\left(\frac{\partial^4}{\partial\eta^4} + 2\delta\frac{\partial^3}{\partial\eta^3}\right) + O(\delta^{-2}). $$

This results in the simple ordinary differential equations

$$ \left(\frac{\mathrm{d}^4}{\mathrm{d}\eta^4} + 2\delta\frac{\mathrm{d}^3}{\mathrm{d}\eta^3}\right) {}_m\langle\psi_p\rangle_n^{\pm}(\eta) = \delta^4 {}_m f_n^{\pm}(\eta), $$

which yield solutions, accurate to $O(\delta^2)$, of the form

$$ {}_m\langle\psi_p\rangle_n^+ = \overline{a}_m\overline{a}_n \mathrm{e}^{\mathrm{i}\phi_{n,m}}(2n+1)\mathrm{e}^{-(1+\mathrm{i})\eta}\left[-\frac{1+\mathrm{i}}{4}\delta + \frac{\delta^2}{8}\left\{11+16m+4n+(1+\mathrm{i})(4m+3)\eta\right\}\right], \tag{B.6} $$

$$ {}_m\langle\psi_p\rangle_n^- = \overline{a}_m\overline{a}_n \mathrm{e}^{\mathrm{i}\phi_{n,m}}(2n+1)\mathrm{e}^{-(1+\mathrm{i})\eta}\left[\frac{1+\mathrm{i}}{4}\delta - \frac{\delta^2}{8}\left\{11+16m-4n+(1+\mathrm{i})(4m+3)\eta\right\}\right]. \tag{B.7} $$

The particular solution to (B.1) is the superposition

$$ \langle\psi_p\rangle = \sum_{m=0}^{\infty}\sum_{n=0}^{\infty} {}_m\langle\psi_p\rangle_n^+ \sin 2(m+n)\theta + {}_m\langle\psi_p\rangle_n^- \sin 2(m-n)\theta. \tag{B.8} $$

Notice that we have retained terms up to $O(\delta^2)$ in (B.6) and (B.7), which as we will show, play an crucial role in determining the boundary conditions at the interface.

B.2 Stokes drift inside and outside the bubble boundary layer

We now derive explicit expressions for the stokes drift, which is in general defined as

$$\psi_d = \left\langle \frac{1}{r}\frac{\partial \psi_0}{\partial \theta}\int -\frac{\partial \psi_0}{\partial r}\mathrm{d}t \right\rangle. \tag{B.9}$$

The Stokes drift in general consists of both exponentially decaying terms (boundary layers), but also in general more slowly decaying terms which persist beyond these boundary layers. It is again useful to consider the Stokes drift due to two oscillatory modes m and n, which we define as

$${}_m\langle \psi_d \rangle_n \equiv \left\langle \frac{1}{r}\frac{\partial \psi_0^m}{\partial \theta}\int -\frac{\partial \psi_0^n}{\partial r}\mathrm{d}t \right\rangle = \frac{\mathrm{i}}{2r}\left(\frac{\partial \psi_0^m}{\partial \theta}\right)^* \frac{\partial \psi_0^n}{\partial r} \tag{B.10}$$

where the real part is implied. The Stokes drift ψ_d is given by a superposition over m and n of ${}_m\langle \psi_d \rangle_n$.

Retaining the coordinate r for algebraically decaying quantities and η for boundary layer quantities, ${}_m\langle \psi_d \rangle_n$ may be written in a series expansion in δ as

$$\begin{aligned} {}_m\langle \psi_d \rangle_n = \overline{a}_m \overline{a}_n \mathrm{e}^{\mathrm{i}\phi_{n,m}} \Bigg[& \frac{-\mathrm{i}}{2r^{2(m+n+1)}} - \frac{\delta^2}{2}\mathrm{e}^{-(1-\mathrm{i})\eta} 2m(2m+1) \\ & + \mathrm{e}^{-(1+\mathrm{i})\eta}(2n+1)\left\{ \frac{1+\mathrm{i}}{2}\delta - \frac{\delta^2}{4}\left\{3 + (1+i)(4m+3)\eta\right\}\right\}\Bigg] \cos 2m\theta \sin 2n\theta \\ & + O\left(\delta^3 \mathrm{e}^{-(1\pm\mathrm{i})\eta}, \delta r^{-2(m+n+1)}\right). \end{aligned} \tag{B.11}$$

Note that we have retained only the leading order $O(1)$ algebraic term, but have included upto $O(\delta^2)$ boundary layer terms. This is ultimately necessary to apply velocity and stress conditions at the interface. It will again prove convenient to rewrite

$${}_m\langle \psi_d \rangle_n = {}_m\langle \psi_d \rangle_n^+ \sin 2(m+n)\theta + {}_m\langle \psi_d \rangle_n^- \sin 2(m-n)\theta,$$

where

$$ {}_m\langle\psi_d\rangle_n^+ = -\,{}_m\langle\psi_d\rangle_n^- = \overline{a}_m\overline{a}_n \mathrm{e}^{\mathrm{i}\phi_{n,m}}\left[\frac{-\mathrm{i}}{4r^{2(m+n+1)}} - \frac{\delta^2}{4}\mathrm{e}^{-(1-\mathrm{i})\eta}2m(2m+1)\right. $$
$$ \left. + \mathrm{e}^{-(1+\mathrm{i})\eta}(2n+1)\left\{\frac{1+\mathrm{i}}{4}\delta - \frac{\delta^2}{8}\left\{3+(1+\mathrm{i})(4m+3)\eta\right\}\right\}\right] \tag{B.12} $$

The Stokes drift stream function is given by

$$ \psi_d = \sum_{m=0}^{\infty}\sum_{n=0}^{\infty} {}_m\langle\psi_d\rangle_n^+ \sin 2(m+n)\theta + {}_m\langle\psi_d\rangle_n^- \sin 2(m-n)\theta \tag{B.13} $$

B.3 Lagrangian steady streaming

We are now in a position to compute the Lagrangian streaming due to the combination of the particular solution part of the Eulerian streaming and the Stokes drift. The Lagrangian streaming is therefore in general written using the superposition

$$ \Psi = \sum_{m=0}^{\infty}\sum_{n=0}^{\infty} {}_m\Psi_n^+ \sin 2(m+n)\theta + {}_m\Psi_n^- \sin 2(m-n)\theta, \tag{B.14} $$

where

$$ {}_m\Psi_n^\pm = {}_m\langle\psi_p\rangle_n^\pm + {}_m\langle\psi_d\rangle_n^\pm . $$

Using equations (B.6), (B.7) and (B.12), one finds that

$$ {}_m\Psi_n^+ = \overline{a}_m\overline{a}_n\left[\frac{-\mathrm{i}\,\mathrm{e}^{\mathrm{i}\phi_{n,m}}}{4r^{2(m+n+1)}} + \delta^2\mathrm{e}^{-(1+\mathrm{i})\eta}(2m+1)(2n+1)\mathrm{e}^{\mathrm{i}\phi_{n,m}}\right. $$
$$ \left. + \frac{\delta^2}{4}\mathrm{e}^{-(1+\mathrm{i})\eta}\left\{2n(2n+1)\mathrm{e}^{\mathrm{i}\phi_{n,m}} - 2m(2m+1)\mathrm{e}^{-\mathrm{i}\phi_{n,m}}\right\}\right] \tag{B.15} $$

$$ {}_m\Psi_n^- = \overline{a}_m\overline{a}_n\left[\frac{\mathrm{i}\,\mathrm{e}^{\mathrm{i}\phi_{n,m}}}{4r^{2(m+n+1)}} - \delta^2\mathrm{e}^{-(1+\mathrm{i})\eta}(2m+1)(2n+1)\mathrm{e}^{\mathrm{i}\phi_{n,m}}\right. $$
$$ \left. + \frac{\delta^2}{4}\mathrm{e}^{-(1+\mathrm{i})\eta}\left\{2n(2n+1)\mathrm{e}^{\mathrm{i}\phi_{n,m}} + 2m(2m+1)\mathrm{e}^{-\mathrm{i}\phi_{n,m}}\right\}\right]. \tag{B.16} $$

Notice that the boundary layer terms at $O(\delta)$ from the Eulerian particular solution and the Stokes drift compensate exactly, so that the leading order bubble boundary layer terms in the Lagrangian streaming are $O(\delta^2)$. While we may in principle stop the computation at this point, it is further

useful to consider the symmetric contribution of modes m and n to the Lagrangian streaming by defining

$$\Psi^+_{m,n} \equiv \frac{1}{1+\delta_{mn}}\left({}_m\Psi^+_n + {}_n\Psi^+_m\right) \quad \text{and} \quad \Psi^-_{m,n} \equiv \frac{1}{1+\delta_{mn}}\left({}_m\Psi^-_n - {}_n\Psi^-_m\right), \tag{B.17}$$

where δ_{mn} is the Kronecker delta, so that one may rewrite (B.14) equivalently as

$$\Psi = \sum_{m\geq n}^{\infty}\sum_{n=0}^{\infty} \Psi^+_{m,n}\sin 2(m+n)\theta + \Psi^-_{m,n}\sin 2(m-n)\theta. \tag{B.18}$$

Using (B.15), one obtains the simple expressions

$$\Psi^+_{m,n} = \frac{\overline{a}_m\overline{a}_n}{1+\delta_{mn}} 2\delta^2\,(2m+1)(2n+1)\cos\phi_{m,n}\,\mathrm{e}^{-(1+\mathrm{i})\eta} \quad \text{and} \tag{B.19}$$

$$\Psi^-_{m,n} = \overline{a}_m\overline{a}_n\left\{\frac{1}{2r^{2(m+n+1)}} + 2\mathrm{i}\,\delta^2(2m+1)(2n+1)\,\mathrm{e}^{-(1+\mathrm{i})\eta}\right\}\sin\phi_{m,n}. \tag{B.20}$$

The algebraically decaying terms are due to the Stokes drift and are proportional to the sine of the phase difference between modes $\sin\phi_{m,n} \neq 0$ and only appear in $\Psi^-_{m,n}$ terms. The Stokes drift terms not only persist in the far field, but are also required to determine the homogeneous streaming solutions through bubble boundary conditions. To leading order, boundary layer terms are $O(\delta^2)$ and therefore do not contribute to the velocity field (at leading order), but result in $O(1)$ stress components and are important to the stress conditions. Further, it is easy to see that tangential stresses due to $\Psi^+_{m,n}$, given to leading order in δ by $\delta^{-2}\partial^2_\eta\Psi^+_{m,n}$, are purely imaginary at $r=1$, and are therefore not contribute in any physically meaningful way to the flow (recall that only the real part of any physical quantity is meaningful in the analysis).

The analysis therefore shows that the streaming due to the bubble boundary layer is entirely governed by "mixed-mode" contributions $\Psi^-_{m,n}$, which are only non-zero for $m \neq n$ (note that this is not true of contributions due to the wall boundary layer). The expressions obtained here are generalizations of the results obtained by Longuet Higgins for a spherical bubble. The combined contribution of mode pairs to the streaming, which may now be written as

$$\Psi^- = \sum_{m>n}^{\infty}\sum_{n=0} \Psi^-_{m,n}\sin 2(m-n)\theta,$$

feed into the expression (3.16) for the Lagrangian outer flow.

B.4 Conclusions

The analysis presented here is valid generally for any combination of 2D surface mode oscillations over a no-stress sessile bubble of semi-cylindrical shape. We have made use of the criterion that the boundary layer thickness is small compared to the bubble, allowing us to treat the bubble boundary layer independently of the no-slip wall boundary layer which play a role near the contact lines between the bubble and the wall. The analysis is therefore formally valid for descriptions of surface mode excitation of a 2D bubble of cylindrical shape (circular in cross-section), i.e. in the absence of contact lines. A similar analysis of the streaming may be carried out for different boundary conditions (e.g. a no-slip bubble) or for other geometries (e.g. a hemispherical bubble), provided that the oscillatory flow functions used are appropriately modified.

Appendix C

Some interesting properties of closed 2D streamlines

C.1 Fluid orbits near an elliptic point

We provide here a general result on the kinematic of fluid motion in the vicinity of an elliptic stagnation point, which may be either interpreted as a closed streamline of vanishing area, or equivalently as the vortex center of a 2D vortex.

In the vicinity of any stagnation point (vanishing fluid velocity), the stream function ψ governing a steady 2D flow may be written in terms of an expansion

$$\psi(x,y) = \psi_0 + \frac{1}{2}\partial_x^2\psi_0(x-x_0)^2 + \frac{1}{2}\partial_y^2\psi_0(y-y_0)^2 + \partial_x\partial_y\psi_0(x-x_0)(y-y_0).$$

It is convenient to rewrite the above equation as

$$\Psi(X,Y) = aX^2 + bY^2 + cXY \tag{C.1}$$

where $\Psi = \psi - \psi_0$, $a = \frac{1}{2}\partial_x^2\psi_0$, $b = \frac{1}{2}\partial_y^2\psi_0$ and $c = \partial_x\partial_y\psi_0$. Equation (C.1) describes a family of elliptical streamlines of constant aspect ratio, which may be written in standard form using the coordinate transform $(X,Y) \mapsto (\xi,\eta)$, defined by a rotation through an angle λ:

$$X = \xi\cos\lambda - \eta\sin\lambda; \quad Y = \xi\sin\lambda + \eta\cos\lambda.$$

If one chooses $\tan 2\lambda = c/(a-b)$, the equation for the streamlines in the transformed coordinates becomes

$$\Psi(\xi,\eta) = \frac{\xi^2}{\alpha^2} + \frac{\eta^2}{\beta^2}, \tag{C.2}$$

where

$$\frac{1}{\alpha^2} \equiv \frac{1}{2}\left(a + b + \frac{c}{\sin 2\lambda}\right), \quad \frac{1}{\beta^2} \equiv \frac{1}{2}\left(a + b - \frac{c}{\sin 2\lambda}\right).$$

In parametric form, (C.2) may be written as

$$\xi = \alpha\sqrt{\Psi}\cos\varphi, \quad \eta = \beta\sqrt{\Psi}\sin\varphi, \tag{C.3}$$

where φ is the azimuthal position of the point (ξ, η) with respect to the ξ axis. The velocity components are just

$$u_\xi = \partial_\eta \Psi = \frac{2\sqrt{\Psi}}{\beta}\sin\varphi, \quad u_\eta = -\partial_\xi \Psi = -\frac{2\sqrt{\Psi}}{\alpha}\cos\varphi \tag{C.4}$$

The equations of motion of a fluid particle on a streamline given by a constant value of Ψ are then $\dot{\xi} = u_\xi$ and $\dot{\eta} = u_\eta$, both of which yield the dynamic equation for the evolution of φ:

$$\dot{\varphi} = -\frac{2}{\alpha\beta}, \tag{C.5}$$

which is independent of both Ψ and φ and therefore represents a constant angular frequency $\Omega = 2/(\alpha\beta)$. The orbit time along a streamline is readily calculated as $T = 2\pi/\Omega$, which is also independent of Ψ. Using the expressions for α and β in terms of the gradients of $\psi(x, y)$, one may compute

$$\Omega = \sqrt{\partial_x^2\psi_0\,\partial_y^2\psi_0 - (\partial_x\partial_y\psi_0)^2}, \tag{C.6}$$

which is exactly the square root of the local Gaussian curvature of the surface $\psi(x, y)$ at the elliptic point (x_0, y_0). It is somewhat surprising that fluid elements on streamlines that are arbitrarily close to the elliptic stagnation point have nonzero orbit times.

C.2 General Hamiltonian formalism for perturbed 2D vortical flows

We present here a proof of the continuity equation (4.26) in ψ-z space, valid for small perturbations $\boldsymbol{v}$ of an incompressible 2D flow $\boldsymbol{u}$ characterized by closed streamlines. This automatically yields the Hamiltonian structure of the 3D motion (4.27), governed by the Hamiltonian $\mathcal{H}(\psi, z)$ defined in (4.28).

Consider a steady flow superposition of the form

$$\boldsymbol{U}(x, y, z) = \boldsymbol{u}(x, y) + \boldsymbol{v}(x, y, z).$$

where $\boldsymbol{u}$ and $\boldsymbol{v}$ are both incompressible fields, and it is assumed that $|\boldsymbol{v}| \ll |\boldsymbol{u}|$. By virtue of incompressibility, one may express $\boldsymbol{u}$ in terms of a stream function ψ, which we assume is characterized by closed streamlines (lines of constant ψ), concentric about a vortex center $\psi = \psi_m$.

If $\boldsymbol{v}$ only slightly perturbs the 2D fluid motion due to $\boldsymbol{u}$, appropriate to compute the motion of a fluid element by means of a perturbative expansion, so that to leading order, the position of a fluid element is given by

$$\frac{\mathrm{d}\tilde{\boldsymbol{x}}(t)}{\mathrm{d}t} = \boldsymbol{u}(\tilde{\boldsymbol{x}}(t)).$$

This is the equation of motion for the 2D flow, i.e. $\tilde{x}$ represents a motion along constant ψ, z, valid to leading order over *short times*, as discussed in section 4.4.2. It is useful under this approximation to define a differential arclength element $\mathrm{d}s = |\boldsymbol{u}|\mathrm{d}t = |\nabla\psi|\mathrm{d}t$, and a local unit outward normal $\boldsymbol{n}$, given for counterclockwise flow by $\boldsymbol{n} \equiv -\nabla\psi/|\nabla\psi|$. The drift of some field $f(\boldsymbol{x})$ sampled by the particle during its motion through a time τ, is then given by

$$\Delta f \equiv \int^{\tau} \boldsymbol{U}(\boldsymbol{x}(t)) \cdot \boldsymbol{\nabla} f(\boldsymbol{x}(t))\,\mathrm{d}t = \int^{\tau} \boldsymbol{U}(\tilde{\boldsymbol{x}}(t)) \cdot \boldsymbol{\nabla} f(\tilde{\boldsymbol{x}}(t))\,\mathrm{d}t + O(|\boldsymbol{x} - \tilde{\boldsymbol{x}}|) \tag{C.7}$$

In particular, we now consider the quantities $\Delta\psi$ and Δz over the time $\tau = T(\psi)$, where $T(\psi)$ is the orbit time of a fluid element around a streamline ψ. To leading order, time integration over $T(\psi)$ may be replaced by a path integral over a streamline ψ, according to (C.7), since $\boldsymbol{x} \approx \tilde{\boldsymbol{x}}$.

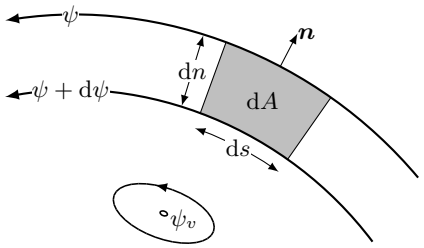

Figure C.1 Schematic showing the definitions used to compute the area enclosed between streamlines.

Using (C.7), definitions for $\mathrm{d}s$ and $\boldsymbol{n}$, and the divergence theorem, (4.25) for $\Delta\psi$ may be recast as

$$\Delta\psi(\psi, z) = -\int_0^{T(\psi)} \boldsymbol{v}\cdot\boldsymbol{n}|\nabla\psi|\mathrm{d}t = -\oint_\psi \boldsymbol{v}\cdot\boldsymbol{n}\,\mathrm{d}s = -\int_{A(\psi)} \nabla_2\cdot\boldsymbol{v}\,\mathrm{d}A, \tag{C.8}$$

where $A(\psi)$ is the area enclosed by a streamline ψ and ∇_2 is the 2D gradient operator in the xy plane. Note that $\boldsymbol{u}\cdot\nabla\psi$ is identically zero, so that $\boldsymbol{U}\cdot\nabla\psi = \boldsymbol{v}\cdot\nabla\psi$. The differential area element may in general be written as

$$\mathrm{d}A = \mathrm{d}s(\boldsymbol{n}\cdot\mathrm{d}\boldsymbol{x}).$$

For counterclockwise flow, the definitions for $\boldsymbol{n}$ and $\mathrm{d}s$ yield $\mathrm{d}A = -\mathrm{d}t\mathrm{d}\psi$, allowing (C.8) to be written as

$$\Delta\psi(\psi, z) = \int_{\psi_m}^{\psi}\int_0^{T(\psi)} \nabla_2\cdot\boldsymbol{v}\,\mathrm{d}t\,\mathrm{d}\psi. \tag{C.9}$$

The drift of the z coordinate of a fluid element is to leading order

$$\Delta z(\psi, z) = \int_0^{T(\psi)} \boldsymbol{v}\cdot\nabla z\,\mathrm{d}t = \int_0^{T(\psi)} v_z\mathrm{d}t \tag{C.10}$$

It follows directly from definitions of $\Delta\psi$ (C.9) and Δz (C.10) that

$$\frac{\partial\Delta\psi}{\partial\psi} + \frac{\partial\Delta z}{\partial z} = \int_0^{T(\psi)} \left(\nabla_2\cdot\boldsymbol{v} + \frac{\partial v_z}{\partial z}\right)\mathrm{d}t = \int_0^{T(\psi)} \nabla\cdot\boldsymbol{v}\,\mathrm{d}t. \tag{C.11}$$

The integrand vanishes identically for incompressible flows $\boldsymbol{v}$, yielding the continuity equation (4.26) in the abstract ψ-z space, and consequently the Hamiltonian structure of the 3D transport, cf chapter 4. The derivation for a clockwise vortex follows similarly, bearing in mind that $\boldsymbol{n} = -\nabla\psi/|\nabla\psi|$ in this case represents the inward pointing normal. The expression (4.28) for the

Hamiltonian $\mathcal{H}(\psi, z)$ is obtained as $\mathcal{H} = \int \Delta\psi \mathrm{d}z$ using (4.27) and (C.8). It is worth noting that the Hamiltonian formalism developed here formally represents the leading order modification of 2D trajectories in the limit $|\boldsymbol{v}| \ll |\boldsymbol{u}|$. The description holds generally for arbitrary time-dependent perturbations $\boldsymbol{v}$, only requiring the condition of incompressibility.

Appendix D

Streaming near a sharp corner

We consider here the steady streaming flow in the vicinity of the vertex of a solid wedge surrounded by a viscous fluid, undergoing a primary oscillatory motion relative to the wedge. Such an oscillatory fluid motion may occur due to a number of different mechanisms that include, but are not limited to (i) the response of the fluid to an applied acoustic pressure field, (ii) oscillations of a compact object — such as a gas bubble — placed some distance from the wedge, or (iii) oscillations of the wedge itself.

Consider a rigid wedge subtending an angle 2α through the fluid at its vertex, as shown in figure D.1.

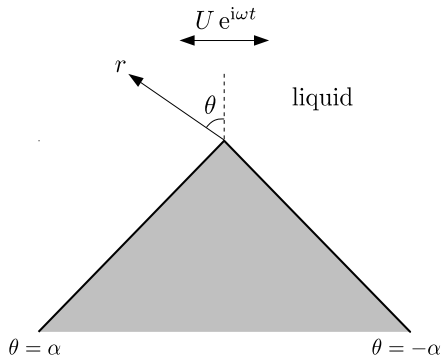

Figure D.1 Cross section of the wedge normal to the sharp edge, showing the coordinate system employed here and indicating oscillatory motion (horizontal in this example).

Irrespective of the actual mechanisms of driving involved, the wedge may be treated as being fixed, with the fluid oscillating about it at a characteristic speed U at the angular frequency ω of the driving. In practice, the characteristic length scale associated with gradients of the flow field is determined by the radius of curvature a wedge near the origin. In the present analysis, however, we will avoid resolving the particular geometric details of the solid boundary near the origin, in effect treating the vertex as being arbitrarily sharp, but retain the length scale a. It is then convenient

to attach a polar coordinate system (r, θ) to the vertex, as shown in D.1, so that fluid is contained within the 2D volume $0 < r < \infty$, $-\alpha < \theta < \alpha$.

We further assume that the wavelength of the driving and any geometric features capable of exciting flow or otherwise changing its structure are at distances from the origin much greater than a. This also permits the flow to be treated as two-dimensional in the r-θ plane.

Using characteristic scales U, a and ω^{-1} respectively as characteristic velocity, length and time scales, we introduce a dimensionless stream function $\psi(r, \theta, t)$, related to the radial and azimuthal velocities as $u = r^{-1}\partial_\theta \psi$ and $v = -\partial_r \psi$ respectively. The flow satisfies the Navier-Stokes equations, and no-slip conditions on the solid-boundary

$$\frac{\partial \psi}{\partial \theta} = \frac{\partial \psi}{\partial r} = 0 \quad \text{on} \quad \theta = 0 \quad \text{and} \quad \theta = \alpha, \tag{D.1}$$

D.1 Primary oscillatory flow

We employ the standard analysis for the primary and secondary flows described in chapters 2 and 3, valid in the limit of $\epsilon \equiv U/a\omega \ll 1$ and $\delta \equiv \sqrt{2\nu/a^2\omega} \ll 1$, where ν is the kinematic viscosity of the fluid. In the limit $\epsilon \ll 1$, an approximate solution may be obtained by the expansion $\psi = \psi_0 + \epsilon\psi_1 + O(\epsilon^2)$. At leading order in ϵ, the non-linear inertia term of the Navier-Stokes equations is negligible, so that the primary oscillatory flow is governed by the linear equation

$$\left(\frac{\partial}{\partial t} - \frac{\delta^2}{2}\nabla^2\right)\nabla^2\psi_0 = 0. \tag{D.2}$$

We focus on the oscillatory flow outside of the Stokes shear layers that are established near the solid boundary boundary, which satisfies

$$\nabla^2\psi_0 = 0 \quad \text{and}$$

and the no-penetration boundary condition

$$\psi_0(r, \theta = \pm\alpha) = 0.$$

The no-slip condition is accommodated by the oscillatory boundary layers that become established at the walls.

The system of equations (D.2, D.1) for the oscillatory flow represents not a unique solution (due to the absence of any inhomogeneities), but rather a space of solutions that is ultimately restricted by matching conditions at $r \to \infty$. While these "far-field" conditions may in general depend on the exact nature of the driving, it is not unreasonable to expect that in cases where the vertex is sufficiently isolated from other geometrical features, any agent driving the flow will result in an oscillatory flow that presents relatively "simple" matching conditions. We consider here an oscillatory potential flow of the form

$$\psi_0(r,\theta,t) = \left(a_1\,\mathrm{e}^{\mathrm{i}\phi_1}\psi^{(1)} + a_2\,\mathrm{e}^{\mathrm{i}\phi_2}\psi^{(2)}\right)\mathrm{e}^{\mathrm{i}t}, \tag{D.3}$$

where

$$\psi^{(1)} = \frac{1}{n}r^n\cos\,n\theta \quad \text{and} \quad \psi^{(2)} = \frac{1}{2n}r^{2n}\sin\,2n\theta \tag{D.4}$$

and $n \equiv \pi/2\alpha$ is a geometric parameter. a_j and ϕ_j are amplitudes and temporal phases respectively of the oscillatory flow functions $\psi^{(j)}$. The flow $\psi^{(1)}$ and $\psi^{(2)}$ correspond respectively to oscillations of the wedge that are respectively perpendicular and parallel to the $\theta = 0$ axis. We remark that for $n < 1$ ($\alpha > \pi$), the velocity field due to (D.3) diverges near the origin. This singularity, however, is a consequence of the sharp edge and can be regularized by a more detailed treatment of the geometry of the wedge near the origin [58].

The oscillatory slip velocity u_s driven over the wall at $\theta = 0$ is then

$$u_s(r,t) = \begin{cases} \left(a_1\,\mathrm{e}^{\mathrm{i}\phi_1}r^{-1+n} - a_2\,\mathrm{e}^{\mathrm{i}\phi_2}r^{-1+2n}\right)\mathrm{e}^{\mathrm{i}t}, & \text{on} \quad \theta = -\alpha \\ \left(-a_1\,\mathrm{e}^{\mathrm{i}\phi_1}r^{-1+n} - a_2\,\mathrm{e}^{\mathrm{i}\phi_2}r^{-1+2n}\right)\mathrm{e}^{\mathrm{i}t}, & \text{on} \quad \theta = \alpha \end{cases} \tag{D.5}$$

D.2 Steady streaming

This oscillatory slip is accommodated by and uniquely determines the oscillatory boundary layer, which has a thickness on the order of δ near the solid boundary and a well-known spatial structure [46]. The oscillatory boundary layer through (3.5) establishes a non-zero steady Reynolds stress,

which drives a steady (time averaged) slip velocity

$$U_s(r) = -\frac{3-5\mathrm{i}}{4} u_s^* \frac{\mathrm{d}u_s}{\mathrm{d}r} \tag{D.6}$$

where u_s^* represents the complex conjugate of u_s. Using (D.5), one finds

$$U_s = \begin{cases} U_s^{(1,1)} + U_s^{(2,2)} - U_s^{(1,2)}, & \text{on} \quad \theta = -\alpha \\ \\ U_s^{(1,1)} + U_s^{(2,2)} + U_s^{(1,2)}, & \text{on} \quad \theta = \alpha, \end{cases} \tag{D.7}$$

where

$$U_s^{(1,1)} = \frac{3}{4} a_1^2 (1-n)\, r^{2n-3}, \tag{D.8}$$

$$U_s^{(2,2)} = \frac{3}{4} a_2^2 (1-2n)\, r^{4n-3}, \tag{D.9}$$

$$U_s^{(1,2)} = \frac{1}{4} a_1 a_2\, r^{3n-3} \left(3(2-3n)\cos\phi_{2,1} - 5n \sin\phi_{2,1}\right) \tag{D.10}$$

and $\phi_{2,1} = \phi_2 - \phi_1$ is the phase difference between the oscillation modes. Note that in this case, self-interactions $U^{(1,1)}$ and $U^{(2,2)}$ result in symmetric slip along both walls $\theta = \pm\alpha$, whereas cross interactions result in anti-symmetric wall slip velocities.

In order to compute the Lagrangian steady streaming driven by the combination of modes, we first compute the Stokes drift (cf. (3.6)), as

$$\psi_d = \left\langle \frac{1}{r} \frac{\partial \psi_0}{\partial \theta} \int -\frac{\partial \psi_0}{\partial r} \mathrm{d}t \right\rangle = \frac{1}{2} a_1 a_2 \sin\phi_{2,1} r^{3n-2} \cos n\theta. \tag{D.11}$$

Note that the Stokes drift is non-zero only for mixed-mode contributions. The Lagrangian steady stream function outsside the wall boundary layer is then given by $\Psi = \langle \psi_1 \rangle + \psi_d$, where $\langle \psi_1 \rangle$ is the Eulerian stream function satisfying the biharmonic equation (Stokes flow)

$$\nabla^4 \langle \psi_1 \rangle = 0. \tag{D.12}$$

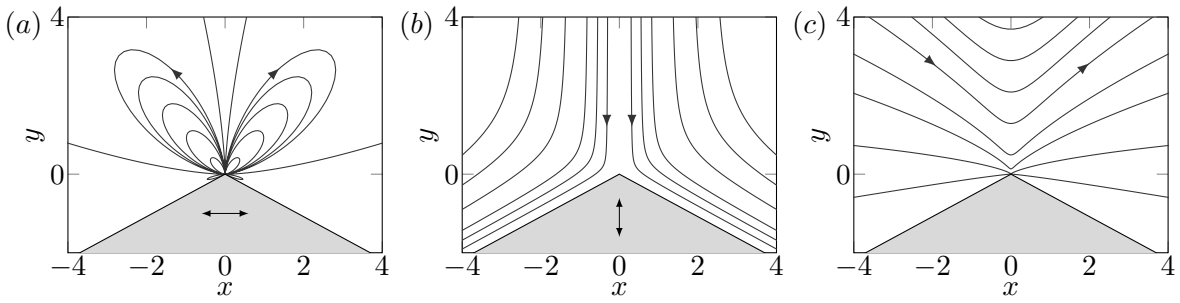

Figure D.2 Streamlines of steady Lagrangian flow for a wedge with $n = 0.76$ due to different flow contributions: (a) $\Psi^{(1,1)}$, (b) $\Psi^{(2,2)}$, and (c) $\Psi^{(1,2)}$ with $\phi_{2,1} = \pi/4$. The arrows indicate the direction of flow. The oscillatory motion of the wedge (shaded grey) is indicated by the double arrows in (a) and (b).

The Lagrangian mean flow satisfies the matching conditions at the walls

$$\left.\begin{aligned} \frac{1}{r}\frac{\partial \Psi}{\partial \theta} &= U_s(r) \\ \frac{\partial \Psi}{\partial r} &= 0 \end{aligned}\right\} \quad \text{on} \quad \theta = 0 \quad \text{and} \quad \theta = \pm\alpha. \tag{D.13}$$

The solution to the system of equations (D.12,D.13) is straightforward to obtain using a separation of variables. Since the slip conditions at the wall contain both symmetric and antisymmetric components, it is useful to consider these symmetries separately.

The Lagrangian streaming corresponding to the symmetric components of U_s, namely $U_s^{(j,j)}$ where $j \in \{1, 2\}$, have the form

$$\Psi^{(j,j)} = a_j^2 \frac{3}{8}(jn-1)\, r^{2(jn-1)} \left\{ b_n^{(j,j)} \sin 2(jn-1)\theta + c_n^{(j,j)} \sin 2(jn-2)\theta \right\}, \tag{D.14}$$

where

$$b_n^{(j,j)} = \frac{2\cos\frac{\pi}{n}}{\cos\frac{2\pi}{n} + jn - 1}, \quad \text{and} \tag{D.15}$$

$$c_n^{(j,j)} = -\frac{1}{\cos\frac{2\pi}{n} + jn - 1}. \tag{D.16}$$

The Lagrangian solution corresponding to the anti-symmetric component of U_s, i.e. $U_s^{(1,2)}$ is

given by

$$\Psi^{(1,2)} = a_1 a_2 r^{3n-2} \left\{ \frac{1}{2} \sin\phi_{2,1} \cos n\theta + b_n^{(1,2)} \cos(3n-2)\theta + c_n^{(1,2)} \cos(3n-4)\theta \right\}, \tag{D.17}$$

where

$$b_n^{(1,2)} = \frac{((-6+9n)\cos\phi_{2,1} + 7n\sin\phi_{2,1})\cos\frac{\pi}{n}}{4\cos\frac{2\pi}{n} + 6n - 4}, \quad \text{and} \tag{D.18}$$

$$c_n^{(1,2)} = -\frac{(-6+9n)\cos\phi_{2,1} + 7n\sin\phi_{2,1}}{2\left(4\cos\frac{2\pi}{n} + 6n - 4\right)}. \tag{D.19}$$

The steady flow field is given by the superposition

$$\Psi = \Psi^{(1,1)} + \Psi^{(2,2)} + \Psi^{(1,12)},$$

and is a function of the wedge angle (characterized by n), as well as the phase difference between the modes $\phi_{2,1}$. The individual contributions of the three streaming components are plotted in figure D.2 for the particular value of $n = 0.76$ and $\phi_{2,1} = \pi/4$. In general, the $\Psi^{(2,2)}$ component of the flow has the slowest decay and is expected to dominate in the far-field. The present theory indicates a radially inward flow towards the vertex of the wedge, which is qualitatively similar to the experimental and numerical results of [36] for streaming due to an oscillating cylinder of square cross-section.

For narrower wedges $n \approx 0.5$, the $\Psi^{(2,2)}$ component is only weakly excited (being proportional to $2n-1$) and the flow is therefore dominated either by $\Psi^{(1,1)}$ or $\Psi^{(1,2)}$. In particular, if the (a_1, ϕ_1) mode is the primary mode of oscillatory excitation, the flow field is given by $\Psi^{(1,1)}$, which results in a system of "fountain" vortices at the tip of the wedge. This is qualitatively similar to flows observed by Huang et al. [32] and Nama et al. [67]. The theory also predicts a reversal of the $\Psi^{(1,1)}$ flow to the anti-fountain orientation occurring at a critical $n = n_c \approx 0.548$ which is given by the smallest solution (such that $n_c > 0.5$) of the equation

$$\cos\frac{2\pi}{n_c} + n_c - 1 = 0.$$

D.3 Conclusions

We have developed a simple theory of streaming flows for translational oscillations of a solid wedge. Taken individually, oscillations of the wedge either along its symmetry plane or perpendicular to it drive streaming flows for which there is no transport of fluid across the plane. We show however, that a combination of these oscillation modes drives streaming of the opposite symmetry, viz. one with maximum velocity perpendicular to the symmetry plane, and whose direction depends not only on the wedge angle, but also the phase difference between the two oscillation modes.

The dependence of the flow on n and ϕ are both non-trivial; each of these quantities is individually capable of modifying the direction of the flow. This suggests the design of simple flow manipulation devices capable of a variety of flow fields simply by small changes in geometrical features or the phase of oscillatory motion.

References

[1] D. Ahmed, X. Mao, B. K. Juluri, and T. J. Huang. A fast microfluidic mixer based on acoustically driven sidewall-trapped microbubbles. *Microfluid. Nanofluid.*, 7:727–731, 2009. doi: 10.1007/s10404-009-0444-3.

[2] D. Ahmed, X. Mao, J. Shi, B. K. Juluri, and T. J. Huang. A millisecond micromixer via single-bubble-based acoustic streaming. *Lab Chip*, 9(18):2738–2741, 2009.

[3] R. Aris. On the dispersion of a solute in a fluid flowing through a tube. In *Proceedings of the Royal Society of London A: Mathematical, Physical and Engineering Sciences*, volume 235, pages 67–77. The Royal Society, 1956.

[4] D. J. Beebe, G. A. Mensing, and G. M. Walker. Physics and applications of microfluidics in biology. *Annu. Rev. Biomed. Eng.*, 4(1):261–286, 2002.

[5] A. Bertelsen, A. Svardal, and S. Tjøtta. Nonlinear streaming effects associated with oscillating cylinders. *J. Fluid Mech.*, 59(03):493–511, 1973.

[6] W. Brown, Z. Pu, and R. Rymden. Size and shape of nonionic amphiphile micelles: Nmr self-diffusion and static and quasi-elastic light-scattering measurements on c12e5, c12e7, and c12e8 in aqueous solution. *The Journal of Physical Chemistry*, 92(21):6086–6094, 1988.

[7] K. Chong, S. D. Kelly, S. Smith, and J. D. Eldredge. Inertial particle trapping in viscous streaming. *Phys. Fluids*, 25(3):033602, 2013.

[8] C. Cierpka and C. J. Kähler. Particle imaging techniques for volumetric three-component (3D3C) velocity measurements in microfluidics. *J. Vis.*, 15(1):1–31, 2012.

[9] C. Cierpka, M. Rossi, R. Segura, and C. J. Kähler. On the calibration of astigmatism particle tracking velocimetry for microflows. *Meas. Sci. Technol.*, 22(1):015401, 2011.

[10] L. Cortelezzi, A. Adrover, and M. Giona. Feasibility, efficiency and transportability of short-horizon optimal mixing protocols. *Journal of Fluid Mechanics*, 597:199–231, 2008.

[11] B. J. Davidson and N. Riley. Cavitation microstreaming. *J. Sound Vib.*, 15:217–233, 1971.

[12] J. De Jong, R. Lammertink, and M. Wessling. Membranes and microfluidics: a review. *Lab Chip*, 6(9):1125–1139, 2006.

[13] A. A. Doinikov. Acoustic radiation force on a spherical particle in a viscous heat-conducting fluid. I. general formula. *J. Acoust. Soc. Amer.*, 101(2):713–721, 1997.

[14] A. A. Doinikov and A. Bouakaz. Acoustic microstreaming around a gas bubble. *J. Acoust. Soc. Amer.*, 127(2):703–709, 2010. doi: 10.1121/1.3279793. URL `http://link.aip.org/link/?JAS/127/703/1`.

[15] A. A. Doinikov and A. Bouakaz. Effect of a distant rigid wall on microstreaming generated by an acoustically driven gas bubble. *Journal of Fluid Mechanics*, 742:425–445, 2014.

[16] J. C. Eijkel and A. Van Den Berg. Nanofluidics: what is it and what can we expect from it? *Microfluidics and Nanofluidics*, 1(3):249–267, 2005.

[17] S. A. Elder. Cavitation microstreaming. *J. Acoust. Soc. Am.*, 31(1):54–64, 1959. doi: 10.1121/1.1907611. URL `http://link.aip.org/link/?JAS/31/54/1`.

[18] I. Fayzrakhmanova, A. Straube, and S. Shklyaev. Bubble dynamics atop an oscillating substrate: Interplay of compressibility and contact angle hysteresis. *Phys. Fluids*, 23(10):102105, 2011.

[19] P. F. Fischer, G. K. Leaf, and J. M. Restrepo. Forces on particles in oscillatory boundary layers. *Journal of Fluid Mechanics*, 468:327–347, 2002.

[20] T. Franke, A. R. Abate, D. A. Weitz, and A. Wixforth. Surface acoustic wave (SAW) directed droplet flow in microfluidics for pdms devices. *Lab Chip*, 9:2625–2627, 2009. doi: 10.1039/B906819H. URL `http://dx.doi.org/10.1039/B906819H`.

[21] T. Franke, S. Braunmüller, L. Schmid, A. Wixforth, and D. Weitz. Surface acoustic wave actuated cell sorting (SAWACS). *Lab Chip*, 10(6):789–794, 2010.

[22] J. Friend and L. Yeo. Microscale acoustofluidics: Microfluidics driven via acoustics and ultrasonics. *Rev. Mod. Phys.*, 83(2):647–704, 2011.

[23] H. Gelderblom, A. G. Zijlstra, L. van Wijngaarden, and A. Prosperetti. Oscillations of a gas pocket on a liquid-covered solid surface. *Phys. Fluids*, 24(12):122101, 2012.

[24] P. Gravesen, J. Branebjerg, and O. S. Jensen. Microfluidics-a review. *J. Micromech. Microeng.*, 3(4):168, 1993.

[25] O. Gubanov and L. Cortelezzi. Towards the design of an optimal mixer. *Journal of Fluid Mechanics*, 651:27–53, 2010.

[26] J. Guckenheimer and P. Holmes. *Nonlinear oscillations, dynamical systems, and bifurcations of vector fields*, volume 42. Springer Science & Business Media, 1983.

[27] S. Hilgenfeldt, D. Lohse, and M. Brenner. Phase diagrams for sonoluminescing bubbles. *Phys. Fluids*, 8:2808, 1996.

[28] B. Ho and L. Leal. Inertial migration of rigid spheres in two-dimensional unidirectional flows. *Journal of fluid mechanics*, 65(02):365–400, 1974.

[29] A. J. Hogg. The inertial migration of non-neutrally buoyant spherical particles in two-dimensional shear flows. *Journal of Fluid Mechanics*, 272:285–318, 1994.

[30] J. Holtsmark, I. Johnsen, T. Sikkeland, and S. Skavlem. Boundary layer flow near a cylindrical obstacle in an oscillating, incompressible fluid. *J. Acoust. Soc. Amer.*, 26(1):26–39, 1954.

[31] K. Hood, S. Lee, and M. Roper. Inertial migration of a rigid sphere in three-dimensional poiseuille flow. *Journal of Fluid Mechanics*, 765:452–479, 2015.

[32] P.-H. Huang, Y. Xie, D. Ahmed, J. Rufo, N. Nama, Y. Chen, C. Y. Chan, and T. J. Huang. An acoustofluidic micromixer based on oscillating sidewall sharp-edges. *Lab on a Chip*, 13 (19):3847–3852, 2013.

[33] M. IanáLapsley, I. KaoáChiang, Y. BingáZheng, T. JunáHuang, et al. A single-layer, planar, optofluidic mach–zehnder interferometer for label-free detection. *Lab on a Chip*, 11(10):1795–1800, 2011.

[34] R. F. Ismagilov, A. D. Stroock, P. J. Kenis, G. Whitesides, and H. A. Stone. Experimental and theoretical scaling laws for transverse diffusive broadening in two-phase laminar flows in microchannels. *Applied Physics Letters*, 76(17):2376–2378, 2000.

[35] M. Kakuta, F. G. Bessoth, and A. Manz. Microfabricated devices for fluid mixing and their application for chemical synthesis. *The Chemical Record*, 1(5):395–405, 2001.

[36] S. K. Kim and A. W. Troesch. Streaming flows generated by high-frequency small-amplitude oscillations of arbitrarily shaped cylinders. *Physics of Fluids A: Fluid Dynamics (1989-1993)*, 1(6):975–985, 1989.

[37] T. Laurell, F. Petersson, and A. Nilsson. Chip integrated strategies for acoustic separation and manipulation of cells and particles. *Chem. Soc. Rev.*, 36(3):492–506, 2007.

[38] T. G. Leighton. *The Acoustic Bubble*. Academic Press, 1997.

[39] J. Lighthill. Acoustic streaming. *J. Sound Vib.*, 61(3):391–418, 1978.

[40] C. Lin, Y. Lai, H. Liu, and A. Wo. Microvortices and recirculating flow generated by an oscillatory microplate for microfluidic applications. *Appl. Phys. Lett.*, 93(13):133503, 2008.

[41] C.-M. Lin, H.-P. Liu, Y.-S. Lai, C.-C. Tseng, C.-Y. Chen, and A. Wo. Micromixing via recirculatory flow generated by an oscillatory microplate. *Microfluid. Nanofluid.*, 11(2):167–176, 2011.

[42] Z. Lin, J.-L. Thiffeault, and C. R. Doering. Optimal stirring strategies for passive scalar mixing. *Journal of Fluid Mechanics*, 675:465–476, 2011.

[43] R. Liu, R. Lenigk, R. Druyor-Sanchez, J. Yang, and P. Grodzinski. Hybridization enhancement using cavitation microstreaming. *Anal. Chem.*, 75(8):1911–1917, 2003.

[44] R. H. Liu, J. Yang, M. Z. Pindera, M. Athavale, and P. Grodzinski. Bubble-induced acoustic micromixing. *Lab Chip*, 2(3):151–157, 2002.

[45] X. Liu and J. Wu. Acoustic microstreaming around an isolated encapsulated microbubble. *J. Acoust. Soc. Amer.*, 125(3):1319–1330, 2009. doi: 10.1121/1.3075552.

[46] M. S. Longuet-Higgins. Mass transport in water waves. *Phil. Trans. Roy. Soc. Lond. Series A: Mathematical and Physical Sciences*, 245(903):535–581, 1953.

[47] M. S. Longuet-Higgins. Viscous streaming from an oscillating spherical bubble. *Proc. Roy. Soc. A*, 454(1970):725–742, 1998.

[48] P. M. Lovalenti and J. F. Brady. The hydrodynamic force on a rigid particle undergoing arbitrary time-dependent motion at small reynolds number. *Journal of Fluid Mechanics*, 256: 561–605, 1993.

[49] B. Lutz, J. Chen, and D. Schwartz. Microfluidics without microfabrication. *Proc. Nat. Acad. Sci. U.S.A.*, 100(8):4395–4398, 2003.

[50] B. R. Lutz, J. Chen, and D. T. Schwartz. Microscopic steady streaming eddies created around short cylinders in a channel: Flow visualization and stokes layer scaling. *Phys. Fluids*, 17(2): 1–7, 2005.

[51] B. R. Lutz, J. Chen, and D. T. Schwartz. Hydrodynamic tweezers: 1. noncontact trapping of single cells using steady streaming microeddies. *Anal. Chem.*, 78(15):5429–5435, 2006.

[52] D. Lyubimov, T. Lyubimova, and S. Shklyaev. Behavior of a drop on an oscillating solid plate. *Phys. Fluids*, 18(1):012101, 2006.

[53] M. MacDonald, G. Spalding, and K. Dholakia. Microfluidic sorting in an optical lattice. *Nature*, 426(6965):421–424, 2003.

[54] A. Marin, M. Rossi, B. Rallabandi, C. Wang, S. Hilgenfeldt, and C. J. Kähler. Three-dimensional phenomena in microbubble acoustic streaming. *Physical Review Applied*, 3(4): 041001, 2015.

[55] P. Marmottant and S. Hilgenfeldt. Controlled vesicle deformation and lysis by single oscillating bubbles. *Nature*, 423(6936):153–156, 2003.

[56] P. Marmottant and S. Hilgenfeldt. A bubble-driven microfludic transport element for bioengineering. *Proc. Natl. Acad. Sci. USA*, 101(26):9523–9527, 2004.

[57] P. Marmottant, J. P. Raven, H. Gardeniers, J. G. Bomer, and S. Hilgenfeldt. Microfluidics with ultrasound-driven bubbles. *J. Fluid Mech.*, 568:109–118, 2006.

[58] J. S. Marshall. *Inviscid incompressible flow*. John Wiley & Sons, 2001.

[59] G. Mathew, I. Mezić, and L. Petzold. A multiscale measure for mixing. *Physica D: Nonlinear Phenomena*, 211(1):23–46, 2005.

[60] G. Mathew, I. Mezić, S. Grivopoulos, U. Vaidya, and L. Petzold. Optimal control of mixing in stokes fluid flows. *J. Fluid Mech.*, 580:261–281, 2007.

[61] M. R. Maxey and J. J. Riley. Equation of motion for a small rigid sphere in a nonuniform flow. *Physics of Fluids (1958-1988)*, 26(4):883–889, 1983.

[62] J. C. McDonald, D. C. Duffy, J. R. Anderson, D. T. Chiu, H. Wu, O. J. A. Schueller, and G. M. Whitesides. Fabrication of microfluidic systems in poly(dimethylsiloxane). *Electrophoresis*, 21(1):27–40, 2000.

[63] P. Meunier and E. Villermaux. How vortices mix. *Journal of Fluid Mechanics*, 476:213–222, 2003.

[64] P. Meunier and E. Villermaux. The diffusive strip method for scalar mixing in two dimensions. *Journal of fluid mechanics*, 662:134–172, 2010.

[65] D. Miller. Particle gathering and microstreaming near ultrasonically activated gas-filled micropores. *J. Acoust. Soc. Am.*, 84(4):1378–1387, 1988.

[66] N. A. Mortensen, F. Okkels, and H. Bruus. Reexamination of hagen-poiseuille flow: Shape dependence of the hydraulic resistance in microchannels. *Physical Review E*, 71(5):057301, 2005.

[67] N. Nama, P.-H. Huang, T. J. Huang, and F. Costanzo. Investigation of acoustic streaming patterns around oscillating sharp edges. *Lab on a Chip*, 14(15):2824–2836, 2014.

[68] N.-T. Nguyen and R. M. White. Acoustic streaming in micromachined flexural plate wave devices: numerical simulation and experimental verification. *IEEE Trans. Ultrason. Ferroelectr. Freq. Control*, 47(6):1463–1471, 2000.

[69] N.-T. Nguyen and Z. Wu. Micromixers—a review. *Journal of Micromechanics and Microengineering*, 15(2):R1, 2005.

[70] W. L. Nyborg. Acoustic streaming near a boundary. *J. Acoust. Soc. Am.*, 30(4):329–339, 1958. doi: 10.1121/1.1909587. URL `http://link.aip.org/link/?JAS/30/329/1`.

[71] M. Oddy, J. Santiago, and J. Mikkelsen. Electrokinetic instability micromixing. *Anal. Chem.*, 73(24):5822–5832, 2001.

[72] J. M. Ottino. *The kinematics of mixing: stretching, chaos, and transport*, volume 3. Cambridge university press, 1989.

[73] M. V. Patel, A. R. Tovar, and A. P. Lee. Lateral cavity acoustic transducer as an on-chip cell/particle microfluidic switch. *Lab Chip*, 12(1):139–145, 2012.

[74] H. V. Phan, M. Şeşen, T. Alan, and A. Neild. Single line particle focusing using a vibrating bubble. *Appl. Phys. Lett.*, 105(19):193507, 2014.

[75] M. Plesset and A. Prosperetti. Bubble dynamics and cavitation. *Annu. Rev. Fluid Mech.*, 9 (1):145–185, 1977.

[76] A. Prosperetti. Viscous effects on perturbed spherical flows. *Q. Appl. Math.*, 35:339–352, 1977.

[77] B. Rallabandi, C. Wang, and S. Hilgenfeldt. Two-dimensional streaming flows driven by sessile semicylindrical microbubbles. *J. Fluid Mech.*, 739:57–71, 2014.

[78] B. Rallabandi, A. G. Marín, M. Rossi, S. Hilgenfeldt, and C. J. Kähler. *Three-dimensional streaming flow in confined geometries*, 2015. submitted.

[79] B. Rallabandi, C. Wang, L. Guo, and S. Hilgenfeldt. *Systematic strategies for open flow mixing with microbubble streaming*, 2015. preprint.

[80] V. B. Rallabandi. The harmonic excitation of a cylindrical bubble pinned to a plane surface: flow field and oscillation dynamics. 2012.

[81] W. P. Raney, J. C. Corelli, and P. J. Westervelt. Acoustical streaming in the vicinity of a cylinder. *J. Acoust. Soc. Amer.*, 26:1006, 1954.

[82] N. Riley. Oscillating viscous flows. *Mathematika*, 12(02):161–175, 1965.

[83] N. Riley. On a sphere oscillating in a viscous fluid. *Q. J. Mech. Appl. Math.*, 19(4):461–472, 1966.

[84] N. Riley. Oscillatory viscous flows. review and extension. *IMA J. Appl. Math.*, 3(4):419–434, 1967.

[85] N. Riley. Acoustic streaming. *Theor. Comput. Fluid Dyn.*, 10(1-4):349–356, 1998.

[86] N. Riley. Steady streaming. *Annu. Rev. Fluid Mech.*, 33:43–65, 2001.

[87] P. Rogers and A. Neild. Selective particle trapping using an oscillating microbubble. *Lab Chip*, 11(21):3710–3715, 2011.

[88] J. A. Rooney. Hemolysis near an ultrasonically pulsating gas bubble. *Science*, 169(3948): 869–871, 1970.

[89] M. Rossi and C. J. Kähler. Optimization of astigmatic particle tracking velocimeters. *Exp. Fluids*, 55(9):1–13, 2014.

[90] S. S. Sadhal. Acoustofluidics 16: Acoustics streaming near liquid–gas interfaces: drops and bubbles streaming near liquid–gas interfaces: drops and bubbles. *Lab Chip*, 12(16):2771–2781, 2012.

[91] P. Saffman. The lift on a small sphere in a slow shear flow. *Journal of fluid mechanics*, 22 (02):385–400, 1965.

[92] D. Saintillan and M. J. Shelley. Emergence of coherent structures and large-scale flows in motile suspensions. *Journal of the Royal Society Interface*, 9(68):571–585, 2012.

[93] A. Sanz. The influence of the outer bath in the dynamics of axisymmetric liquid bridges. *J. Fluid Mech.*, 156:101–140, 1985.

[94] A. Sanz and J. Diez. Non-axisymmetric oscillations of liquid bridges. *J. Fluid Mech.*, 205: 503–521, 1989.

[95] R. B. Schoch, J. Han, and P. Renaud. Transport phenomena in nanofluidics. *Rev. Mod. Phys.*, 80(3):839, 2008.

[96] E. L. Shock and M. D. Schulte. Organic synthesis during fluid mixing in hydrothermal systems. *Journal of Geophysical Research: Planets (1991–2012)*, 103(E12):28513–28527, 1998.

[97] S. Smale. Differentiable dynamical systems. *Bulletin of the American mathematical Society*, 73(6):747–817, 1967.

[98] K. J. Stebe and C. Maldarelli. Remobilizing surfactant retarded fluid particle interfaces: Ii. controlling the surface mobility at interfaces of solutions containing surface active components. *Journal of colloid and interface science*, 163(1):177–189, 1994.

[99] H. A. Stone and S. Kim. Microfluidics: basic issues, applications, and challenges. *AIChE Journal*, 47(6):1250–1254, 2001.

[100] A. D. Stroock, S. K. Dertinger, A. Ajdari, I. Mezić, H. A. Stone, and G. M. Whitesides. Chaotic mixer for microchannels. *Science*, 295(5555):647–651, 2002.

[101] J. T. Stuart. Double boundary layers in oscillatory viscous flow. *J. Fluid Mech.*, 24(4): 673–687, 1966.

[102] R. Sturman, J. M. Ottino, and S. Wiggins. *The mathematical foundations of mixing: the linked twist map as a paradigm in applications: micro to macro, fluids to solids*, volume 22. Cambridge University Press, 2006.

[103] M. Tan, J. Friend, and L. Yeo. Microparticle collection and concentration via a miniature surface acoustic wave device. *Lab Chip*, 7(5):618–625, 2007.

[104] G. Taylor. Dispersion of soluble matter in solvent flowing slowly through a tube. *Proceedings of the Royal Society of London A: Mathematical, Physical and Engineering Sciences*, 219 (1137):186–203, 1953.

[105] R. Thameem, B. Rallabandi, and S. Hilgenfeldt. *Fast sorting of microparticles in bubble streaming flows*, 2015. preprint.

[106] P. Tho, R. Manasseh, and A. Ooi. Cavitation microstreaming patterns in single and multiple bubble systems. *J. Fluid Mech.*, 576:191–233, 2007.

[107] E. Villermaux and J. Duplat. Mixing as an aggregation process. *Physical review letters*, 91 (18):184501, 2003.

[108] B. Vukasinovic, M. Smith, and A. Glezer. Dynamics of a sessile drop in forced vibration. *J. Fluid Mech.*, 587:395–423, 2007.

[109] C. Wang. *Microbubble streaming flows for non-invasive particle manipulation and liquid mixing*. PhD thesis, University of Illinois at Urbana-Champaign, 2013.

[110] C. Wang, S. V. Jalikop, and S. Hilgenfeldt. Size-sensitive sorting of microparticles through control of flow geometry. *Appl. Phys. Lett.*, 99(3):034101, 2011.

[111] C. Wang, S. V. Jalikop, and S. Hilgenfeldt. Efficient manipulation of microparticles in bubble streaming flows. *Biomicrofluidics*, 6(1):012801, 2012.

[112] C. Wang, B. Rallabandi, and S. Hilgenfeldt. Frequency dependence and frequency control of microbubble streaming flows. *Phys. Fluids*, 25:022002, 2013.

[113] C.-Y. Wang. On high-frequency oscillatory viscous flows. *J. Fluid Mech.*, 32(01):55–68, 1968.

[114] S. S. Wang, Z. J. Jiao, X. Y. Huang, C. Yang, and N. T. Nguyen. Acoustically induced bubbles in a microfluidic channel for mixing enhancement. *Microfluid. Nanofluid.*, 6(6):847–852, 2009.

[115] Y. Wang, D. T. Papageorgiou, and C. Maldarelli. Increased mobility of a surfactant-retarded bubble at high bulk concentrations. *Journal of Fluid Mechanics*, 390:251–270, 1999.

[116] E. Watson. Diffusion in oscillatory pipe flow. *Journal of Fluid Mechanics*, 133(1):233–244, 1983.

[117] S. Wiggins. *Introduction to applied nonlinear dynamical systems and chaos*, volume 2. Springer Science & Business Media, 2003.

[118] M. Wiklund, R. Green, and M. Ohlin. Acoustofluidics 14: Applications of acoustic streaming in microfluidic devices. *Lab Chip*, 12(14):2438–2451, 2012.

[119] J. Wu and G. Du. Streaming generated by a bubble in an ultrasound field. *J. Acoust. Soc. Amer.*, 101(4):1899–1907, 1997.

[120] Y. Xie, D. Ahmed, M. I. Lapsley, S.-C. S. Lin, A. A. Nawaz, L. Wang, and T. J. Huang. Single-shot characterization of enzymatic reaction constants K_m and k_{cat} by an acoustic-driven, bubble-based fast micromixer. *Anal. Chem.*, 84(17):7495–7501, 2012.

[121] J. Xu and D. Attinger. Acoustic excitation of superharmonic capillary waves on a meniscus in a planar microgeometry. *Phys. Fluids*, 19(10):108107, 2007.

[122] L. Yeo and J. Friend. Ultrafast microfluidics using surface acoustic waves. *Biomicrofluidics*, 3(1):012002, 2009.

[123] D. L. Youngs. Three-dimensional numerical simulation of turbulent mixing by rayleigh–taylor instability. *Physics of Fluids A: Fluid Dynamics (1989-1993)*, 3(5):1312–1320, 1991.

[124] B. Ziaie, A. Baldi, M. Lei, Y. Gu, and R. A. Siegel. Hard and soft micromachining for biomems: review of techniques and examples of applications in microfluidics and drug delivery. *Advanced Drug Delivery Reviews*, 56(2):145–172, 2004.